Rijkswaterstaat
Ministerie van Infrastructuur en Waterstaat

Rijkswaterstaat Technisch Document (RTD)

Validation of the Guidelines for Nonlinear Finite Element Analysis of Concrete Structures

Part: Pre-stressed beams 2

Doc.nr.: RTD 1016-3D:2020
Versie: 1.0
Status: Final
Datum: 2 April 2020

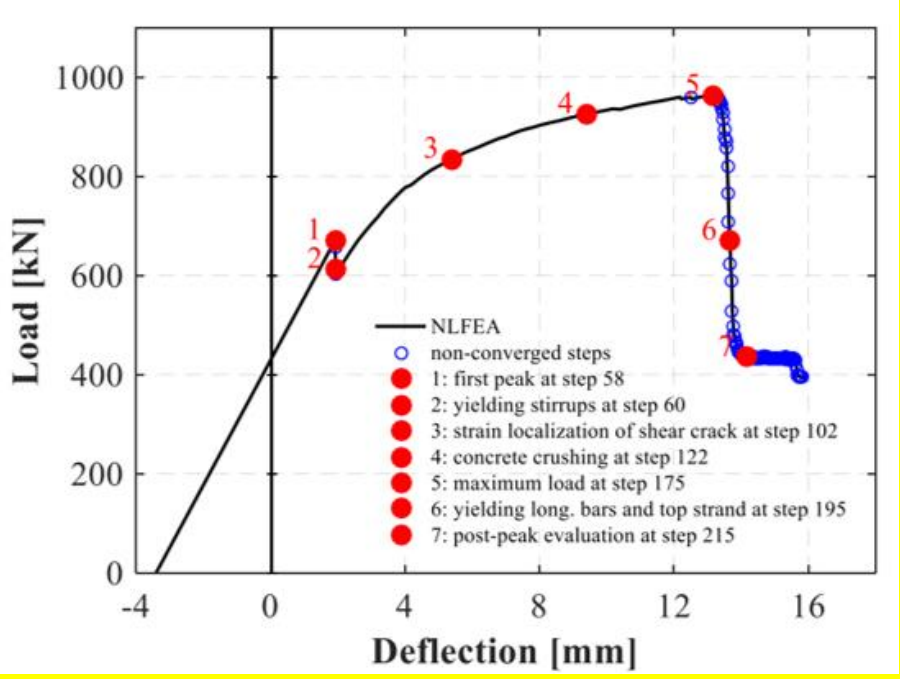

Water. Wegen. Werken. Rijkswaterstaat

Preface

This document investigates the validity of the Guidelines for Nonlinear Finite Element Analysis for three more reinforced beams. The focus is on beams in which the tensile strength of the concrete is expected to be dominant.

This document is fully based on a study performed by TNO. The TNO report 2017-R11413-B (30 April 2018, 107 pages) is included in its entirety.

The analyses were performed by TNO as 'blind predictions', meaning that the analyst did not have prior knowledge of the experimental results. Afterwards, the results were compared with experimental observations. This document includes the original blind predictions, supplemented with analytical analysis results, the experimental outcomes and a discussion for each of the beams.

This document is one from a series of documents. At the time of writing, the following documents have been issued:

RTD 1016-1:	Guidelines for Nonlinear Finite Element Analysis of Concrete Structures
RTD 1016-2:	Validation of the Guidelines for Nonlinear Finite Element Analysis of Concrete Structures - Part: Overview of results
RTD 1016-3A:	Validation of the Guidelines for Nonlinear Finite Element Analysis of Concrete Structures - Part: Reinforced beams
RTD 1016-3B:	Validation of the Guidelines for Nonlinear Finite Element Analysis of Concrete Structures - Part: Prestressed beams
RTD 1016-3C:	Validation of the Guidelines for Nonlinear Finite Element Analysis of Concrete Structures - Part: Slabs
RTD 1016-3D:	Validation of the Guidelines for Nonlinear Finite Element Analysis of Concrete Structures - Part: Prestressed beams, 2

Urbanisation
Stieltjesweg 1
2628 CK Delft
P.O. Box 155
2600 AD Delft
The Netherlands

www.tno.nl

T +31 88 866 20 00
F +31 88 866 06 30

TNO report

TNO 2017 R11413-B

Validating the guidelines for nonlinear finite element analysis of three prestressed concrete beams - blind predictions

Date 30 April 2018

Author(s) Dr.ir. A.T. Slobbe
Dr.ir. A.J. Bigaj - van Vliet

Copy no 0100310156B
No. of copies
Number of pages 107 (incl. appendices)
Number of appendices

Customer Rijkswaterstaat
T.a.v. H. Sliedrecht
Postbus 2322
3500 GE Utrecht

Project name Cases dwarskracht ten behoeve van het project Constructieve Veiligheid op Orde
Project number 060.28859

Summary

This work investigates how well the failure process and the maximum load capacity of three pre-selected experiments with prestressed concrete girders can be predicted by nonlinear finite element analysis. The analyses are performed according to the RTD1016 guidelines for nonlinear finite element analysis of concrete structures (Rijkswaterstaat, 2017a). Furthermore, the analyses are performed as ‘blind predictions’, meaning that the analyst do not have prior knowledge of the experimental results. The results of this work may be used by Rijkswaterstaat to amend or complement the validation of the RTD guidelines, if needed.

Contents

Summary **2**

1 Introduction **4**
1.1 Background 4
1.2 Problem statement 4
1.3 Approach 5
1.4 Outline of the report 5

2 Case PB5: Choulli, Mari, Cladera, girder without stirrups (2005) **6**
2.1 Experimental setup and results 6
2.2 Analytical analysis 10
2.3 Finite element model 14
2.4 Nonlinear finite element analysis 20
2.5 Application of safety formats for nonlinear finite element analysis 25
2.6 Sensitivity analysis 28
2.7 Concluding remarks 31

3 Case PB6: Choulli, Mari, Cladera, girder with stirrups (2005) **33**
3.1 Experimental setup and results 33
3.2 Analytical analysis 38
3.3 Finite element model 44
3.4 Nonlinear finite element analysis 49
3.5 Application of safety formats for nonlinear finite element analysis 55
3.6 Sensitivity analysis 59
3.7 Concluding remarks 61

4 Case PB7: Leonhardt, Koch, Rostasy, beam IP3 (1973) **63**
4.1 Experimental setup and results 63
4.2 Analytical analysis 68
4.3 Finite element model 74
4.4 Nonlinear finite element analysis 79
4.5 Application of safety formats for nonlinear finite element analysis 85
4.6 Sensitivity analysis 88
4.7 Concluding remarks 92

5 Recommendations for RTD guidelines **93**

6 References **96**

7 Signature **97**

Appendices
A Case PB5: additional results
B Case PB7: additional results

1 Introduction

This chapter describes the background of the project, the problem statement, the adopted approach and the outline of the report.

1.1 Background

In coming future, the ministry of Public work and Transport (Rijkswaterstaat) intends to commission the assessment of the shear capacity of a number of concrete bridges, using nonlinear finite element analysis and the RTD1016 guideline (Rijkswaterstaat, 2017a). The bridges under consideration are constructed with T-shaped prestressed concrete girders. In order to validate the applicability of RTD1016 for the assessment of these bridges, Rijkswaterstaat has asked TNO to perform nonlinear finite element analyses of several experiments with prestressed concrete girders that are reported in the literature using the procedures as described in the RTD1016. The results of these analyses and the experience gained with application of the RTD1016 may be used by Rijkswaterstaat to amend or complement the validation of the RTD guideline, if needed.

1.2 Problem statement

TNO is asked to investigate how well the failure process and the maximum load capacity of three pre-selected prestressed concrete girders can be predicted by nonlinear finite element analysis. The following conditions are set:

- the analyses are performed as ‘blind predictions’, meaning that the analyst do not have prior knowledge of the experimental results;
- the analyses are performed strictly according to the RTD document (Rijkswaterstaat, 2017a);
- the analyses are reported according to the format set in RTD document (Rijkswaterstaat, 2017b).

For each of the three cases, the following set of analyses is performed:

1. The reference analysis, in which the experiment is modelled in plane stress conditions, the concrete behaviour is represented by a total strain based smeared rotating crack model and the input for the model parameters is based on mean values of the material properties.
2. Analyses to demonstrate the application of the three semi-probabilistic safety formats for nonlinear finite element analysis as formulated in *fib* Model Code 2010 (CEB/fib, 2012), which are: (1) the global resistance factor method (GRF); (2) the method of estimation of a coefficient of variation of resistance (ECOV); and (3) the partial factor method (PF).
3. Analyses that investigate the sensitivity of the results of the reference analysis with respect to the crack model, the level of prestressing force, the geometrical representation / element type, and the tensile strength of the concrete.

1.3 Approach

The work starts with preparing a plan of approach to perform the numerical analyses of the three prestressed concrete girders on the basis of the information provided by Rijkswaterstaat. This plan of approach describes per case all the steps in the modelling process and explains the assumptions and modelling choices that are made. After approval of the plan of approach by Rijkswaterstaat and TU Delft, the cases are sequentially worked out with the following sub steps:

- Generating the finite element model;
- Testing the finite element model;
- Performing the reference analysis and interpret the results;
- Performing analyses for the semi-probabilistic formats and the sensitivity study;
- Reporting the modelling steps and the results according to the RTD document (Rijkswaterstaat, 2017b).
- The description of the experimental results, the analytical analyses and discussions have been added to the report at the very end of the project.

All the analyses are performed with DIANA 10.1, diadate July 17th, 2017. The analyses are carried out according to the guidelines of Rijkswaterstaat for nonlinear finite element analysis of concrete structures (Rijkswaterstaat, 2017a).
Rijkswaterstaat and TU Delft are consulted in case the guidelines are ambiguous or TNO prefers a different choice in the modelling of the beams than what is indicated by the guidelines. When reporting the outcomes of the analysis, all issues that have been identified as ambiguous or gave rise to proposing different choices in the modelling approach are listed as points of attention, which are recommended for consideration in case of amending the guidelines.
The progress and results of the work are reviewed by the following persons:

- Ir. M. Roosen, Rijkswaterstaat;
- Ir. H. Sliedrecht, Rijkswaterstaat;
- Dr. ir. M.A.N. Hendriks, TU Delft;
- Dr. Ir. C. van der Veen, TU Delft.

1.4 Outline of the report

Each of the cases is reported in a separate chapter of this document. Hence, the remaining of this report is structured as follows. Chapters 2, 3 and 4 discuss the results of the analysis of the cases PB5, PB6 and PB7 respectively. These chapters include the following subsections:

- Experimental setup;
- Experimental results (written by M. Roosen & M.A.N. Hendriks, later added);
- Analytical analysis (written by M. Roosen & M.A.N. Hendriks, later added);
- Finite element model;
- Nonlinear finite element analysis;
- Application of the safety formats for nonlinear finite element analysis;
- Sensitivity analysis;
- Concluding remarks.

Chapter 5 contains the list and discussion of all issues that are recommended for consideration in case of amending the guidelines.

2 Case PB5: Choulli, Mari, Cladera, girder without stirrups (2005)

This chapter describes the experimental setup and results, analytical analysis, finite element modelling, numerical analyses and the application of safety formats for nonlinear finite element analysis for the prestressed concrete beam that is denoted with *case PB5*. Case PB5 is a pre-tensioned I-shaped beam without stirrups. It concerns specimen HAP1W in the experiment of Choulli (2005).

2.1 Experimental setup and results

This section provides the details of the experimental setup in terms of geometry of the beam, material properties and boundary conditions. Furthermore, the result of the test is described.

2.1.1 Geometry

Figure 1 shows the geometry, the reinforcement layout and the location of the prestressing strands of the beam. The beam has an I-shaped cross-section, a length of 10.0 m and a total depth of 0.75 m. The reinforcement consists of six Ø8 mm reinforcing bars in the top flange. Additionally, two Ø10 mm rebars of 3.0 m length are placed in the top flange at both ends of the beam. Case PB5 contains no transversal reinforcement along the web, except in the anchorage zone of the prestressing strands. Stirrups of Ø10 mm and Ø12 mm are used in the web (from bottom flange to top flange) and bottom flange over an approximately 0.45 m distance from each end. This set of stirrups is also placed at 3.0 m of the east end.

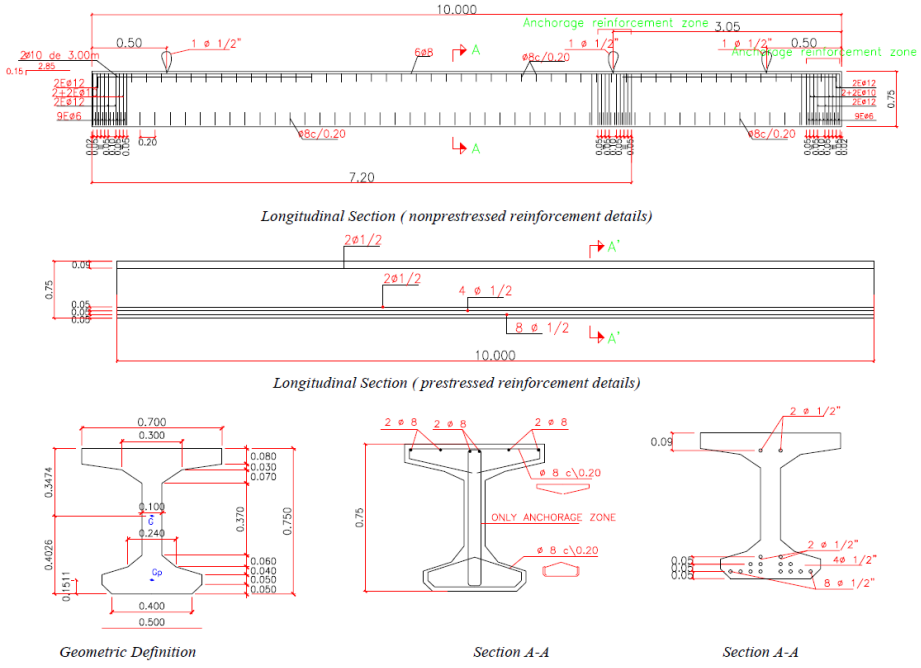

Figure 1: Case PB5. Geometry, reinforcement layout and the location of the prestressing strands (dimensions in m). The pictures are taken from (Choulli, 2005).

The prestressing force is transferred by sixteen straight bonded strands 0.5” in a long line process, with an area A_p of 99 mm^2 per strand. The total area of prestressing strands in the beam equals 1584 mm^2. The initial stress in the prestressing steel without losses σ_{p0} equals 1397 N/mm^2. The averaged initial stress in the concrete σ_{cp} without prestressing losses equals 11.37 N/mm^2. The averaged initial stress in the concrete σ_{cp} at the day of testing (incl. losses due to elastic shortening of the concrete, creep, shrinkage and relaxation) equals 9.56 N/mm^2. The prestressing force was applied six days after casting. Testing was performed 38 days after casting.

2.1.2 Material properties

Table 1 summarizes the provided concrete, reinforcement and strand properties. The mean concrete cylinder compressive strength f_{cm} of 99.15 N/mm^2 is obtained from the results of standard 150 mm x 300 mm cylinder tests (at the day of testing). The mean concrete cylinder compressive strength at six days after casting equals 71.4 N/mm^2.

Table 1: Case PB5. Properties of concrete, reinforcement and prestressing strands.

Concrete properties	
f_{cm} (N/mm^2)	**d_{max} (mm)**
99.15	12

Reinforcement and strand properties							
	Steel	**Corru-gation**	**Ø (mm)**	**E_s (N/mm^2)**	**f_{ym} (N/mm^2)**	**f_{tm} (N/mm^2)**	**ε_u (%)**
Stirrups	B500S	0.57	8.0	NA	525.38	660.63	26.9*
Long. bars Ø8	B500SD	0.58	8.0	NA	556.50	664.00	25.0*
Long. bars Ø10	B500SD	0.79	10.0	NA	581.00	691.00	24.0*
Strands	Y1860 S7 13.0	-	12.7	192940	1776	1941.4	5.17

* The ultimate strain is determined from test specimens with length of 100 mm.

2.1.3 Boundary conditions and loading

Figure 2 shows the test setup of case PB5. The simply supported beam was subjected to a three-point bending test. The beam had a fixed support near the applied load (west side) and a sliding support on the other side (east side). The test consisted of two stages. In the first stage, the east side of the beam was tested. In the second stage, the west side of the beam was tested. The current analysis concerns the second stage of testing. During this stage of testing, a displacement controlled load was placed at 2.1 m distance from the left support. The load was applied by a hydraulic jack, using a closed loop hydraulic MTS 1100 KN equipment. The loading rate varied from 0.3 mm/min to 1 mm/min. The dimension of the load plate was 75 mm. The beam was monotonically loaded until failure. Figure 3 shows the test setup during testing of the west side of the beam.

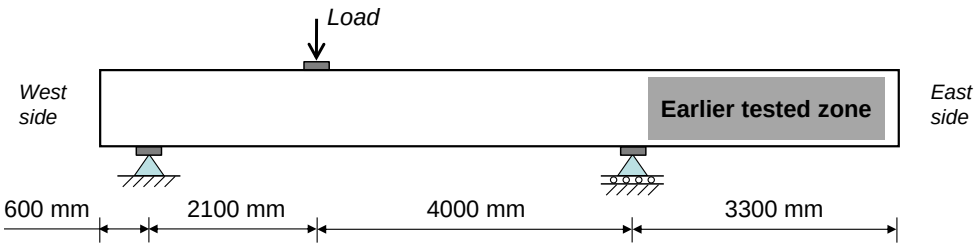

Figure 2: Case PB5. Loading and boundary conditions (dimensions in mm).

Figure 3: Case PB5. Overview of the test setup during testing the west side of the beam. The picture is taken from (Choulli, 2005).

2.1.4 *Experimental results*

Figure 4 shows the obtained load-deflection response. The first major shear crack appeared at a load of 633 kN, with an angle of 22 degrees to the horizontal. The principal and the first crack started in the mid-height of the web and propagated immediately throughout the depth of the web, see Figure 5. While reloading, the first crack continued opening, but the specimen continued to resist more load. Spalling of the concrete occurred prior to the failure, at the bottom of the diagonal shear cracks. Each drop in the load followed the development of a diagonal crack (not visible at this scale in Figure 4). In total five principal diagonal shear cracks were formed, see Figure 6 and Figure 7. No flexural cracks were formed. The formation of the cracks reduced the stiffness of the girder. None of the prestress tendons did reach their yield strength at any time during the test. Before recording the test data, a load of about 30 kN was applied to stabilize the test system. This load is added to the reported values of the external load. The maximum observed load level is 778 kN at a deflection of 17.7 mm.

Quoting Choulli (2005), the following failure process took place in all tested girders without stirrups. “In all the beam specimens the first and principal diagonal shear crack corresponded to diagonal tension failure. After the formation of new diagonal cracks, the arch action was developed and the final collapse that resulted in the four beams tested ... collapsed by a diagonal and sudden shear compression failure, with the development of more than one diagonal shear crack”. Specific for girder

PB5 the subsequent description of the failure process was added: “The final collapse of the beam specimen end resulted from a diagonal tension failure in the web.”

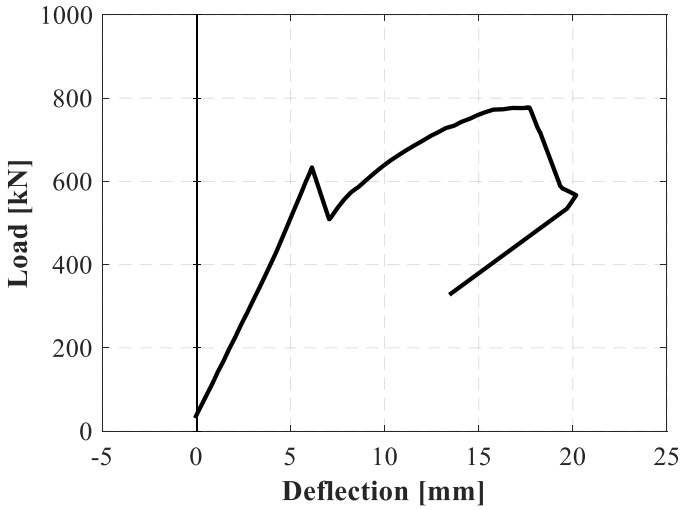

Figure 4: Case PB5. The experimentally obtained load – deflection curve.

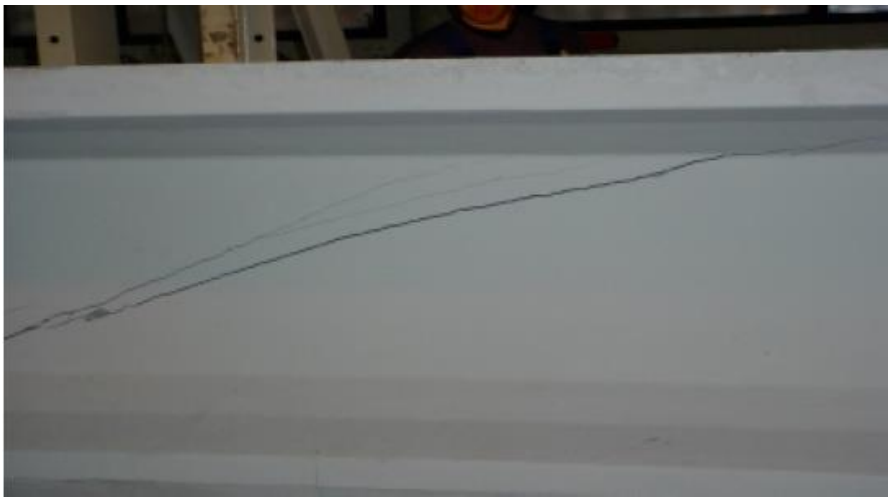

Figure 5: Case PB5. Development of the first shear crack in the girder. The picture is taken from (Choulli, 2005).

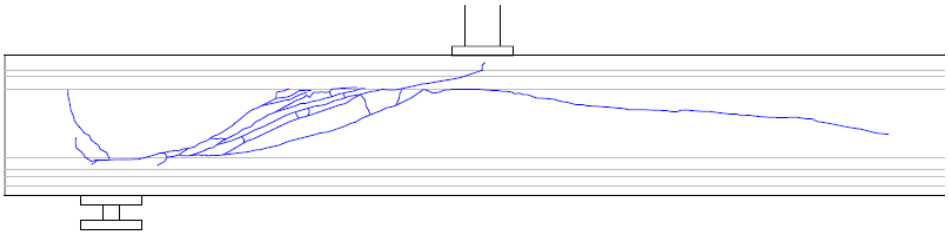

Figure 6: Case PB5. Crack pattern at failure. The picture is taken from (Choulli, 2005).

Figure 7: Case PB5. Details of the girder at failure. The picture is taken from (Choulli, 2005).

2.2 Analytical analysis

2.2.1 *Cross-sectional properties*

Figure 8 shows the cross-section of the girder. The corresponding cross-sectional properties are:

- the area of the cross-section A: 194500 mm^2,
- the second moment of area I: = 1.50·10^{10} mm^4,
- the first moment of area (axis top flange-web) S_{tf}: 2.39·10^7 mm^3,
- the first moment of area (centroidal axis) S_c: 2.53·10^7 mm^3,
- the first moment of area (axis bottom-flange web) S_{bf}: 2.33·10^7 mm^3.

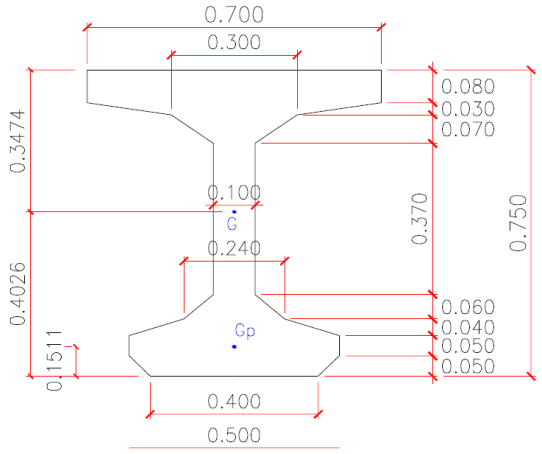

Figure 8: Case PB5. Cross-section. The picture is taken from (Choulli, 2005).

2.2.2 *Cross-sectional forces due to the loads*

In the following, the moments and shear forces due to dead weight, the prestressing force and the point load at midspan are calculated.

Dead weight

Figure 9 shows the static scheme of the girder subjected to the dead weight. Assuming a density for the reinforced concrete ρ_c of 2500 kg/m^3, the moments and shear forces between the supports due to this load are calculated as follows:

$q_{dw} = A \cdot \rho_c = 0.1945 \cdot 25 = 4.86$ kN/m
$R_{1,dw} = (10/2 - 3.3)/ 6.1 \cdot 10 \cdot q_{dw} = 13.5$ kN (vertical reaction force of left support)
$V_{E,dw} = -0.6 \cdot q_{dw} + R_{1,dw} - 4.86 \cdot x = 10.6 - 4.86 \cdot x \quad [0 < x < 6.1]$
$M_{E,dw} = 13.5 \cdot x - ½ \cdot 4.86 \cdot (x + 0.6)^2 \quad [0 < x < 6.1]$

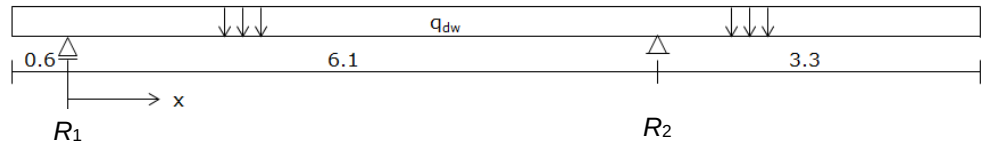

Figure 9: Case PB5. Dead weight load.

Prestressing force

The moments and shear forces due to the prestressing force are calculated as follows:

σ_{cp} = 9.56 N/mm^2 (after losses)
$N_{E;all} = A_c \cdot \sigma_{cp} = 1859$ kN
$N_{E,td} = 1859 / 16 = 116$ KN
$d_{p,top} = 90$ mm (see Figure 1)
$d_{p,bottom} = (2 \cdot 600 + 4 \cdot 650 + 8 \cdot 700) / 14 = 671$ mm (from top side)
$V_p = 0$
$M_p = 14 \cdot 116 \cdot (0.347 - 0.671) + \ldots$
$2 \cdot 116 \cdot (0.347 - 0.090) = -467$ kNm

Note that the prestressing force is fully introduced in the cross-section above the left support, since the transmission length of the tendons equals 556 mm (see 2.3.5).

External point load

Figure 10 shows the static scheme of the girder subjected to the point load. The corresponding moments and shear forces are:

$V_{E,F} = 4.0 / 6.1 \cdot F \quad [0 < x < 2.1]$
$M_{E,F} = 4.0 / 6.1 \cdot F \cdot x \quad [0 \leq x \leq 2.1]$

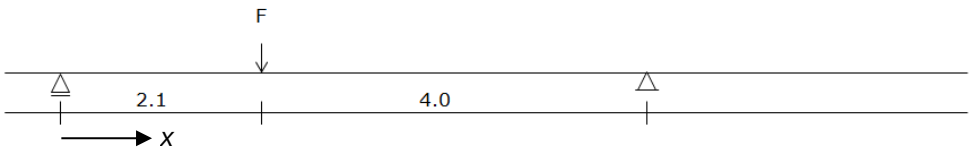

Figure 10: Case PB5. External point load.

2.2.3 *Bending moment resistance*

The analytical approaches predict shear tension failure prior to flexural cracking (which is shown in the next subsection). Hence, the bending moment resistance will not be governing.

2.2.4 *Shear force resistance*

The Model Code 2010 (CEB/fib, 2012) offers two levels of approximations for the calculation of the shear resistance of hollow core slabs and similar structural members without shear reinforcement. According to Model Code 2010, shear failure for these members occurs when the principal tension stress demand in the web exceeds the tensile strength of the concrete.

In the following, the shear resistance of the girder is determined by using both level of approximations. The level II approximation is equal to the Eurocode approach (CEN, 2011).

Shear resistance Eurocode/ Model Code level II, based on mean values

For regions uncracked in bending of prestressed single span members without shear reinforcement, the shear resistance should be limited to the tensile strength of the concrete, according to the Eurocode. The Eurocode prescribes that the calculation of the shear resistance is not required for cross-sections that are closer to the support than the point which is the intersection of the elastic centroidal axis and a line inclined from the inner edge of the support at an angle of 45˚. For this specimen with a support plate length of 75 mm, this distance is equal to 75/2 + 402 = 440mm (see Figure 11).

The maximum allowable point load *F* in Figure 10 is calculated in an iterative way by checking $\sigma_1 \leq f_{ctm}$ for different locations along the length and the height of the beam in the area indicated by the grey zone in Figure 11. For each of these locations, the maximum principal stress σ_1 is calculated with:

$$\sigma_1 = \sqrt{\tau^2 + \left(\frac{\sigma_{cp}}{2}\right)^2} + \frac{\sigma_{cp}}{2}$$

in which

$$\tau = \frac{V_{Rc,calc}\, S}{b_w\, I}$$

Figure 11: Case PB5. Considered locations (grey zone) for maximum principle tensile stresses.

and

$$\sigma_{cp} = \frac{N_E}{A} + \frac{M_E z}{I}$$

The tensile strength of the concrete f_{ctm} is equal to 2.12 ln (1 + 99.15/ 10) = 5.07 N/mm^2.

The critical stress state, $\sigma_1 = f_{ctm}$, was found at x = 2.1 m (under the point load) and at the height of the bottom flange – web connection, for a point load of F_m = 651 kN. Table 2 shows the principal stress state in the grey zone in Figure 11 at this critical load.

To illustrate the calculation procedure, we consider the critical location at x = 2.1 m and z = 203 mm (bottom flange – web connection) for the point load F_m = 651 kN. The cross-sectional forces due to dead weight at his location are V_{dw} = 0.4 kN and M_{dw} = 10.6 kNm, the cross-sectional forces due to the prestressing force are V_p = 0 kN and M_p = -467 kNm, and the cross-sectional forces due to the point load are V_F = 427 kN and M_F = 896 kNm. The maximum principal stress σ_1 is then:

$$\sigma_{cp} = \frac{N_E}{A} + \frac{M_E z}{I} = -\frac{1859 \cdot 10^3}{194500} + \frac{(10.6 + 896 - 467) \cdot 10^6 \cdot 203}{1.50 \cdot 10^{10}} = -3.61 \text{ N/mm}^2$$

$$\tau = \frac{V_{Rc,calc}\, S}{b_w\, I} = \frac{(0.4 + 427) \cdot 10^3 \cdot 2.33 \cdot 10^7}{100 \cdot 1.50 \cdot 10^{10}} = 6.63 \text{ N/mm}^2$$

$$\sigma_1 = \sqrt{\tau^2 + \left(\frac{\sigma_{cp}}{2}\right)^2} + \frac{\sigma_{cp}}{2} = \sqrt{6.63^2 + \left(\frac{-3.61}{2}\right)^2} + \frac{-3.61}{2} = 5.07 \text{ N/mm}^2.$$

The maximum tensile stress at the bottom of the girder at x = 2.1 m for the point load F_m = 651 kN is

$$\sigma_{cp} = \frac{N_E}{A} + \frac{M_E z}{I} = -\frac{1859 \cdot 10^3}{194500} + \frac{(10.6 + 896 - 467) \cdot 10^6 \cdot 403}{1.50 \cdot 10^{10}} = 2.25 \text{N/mm}^2$$

Since this stress value is lower than the (flexural) tensile strength of concrete, no flexural cracking prior to shear tension failure is expected.

Table 2: Case PB5. Principle tensile stresses over the height of the beam at different x values for Fm = 651 kN.

		Horizontal position *x* [m]							
		0.44	**0.60**	**0.85**	**1.10**	**1.35**	**1.60**	**1.85**	**2.10**
Vertical position	*top flange-web*	4.43	4.20	3.88	3.59	3.33	3.10	2.89	2.71
	centroidal	3.99	3.98	3.96	3.95	3.93	3.91	3.90	3.88
	bottom flange-web	2.84	2.97	3.21	3.49	3.81	4.17	4.59	5.07

Shear resistance Eurocode/ Model Code level II, based on design values
When the principal tensile stress is limited to the design value of the tensile strength f_{ctd} = 0.7 f_{ctm} / 1.5 = 2.36 N/mm², the critical stress state is found at F_d = 403 kN. This critical stress state occurs at x = 0.44 m (the cross-section at the left side of the grey zone) and at the height of the top flange – web connection.

To check this critical stress state, we again calculate σ_1. So, x = 0.44 m and z = -167 mm (top flange – web connection) and the point load F_d = 403 kN. The cross-sectional forces due to dead weight at his location are V_{dw} = 8.5 kN and M_{dw} = 3.3 kNm, the cross-sectional forces due to the prestressing force are V_p = 0 kN and M_p = -467 kNm, and the cross-sectional forces due to this point load are V_F = 264 kN and M_F = 116 kNm. The maximum principal stress σ_1 is then:

$$\sigma_{cp} = \frac{N_E}{A} + \frac{M_E z}{I} = -\frac{1859 \cdot 10^3}{194500} + \frac{(3.3 + 116 - 467) \cdot 10^6 \cdot -167}{1.50 \cdot 10^{10}} = -5.69 \text{ N/mm}^2$$

$$\tau = \frac{V_{Rc,calc}\, S}{b_w\, I} = \frac{(8.5 + 264) \cdot 10^3 \cdot 2.39 \cdot 10^7}{100 \cdot 1.50 \cdot 10^{10}} = 4.34 \text{ N/mm}^2$$

$$\sigma_1 = \sqrt{\tau^2 + \left(\frac{\sigma_{cp}}{2}\right)^2} + \frac{\sigma_{cp}}{2} = \sqrt{4.34^2 + \left(\frac{-5.69}{2}\right)^2} + \frac{-5.69}{2} = 2.34 \text{ N/mm}^2.$$

Shear resistance Model Code level I, based on mean values
The simpler level I approximation only considers the concrete compressive stress at the centroidal axis due to prestressing. Presumably to account for the simplification, the resistance must be reduced to 80% of the calculated value. Using the mean value of the concrete tensile strength f_{ctm}, the shear resistance is:

$$V_{Rm,ct} = 0.8\, \frac{I_c\, b_w}{S_c} \sqrt{{f_{ctm}}^2 + \sigma_{cp}\, f_{ctm}}$$

$$V_{Rm,ct} = 0.8\, \frac{1.5 \cdot 10^{10} \cdot 100}{2.53 \cdot 10^7} \sqrt{5.07^2 + 9.56 \cdot 5.07} = 408 \cdot 10^3\ N$$

With $V_{E,dw}$ = 8 kN at x = 0.44 m, the maximum allowable point load F_m in Figure 10 becomes equal to (408 - 8) · 6.1 / 4.0 = 610 kN.

Shear resistance Model Code level I, based on design values
When the principal tensile stress is limited to the design value of the tensile strength f_{ctd} = 0.7 · f_{ctm} / 1.5 = 2.36 N/mm², the design shear resistance $V_{Rd,ct}$ is 252 kN and F_d is 372 kN.

2.3 Finite element model

This section presents all the details of the finite element model for case PB5.

2.3.1 Units

The force unit is in newtons (N) and the length unit in millimeters (mm).

2.3.2 *Geometry*

Case PB5 is modelled in plane stress conditions. Five different parts in the finite element model can be distinguished: (*i*) the I-shaped beam; (*ii*) the support and loading plates; (*iii*) the interface between the beam and the support and loading plates; (*iv*) the reinforcement; and (*v*) the pre-tensioned strands. The modelling choices for each part are discussed in the following. Note that the damage in the zone at the east side of the beam, tested in the first stage of the experiment, is not considered in the model. Since this damage is located at the right-hand side of the right support, it is assumed that neglecting the damage has a minor effect on the structural response.

I-shaped beam: The dimensions of the I-shaped beam are based on Figure 1. To account for the varying out-of-plane thicknesses, the beam geometry is discretized over the height by eight layers, see Figure 12. The calculated thicknesses of the layers are such that the total cross-sectional area of the modelled beam matches with the real cross-sectional area.

Support and loading plates: All plates are modelled with a length of 75 mm and a height of one element (i.e. 50 mm). The out-of-plane thickness of the support plates are set to the thickness of the bottom layer t_1 and the out-of-plane thickness of the loading plate is set to the thickness of the top layer t_8.

Interface: The interfaces between the beam and the support and loading plates are modelled as zero thickness interfaces.

Reinforcement: The reinforcement layout is based on Figure 1. Since some detailed information regarding the positions of the reinforcing bars and stirrups in the beam is missing, the following estimates are made:

- the concrete cover is set to 20 mm (based on $1.5Ø_{strand}$);
- the stirrups in the anchorage zones are distributed over a length of 45 cm;

The stirrups in the top and bottom flanges along the beam (except in the anchorage zones) are neglected in the model[1].

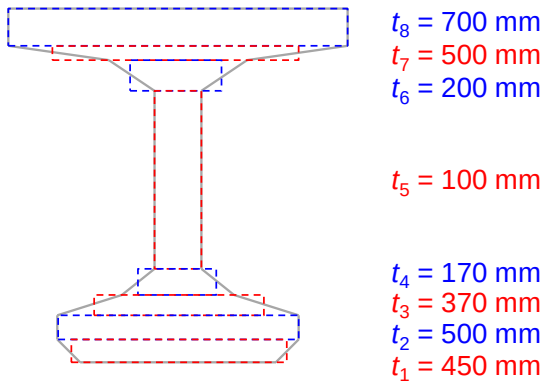

Figure 12: Case PB5. Cross-sectional discretization.

[1] Since the stirrups in the bottom flange consist of two parts (see Figure 1) and their height is limited, it is questionable if they are effective from a mechanical point of view. When included in the model, the stirrups most likely do have an (small) effect on the crack development and subsequently they may affect the failure behaviour.

Pre-tensioned strands: The sixteen strands are located in four different layers, see Figure 1. To avoid stress concentrations, spurious cracking and subsequent numerical instabilities, each layer of strands is modelled separately.

2.3.3 Material models and parameters

The finite element model has six different materials: (*i*) concrete; (*ii*) structural steel; (*iii*) interface; (*iv*) reinforcing bars; (*v*) stirrups and (*vi*) strands. Table 3 summarizes all the adopted material models and properties, based on Table 1 and the RTD guidelines (Rijkswaterstaat, 2017a).

The concrete material behaviour is modelled with a total strain based orthogonal rotating smeared crack model and a band width estimator according to (Govindjee, 1995). The adopted material properties are as follows: Young's modulus E_c of 46.2 GPa, Poisson's ratio ν of 0.15, density of 2500 kg/m^3, tensile strength f_{ctm} of 5.07 MPa, tensile fracture energy G_f of 0.167 N/mm and compressive strength f_{cm} of

Table 3: Case PB5. Summary of the adopted material models and properties in the FE model.

Material/-model	*Variable/parameter*	*Value*
Concrete	Density	2500 kg/m^3
total strain based	Young's modulus*	46.2 GPa
smeared rotating crack	Initial Poisson's ratio ν	0.15
model	Variable Poisson's ratio	Yes
	Compression curve	Parabolic
	Compressive strength	99.15 MPa
	Compressive fracture energy	41.74 N/mm
	Reduction due to lateral cracking	Yes
	Minimum reduction factor f_{cm}	0.4
	Influence of lateral confinement	Yes
	Tensile strength*	5.07 MPa
	Type of tension softening	Hordijk
	Tensile fracture energy*	0.167 N/mm
	Band width estimator	Govindjee
	Maximum aggregate size	12 mm
Stirrups	Young's modulus	200 GPa
hardening plasticity	Yield strength at ε_y = 0.25%	525.38 MPa
	Ultimate strength at ε_u = 27%	660.63 MPa
Longitudinal bars Ø8	Young's modulus	200 GPa
hardening plasticity	Yield strength at ε_y = 0.27%	556.5 MPa
	Ultimate strength at ε_u = 25%	664.0 MPa
Longitudinal bars Ø10	Young's modulus	200 GPa
hardening plasticity	Yield strength at ε_y = 0.28%	581.0 MPa
	Ultimate strength at ε_u = 24%	691 MPa
Strands	Young's modulus	192.94 GPa
hardening plasticity	Yield strength at ε_y = 0.92%	1776 MPa
	Ultimate strength at ε_u = 5.17%	1941.4 MPa
Bond	Perfect bond	
Interface steel plates	Normal stiffness	$4.62 \cdot 10^4$ N/mm^3
Nonlinear-elasticity	Shear stiffness	$4.62 \cdot 10^1$ N/mm^3
	No-tension interface (Δ - σ_n curve)	Yes
Structural steel	Density	7850 kg/m^3
linear-elastic	Elastic modulus	210 GPa
	Poisson's ratio	0.3

* Derived from relation given in *fib* Model Code 2010 (CEB/fib, 2012).

99.15 MPa. The parameters E_c, f_{ctm} and G_f are derived from the formulas of the *fib* Model Code 2010 (CEB/fib, 2012), based on the given f_{cm} from Table 1. The compressive fracture energy G_c is assumed to be equal to 250 G_f, following reference (Nakamura, 2001). The adopted stress-strain tension softening curve is according to (Hordijk, 1991) and for concrete under compression a parabolic softening behaviour is assumed, see Figure 13. Furthermore, lateral effects of cracking (Vecchio, 1993) and confinement (Selby, 1993) on the compressive strength and a variable Poisson's ratio dependent on the crack width are included.

The material behaviour of the steel plates is modelled with a linear-elastic stress-strain relation, using the elastic properties E_s of 210 GPa and ν of 0.3. Furthermore, the density of the steel is set to 7850 kg/m^3.

The interface between the steel plates and concrete have elastic stiffness properties of $k_n = 4.62 \cdot 10^4$ N/mm^3 and $k_t = 4.62 \cdot 10^1$ N/mm^3, which are derived from the Young's modulus of the concrete. A bilinear behaviour is assumed in the interface normal direction and a linear-elastic behaviour in the interface tangential direction. The normal stiffness in tension and compression are set to $4.62 \cdot 10^1$ N/mm^3 and $4.62 \cdot 10^4$ N/mm^3 respectively, simulating a no-tension interface (see Figure 14).

The reinforcing bars, stirrups and strands adopt von Mises plasticity and hardening behaviour. Figure 15 shows the stress – equivalent plastic strain curve for the strands. Similar curves are applied to the reinforcing bars and stirrups, though with different values. The elastic modulus E_s, the yield strength f_{ym}, the ultimate strength f_{tm} and the ultimate (total) strain[2] ε_u for the different reinforcements are obtained from Table 1. The elastic modulus of the reinforcing bars and stirrups is set to 200 GPa. The interaction between the reinforcements and concrete is modelled with perfect bond.

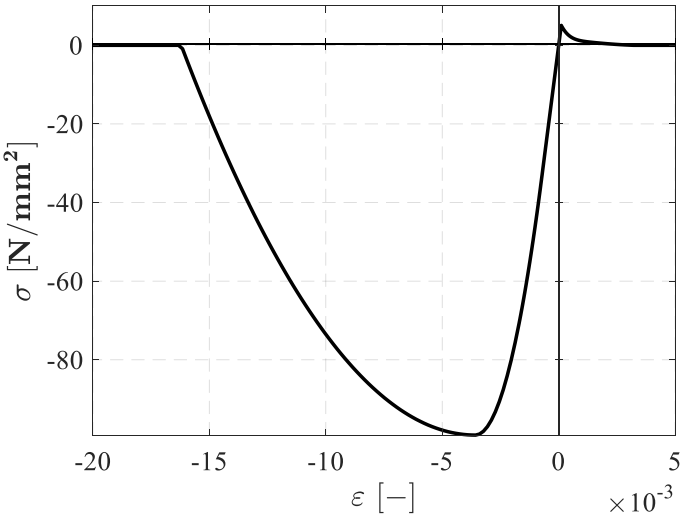

Figure 13: Case PB5. Adopted stress-strain curve for concrete (based on a crack band width of 50 mm).

[2] The ultimate strain values from Table 1, based on test specimens with length of 100 mm, are used in the model. Since the element size is approximately 50 mm (see section 2.3.4), the numerically obtained strain values may be larger than the specified ultimate strain values to cause rupture of the bar.

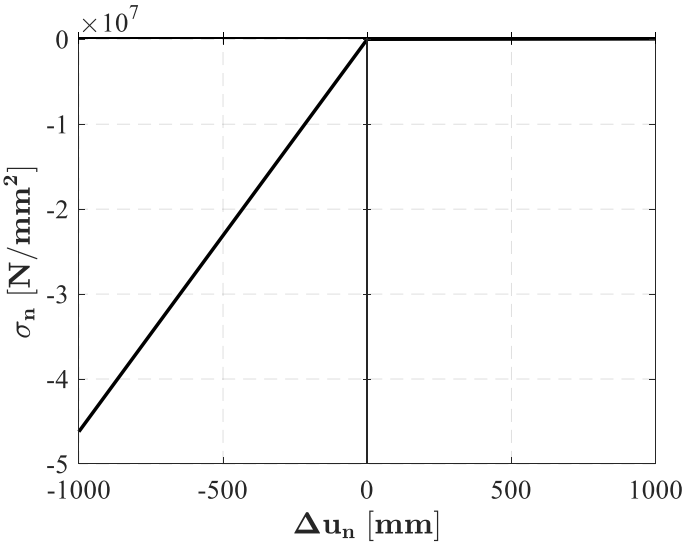

Figure 14: Case PB5. Adopted traction-displacement curve in the interface normal direction.

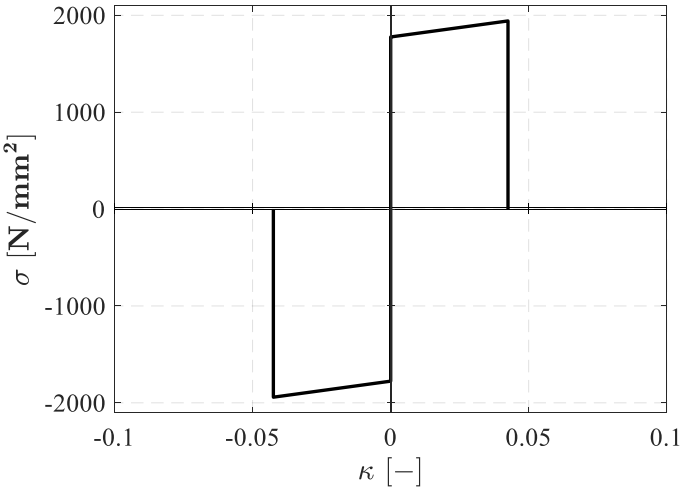

Figure 15: Case PB5. Adopted stress - equivalent plastic strain curve for the strands.

2.3.4 Element types and finite element mesh

Figure 16 shows the 2D finite element model that is used to simulate the test. The finite element model adopts three different element types: (*i*) plane stress elements; (*ii*) interface elements; and (*iii*) embedded reinforcements.

The concrete is represented by a structured mesh, consisting of quadrilateral plane stress elements based on quadratic interpolation and using a 3 x 3 (full) Gauss integration scheme. The averaged elements sizes are set to 50 mm by 50 mm. The out-of-plane thicknesses of these elements are based on Figure 12. The steel plates, that introduce the load and support forces, are modelled by the same elements.

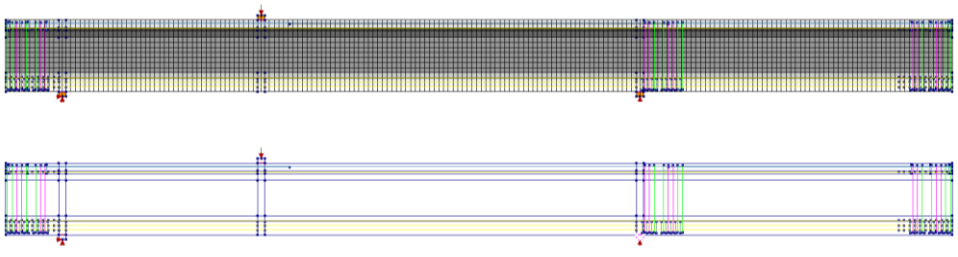

Figure 16: Case PB5. Mesh and boundary conditions (a) and embedded reinforcement sets (b).

Zero-thickness quadratic interface elements with a 3-point Newton-Cotes integration scheme are used between the steel plates and the concrete beam.

The reinforcing bars, stirrups and strands are modelled by embedded reinforcement elements with 2-point Gauss integration, assuming perfect bond between the steel and concrete. The reinforcements only have axial stiffness.

2.3.5 *Boundary conditions and loading*

Horizontal and vertical constraints are applied at the bottom mid-nodes of the support plates. According to Figure 2, the left support is constrained in *x* and *y* direction and the right support in the *y* direction only. Furthermore, a vertical constraint is attached to the top mid-node of the loading plate in order to apply the unit displacement. Three loads are considered in the simulation of the test: prestressing, dead weight and a unit displacement of 1 mm at the loading plate. The loads are applied in three separate load cases.

The prestressing load is divided over four layers of strands, which are simultaneously applied. The forces P_i per layer of strands is calculated with:

$$P_i = \sigma_{pcs} \cdot A_{p;i} \tag{1}$$

where σ_{pcs} is the stress in the prestressed strands at time of testing and $A_{p;I}$ the area of strands in layer *i*, *i* = 1…4. The stress σ_{pcs} is calculated from the averaged stress in the concrete after prestressing losses σ_{cp} = 9.56 N/mm^2, see subsection 2.1.1, using:

$$\sigma_{pcs} = \frac{\sigma_{cp} \cdot A_c}{A_p} = \frac{9.56 \cdot 194500}{1584} = 1173.9 \text{ N/mm}^2 \tag{2}$$

Due to elastic shortening a lower stress level in the strands will occur. Therefore, the strands are “overstressed” in the model in order to get the intended stress level in the strands. The required input value for σ_{pcs} is calculated from results of a linear-elastic calculation, such that σ_{cp} at the neutral line is approximately 9.56 N/mm^2.

The prestressing forces are gradually introduced (i.e. from zero to P_i) over a transmission length l_{pt}, which is calculated from the equations in section 8.10.2.2 of (CEN, 2011):

$$l_{pt} = \alpha_1 \alpha_2 \phi \frac{\sigma_{p0}}{f_{bpt}} \tag{3}$$

where:

$\alpha_1 = 1.25$ (for sudden release – as a conservative approach)

$\alpha_2 = 0.19$ (for three- and seven-wire strands)

$\phi = 12.7$ mm

$\sigma_{p0} = 1397$ N/mm^2

$f_{ctm} = 4.45$ N/mm^2 (based on f_{cm} = 71.4 N/mm^2, see subsection 2.1.2)

$$f_{ctm}(t) = \beta_{cc}(t) \cdot f_{ctm} = \exp\left(0.25 \cdot \left(1 - (28/6)^{0.5}\right)\right) \cdot 4.45 = 3.33 \text{ N/mm}^2$$

$$f_{bpt} = \eta_{p1} \cdot \eta_1 \cdot \alpha_{ct} \cdot 0.7 \cdot \frac{f_{ctm}(t)}{\gamma_c} = 3.2 \cdot 1.0 \cdot 1.0 \cdot 0.7 \cdot \frac{3.33}{1.0} = 7.45 \text{ N/mm}^2$$

(for the simulation of the test, the partial factor is set to 1.0)

As mentioned in subsection 2.1.1, the prestressing was applied six days after casting. Hence, the transmission length belonging to t = 6 is equal to 566 mm.

2.3.6 Load increments and convergence criteria

The analysis is performed in two phases. In the first phase, the loads “prestressing” and “dead weight“ are subsequently applied, both in one step. The second phase of the analysis is performed in displacement control with 16 steps of 0.25 mm, 100 steps of 0.025 mm and 75 steps of 0.2 mm. The regular Newton-Raphson method is used as solution procedure, with maximal 50 iterations per load step. An explicit line search technique is adopted in order to decrease the number of iterations per increment. A force tolerance of 1.0% and an energy tolerance of 0.1% are used as convergence criteria. The analysis is set to continue, even if the convergence criteria are not satisfied.

2.4 Nonlinear finite element analysis

This section presents the results of the analysis of case PB5. Attention is given to the load – deflection response, the convergence behaviour, the deformed meshes, the crack widths in concrete, the strains in steel, and Gauss point statistics.

2.4.1 Load – deflection

Figure 17 presents the load – deflection response of the beam during phase 2 of the analysis (black line), where the deflections are measured at the loading point. Four steps are marked with red and orange dots, corresponding to peak load values and post-peak load values respectively. These points are closer investigated in the following paragraphs. Non-converged steps are indicated with blue circles. The beam fails at a load of 745 kN. This failure load is marked by the first red dot.

The load–deflection response starts with negative deflections, indicating the upward bending due to the prestress (phase 1). In the second phase of the analysis, the displacement at the loading plate is applied, causing a downward (positive) deflection of the beam. Until load step 43, the beam behaves almost linearly. Beyond this load step a sudden load drop from 745 kN to 547 kN is visible, accompanied with the occurrence of a large diagonal crack between the left support and loading plate. The convergence behaviour of the analysis in this first post-peak regime is rather poor: almost none of the steps between the load step 44 and 74 converge. After this non-converged stage, an equilibrium path was found and the

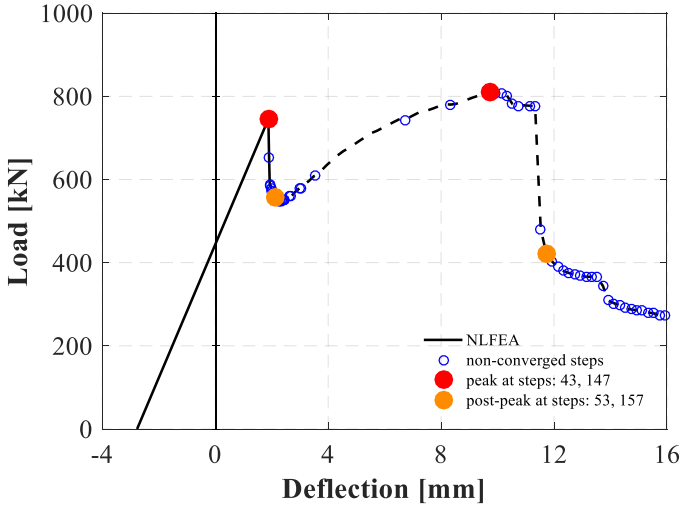

Figure 17: Case PB5. Load – deflection curve during phase 2 of the analysis.

analysis continued till load step 147 (at 809 kN) with only a few non-converged steps. From here, a second load drop occurs and none of the remaining load steps reach convergence anymore.

For the following reasons, the first load drop is considered as the structural failure of case PB5: (*i*) this load drop is quite significant; (*ii*) it is accompanied by the appearance of a large diagonal crack; (*iii*) the analysis did not converge for many steps after this load drop; (*iv*) from the physical point of view it is more realistic to assume that after the first load drop the beam has no residual load capacity anymore, due to dynamic effects caused by the sudden energy release and the absence of shear reinforcement in the web. The remaining part of the numerically obtained load – deflection response may be a result of the quasi-static displacement-controlled loading procedure, but is deemed as not reliable in this case. Therefore, the second part of the curve is plotted with a dashed black line.

2.4.2 Convergence behaviour

Figure 18 shows the evolutions of the relative out of balance force and relative energy variation during the analysis. The red and orange dots refer to the characteristic points in the load – deflection curve, see Figure 17. The black lines in the two graphs indicate the force norm and energy norm respectively.

Before load step 43, phase 2 of the analysis converges on the basis of the force norm. The energy norm is not considered in this stage, since the load steps converge without iterations. Right after load step 43 it is shown that both the force norm criterion and (especially) energy norm criterion are far from being reached. Between the load steps 75 and 147, the convergence is reached on the basis of the energy norm. From (and including) load step 147, none of the steps satisfy the convergence criteria anymore and the force and energy norms reveal a diverging trend.

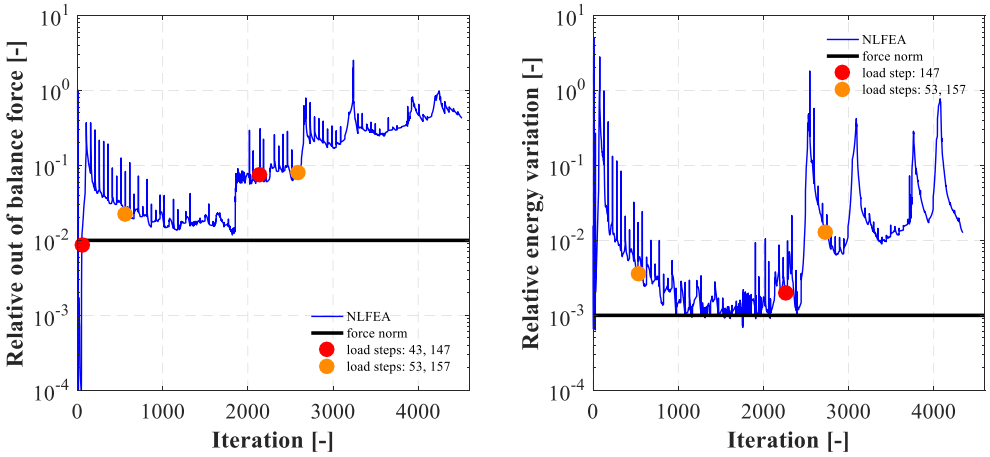

Figure 18: Case PB5. Evolutions of the relative out of balance force and relative energy variation.

2.4.3 *Deformed meshes*

Figure 19 presents the meshes with normalized deformations at the load steps 43, 53, 147 and 157. The plots clearly indicate the occurrence of a diagonal crack between the left support and the loading plate. During the second ascending branch of the load – deflection response, between the load steps 53 and 147, the elements in the diagonal crack further deforms. In load step 157 different elements show a distorted shape, which indicates that the element stiffness entirely vanished.

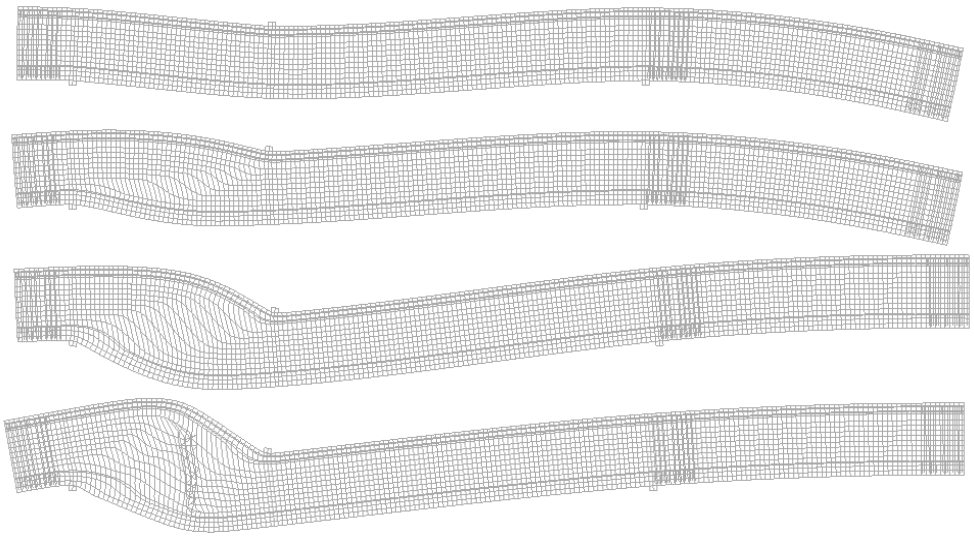

Figure 19: Case PB5. Deformed meshes at the load steps 43, 53, 147 and 157, see Figure 17.

2.4.4 *Crack widths and principal strains in concrete*

Figure 20 presents the crack widths plots at the load steps 43, 53, 147 and 157. Figure 21 and Figure 22 present the plots with the maximum principal strains (ε_1) and minimum principal strains (ε_2) at these load steps respectively. These plots show again the (sudden) appearance of the diagonal crack (or strain localizations) at load step 43, with values far beyond the softening branch of the stress – crack width relation (or stress – strain relation). However, in the numerical analysis a force transfer mechanism can occur and the beam is prevented from total failure (though the convergence behaviour right after load step 43 is rather poor). This can happen

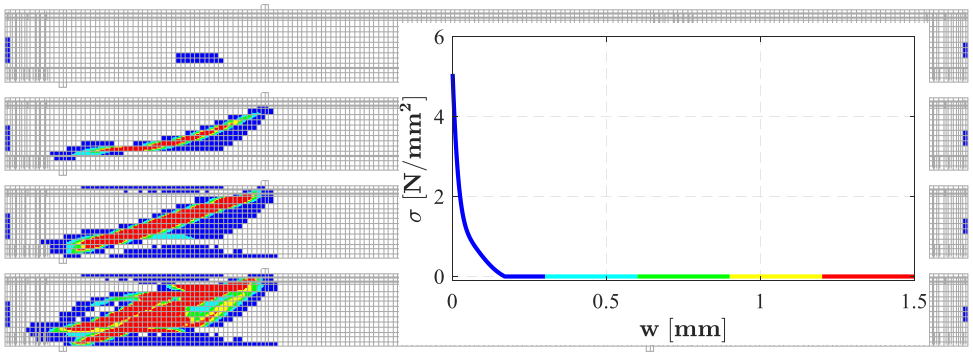

Figure 20: Case PB5. Crack width plots at the load steps 43, 53, 147 and 157, see Figure 17.

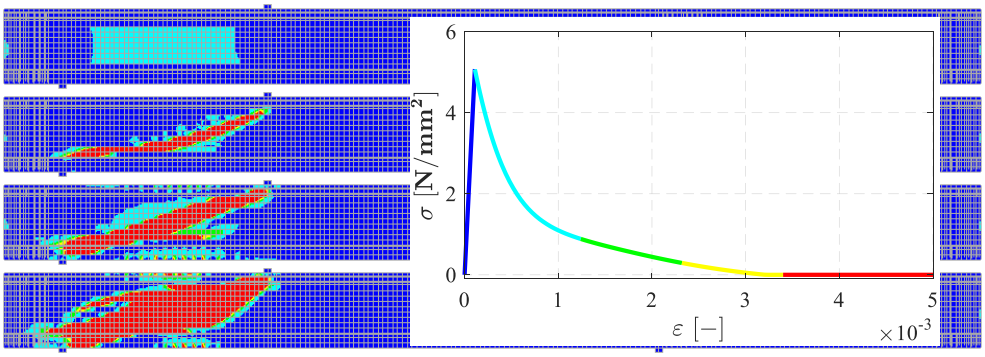

Figure 21: Case PB5. Maximum principal strain plots (ε_1) at the load steps 43, 53, 147 and 157, see Figure 17.

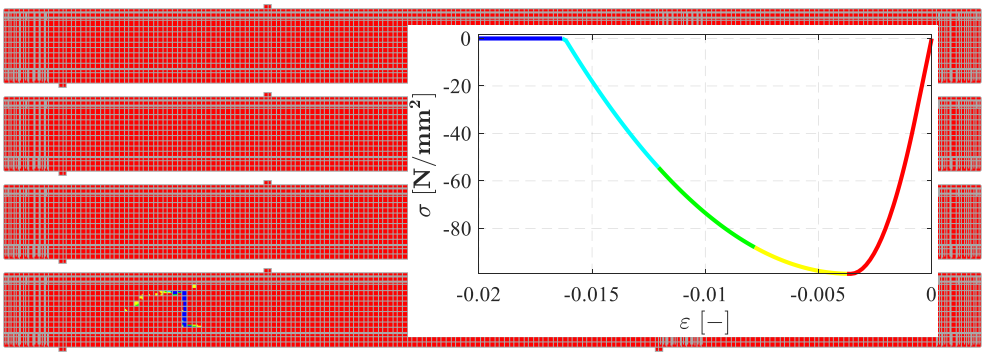

Figure 22: Case PB5. Minimum principal strain plots (ε_2) at the load steps 43, 53, 147 and 157, see Figure 17.

because (*i*) the left-bottom end of the diagonal crack stops at the left support; (*ii*) the prestressed strands are far from yielding; and (*iii*) the compression zone at the right-top end of the diagonal crack is still intact. In the stage between the load steps 53 and 147 the crack widths at the integration points and the band width of the diagonal crack further increase. At load step 157, almost the entire shear zone is cracked and at the location of the distorted elements (see the last plot in Figure 19), crushing of the concrete can be observed (see the last plot in Figure 22). Note that the results of the last two load steps belong to an unreliable equilibrium path.

2.4.5 *Strains in steel*

Figure 23 presents the strains in the reinforcing bars and prestressed strands at the load steps 43, 53, 147 and 157. The colour legend scale is related to the stress – equivalent plastic strain curve for the strands. Yielding of the strands is observed when the second peak in the load – deflection response is reached and beyond this second peak (indicated by the red circles). The reinforcing bars did not yield in the analysis. Note that the results of load steps 147 and 157 belong to an unreliable equilibrium path.

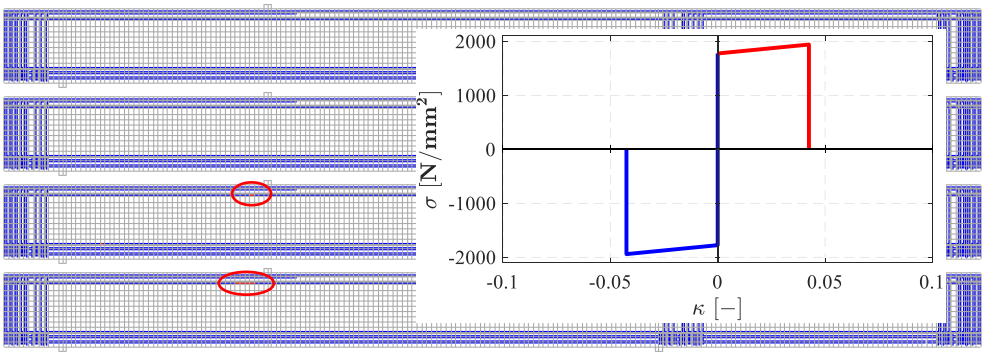

Figure 23: Case PB5. Strains in reinforcing bars and strands at the load steps 43, 53, 147 and 157, see Figure 17.

2.4.6 *Gauss point statistics*

Figure 24 presents the evolutions of the number of Gauss points with earlier and present plastic behaviour (crushing or yielding) and the number of cracked Gauss points. The graphs clearly highlight the two events around the load steps 43 and 147, as described before.

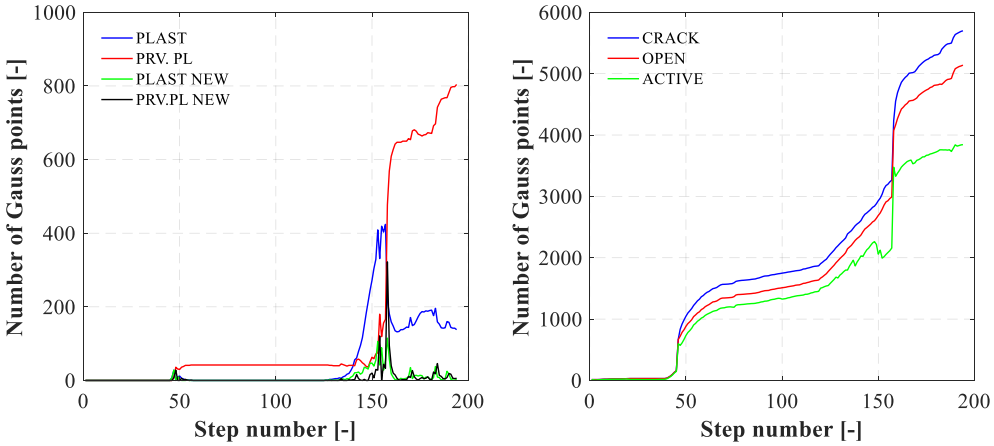

Figure 24: Case PB5. Evolutions of the number of Gauss points with (former) plastic behaviour (crushing or yielding) and the number of cracked Gauss points.

2.5 Application of safety formats for nonlinear finite element analysis

This section demonstrates the application of the three safety formats *global resistance factor method* (GRF), *estimation of the coefficient of variation of the resistance* (E-COV) and the *partial factor method* (PF), as proposed in *fib* Model Code 2010 (CEB/fib, 2012). In total, four different nonlinear finite element analyses need to be performed.

Table 4 to Table 8 summarize the input geometry and material parameters of the concrete, reinforcing bars and strands for the four analyses. The input parameters are based on the mean values, characteristic values, mean GRF values and design values, which are calculated according to Annex A of (Rijkswaterstaat, 2017a). According to this annex, only material properties are changed and the geometry properties are kept constant.

For the analysis with design values, the load increment scheme is changed and slightly differs from the one discussed in subsection 2.3.6.

Table 4: Case PB5. Concrete properties for the nonlinear analyses of the safety formats.

	f_c (N/mm^2)	f_{ct} (N/mm^2)	E_c (N/mm^2)	v (-)	G_f [3] (N/mm)	G_c (N/mm)
Mean	99.15	5.07	46189	var	0.1670	41.74
Characteristic	91.15	3.55	44911	var	0.1645	41.12
Mean GRF	77.48	4.60	42543	var	0.1597	39.93
Design	60.77	2.36	39234	var	0.1529	38.22

Table 5: Case PB5. Stirrup properties for the nonlinear analyses of the safety formats.

	Ø (mm)	A_s (mm^2)	f_y (N/mm^2)	f_t (N/mm^2)	E_s (N/mm^2)	ε_{sy} (-)
Mean	8.0	50.27	525.38	660.63	200000	0.0026
Characteristic	8.0	50.27	475.86	598.36	200000	0.0024
Mean GRF	8.0	50.27	523.45	658.20	200000	0.0026
Design	8.0	50.27	413.79	520.31	200000	0.0021

Table 6: Case PB5. Properties of the longitudinal reinforcing bars Ø8 for the nonlinear analyses of the safety formats.

	Ø (mm)	A_s (mm^2)	f_y (N/mm^2)	f_t (N/mm^2)	E_s (N/mm^2)	ε_{sy} (-)
Mean	8.0	50.27	556.50	664.00	200000	0.0028
Characteristic	8.0	50.27	504.04	601.41	200000	0.0025
Mean GRF	8.0	50.27	554.45	661.55	200000	0.0028
Design	8.0	50.27	438.30	522.97	200000	0.0022

[3] Note that the variations in the fracture energies G_f and G_c are surprisingly small and their values do not proportionally change with the values of the tensile strength f_t and compressive strength f_c.

Table 7: Case PB5. Properties of the longitudinal reinforcing bars Ø10 for the nonlinear analyses of the safety formats.

	Ø (mm)	A_s (mm²)	f_y (N/mm²)	f_t (N/mm²)	E_s (N/mm²)	ε_{sy} (-)
Mean	10.0	78.54	581.00	691.00	200000	0.0029
Characteristic	10.0	78.54	526.24	625.87	200000	0.0026
Mean GRF	10.0	78.54	578.86	688.46	200000	0.0029
Design	10.0	78.54	457.60	544.23	200000	0.0023

Table 8: Case PB5. Strand properties for the nonlinear analyses of the safety formats.

	Ø (mm)	A_s (mm²)	f_y (N/mm²)	f_t (N/mm²)	E_s (N/mm²)	ε_{sy} (-)
Mean	12.7	99	1776.0	1941.4	192940	0.0092
Characteristic	12.7	99	1608.6	1758.4	192940	0.0083
Mean GRF	12.7	99	1769.5	1934.2	192940	0.0092
Design	12.7	99	1398.8	1529.1	192940	0.0072

Figure 25 presents the load – deflection curves of the analyses with mean values, characteristic values, mean GRF values and design values for the input parameters of the concrete, reinforcing bars and strands. Their corresponding peak values are 745 kN, 607 kN, 708 kN and 466 kN respectively, which reveals a strong correlation between the predicted load capacity and the tensile strength. The analyses with characteristic values, mean GRF values and design values reveal a similar failure behaviour as the analysis with mean values, though the shapes of the failure cracks are different, see Figure 26. Using the expressions provided by Annex A of (Rijkswaterstaat, 2017a), the design resistances for the safety formats can be calculated. These values are compared in Figure 27 and Table 9, together with the results of the analytical calculations from subsection 2.2.4. The resistances based on mean values of the input parameters are also added. Note that the analysis with label “No safety format” refers to the analysis with mean values, discussed in the previous section.

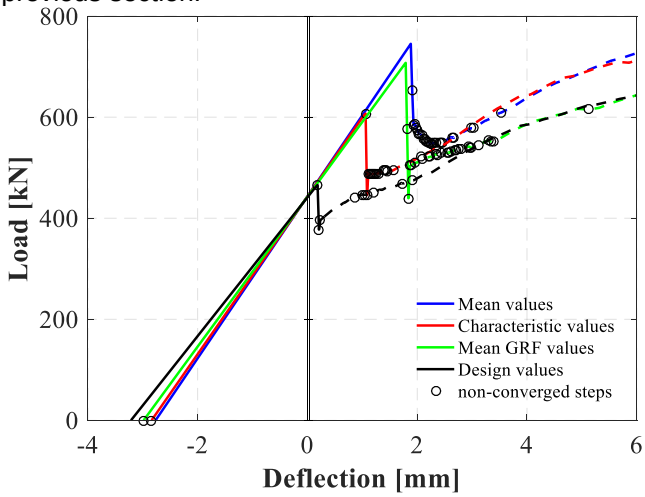

Figure 25: Case PB5. Load – deflection curves of the analyses with mean values, characteristic values, mean GRF values and design values for the input parameters of the concrete, reinforcing bars and strands. The graph with the entire numerically obtained responses is shown in Annex A.

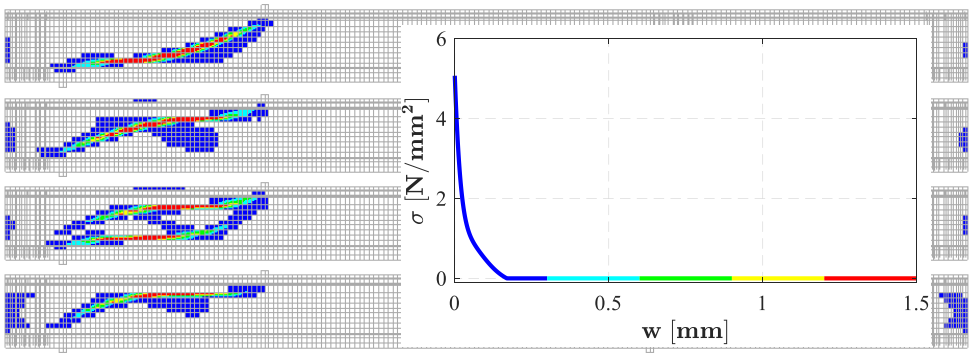

Figure 26: Case PB5. Crack width plots after the load drop for the analyses with mean values, characteristic values, mean GRF values and design values.

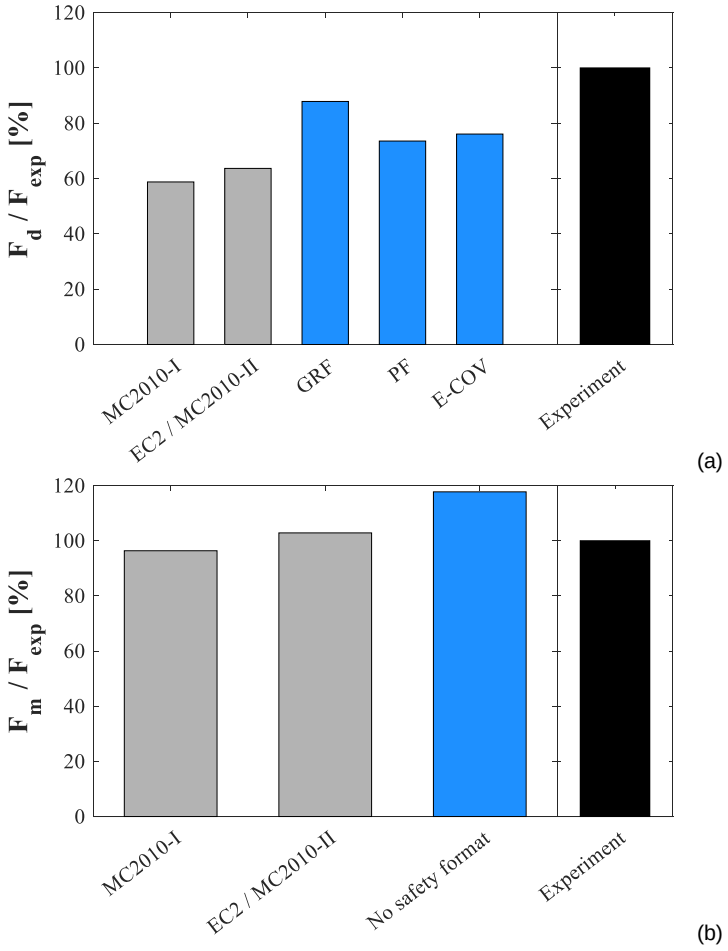

Figure 27: Case PB5. Design values of the resistance (F_d) according to the different safety formats (a) and the resistances (F_m) based on the mean values of the input parameters (b), expressed in terms of a percentage of the experimentally obtained ultimate load (F_{exp}). The grey colour bars refer to the calculations with symbolic expressions, the blue colour bars to the nonlinear finite element analyses.

Table 9: Case PB5. Design values of the resistance according to the different safety formats and the resistances (F_m) based on the mean values of the input parameters (in kN).

	Design values (F_d)					**Mean input (F_m)**		
F_{exp}	*MC2010 level I*	*EC2 / MC2010 level II*	*GRF*	*PF*	*E-COV*	*MC2010 level I*	*EC2 / MC2010 level II*	*No safety formats*
633	372	403	556	466	482	610	651	745

2.6 Sensitivity analysis

This section investigates the sensitivity of the numerical results of the previous analysis with mean values with respect to the (*i*) crack model; (*ii*) the level of prestressing force; (*iii*) the geometrical representation / element type, and (*iv*) the tensile strength of the concrete. The variations are explained in the following.

Crack model: In this analysis the rotating crack model is replaced by a fixed crack model. All the other modelling aspects are the same as described in section 2.3. The fixed crack model requires the specification of a shear retention relation. In this study, the damaged based shear retention relation and the aggregate size based shear retention relation are considered. In the former relation, the shear retention *G* depends on the normal stiffness decay (and so on the crack normal strain), via:

$$G = \frac{E_n}{2\left(1+\nu\right)} \tag{4}$$

In the latter relation, the shear retention factor β depends on the aggregate size d_{aggr}, the crack normal strain ε_n and the crack band width *h*, via:

$$\beta = 1 - \left(\frac{2}{d_{aggr}} \right) \cdot \varepsilon_n \cdot h \tag{5}$$

The damaged based shear retention relation is characterized by a relatively rapidly decreasing shear stiffness and the aggregate size based shear retention relation is characterized by a relatively slow decreasing shear stiffness.

Level of prestressing force: In this analysis the prestressing force *P* is increased by 10%. All the other modelling aspects are the same as described in section 2.3. In the context of ULS verification, the level of *P* is less importance in case of problems with bending failure. However, in case of problems with shear failure the level of *P* can be quite important, since it will determine the (bending) crack development and the principal stress distribution in the structure.

Geometrical representation / element type: In this analysis the beam is modelled by shell elements with quadratic interpolation. The model has a T-shape in cross-sectional view, meaning that the top flange is modelled by “out-of-plane” shell elements and the web and bottom flange are modelled by “in-plane” shell elements. Figure 28 shows the thickness directions and their thicknesses in the adopted cross-sectional discretization. The shell elements are modelled in the center lines of

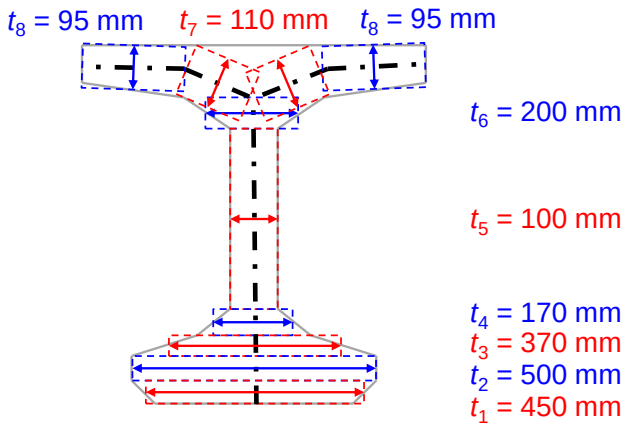

Figure 28: Case PB5. Cross-sectional discretization for the shell element model.

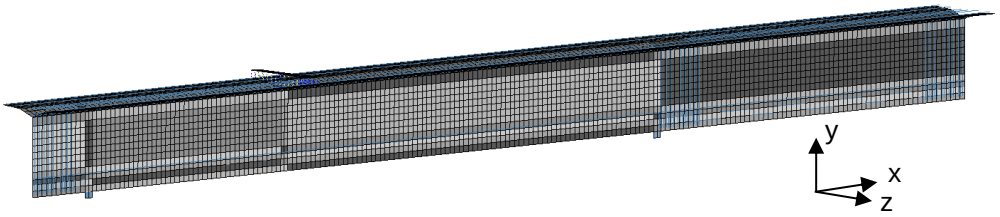

Figure 29: Case PB5. Mesh of the shell element model.

the flanges and web, except in top flange – web connection. Hence, the cross-sectional area and moment of inertia in the model differ from the real cross-sectional area and moment of inertia. All the other modelling aspects of this shell element model are the same as described in section 2.3. Figure 29 shows the mesh of the shell element model.

Note that the adopted cross-sectional discretization in the shell element model is only one of the possibilities. Other cross-sectional discretization's may be equally valid. Though there is some overlapping material in the top flange – web connection, this model is considered as a conservative approach, because: (*i*) the moment of inertia and *y* coordinate of the center of gravity are lower compared to the real beam; (*ii*) some material in the parts with thickness t_7 is neglected.

Tensile strength of the concrete: In this analysis the mean value of the concrete tensile strength is reduced by 32.8%, leading to $f_t = 0.672\ f_{t;m}$. The load increment scheme is changed and slightly differs from the one discussed in subsection 2.3.6. All the other modelling aspects are the same as described in section 2.3.

Figure 30 presents the load – deflection responses of the sensitivity analyses. The maximum obtained load capacities are summarized in Table 10. From the comparison with the results of the reference analysis in section 2.4, it is noted that the adopted crack model has no influence on the results until the peak. This is not surprising, since the beam behaves almost linearly in this regime and the failure load is mainly determined by the tensile strength. The extent of load drop depends on the crack model and shear retention relation.

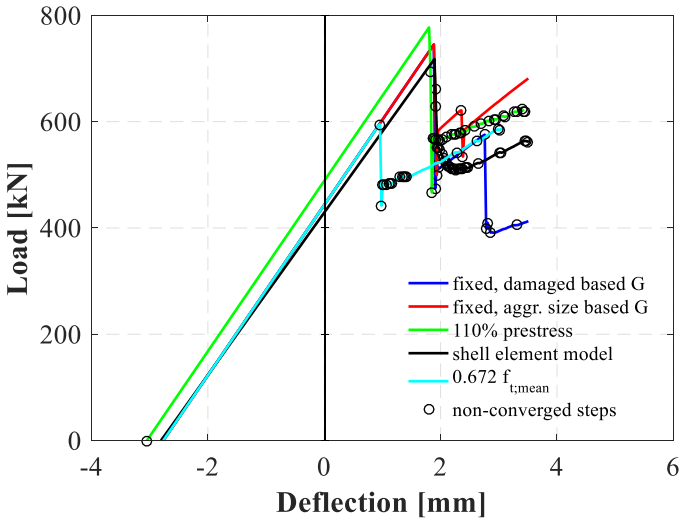

Figure 30: Case PB5. Load – deflection curves of the sensitivity analyses. The graph with the entire numerically obtained responses is shown in Annex A.

Table 10: Case PB5. Maximum load capacities of sensitivity analyses.

Analysis	Maximum load capacity (kN)
Reference analysis (“No safety format”, mean values)	745.2
Fixed crack model – damaged based shear retention	745.2
Fixed crack model – aggr. size based shear retention	745.2
10% higher prestressing force	777.2
Shell element model	717.9
Reduced tensile strength of the concrete	594.8

The level of prestress slightly affect the maximum load capacity of the beam. An increase of 10% in the prestressing force leads to an increase of 4.3% in load capacity.

Using shell elements instead of plane stress elements have also limited effects on the results. The shell element model reveals some less stiff behaviour and results in a 3.7% lower failure load. These observations can be explained by the adopted cross-sectional discretization, which leads to a lower moment of inertia and a lower *y* coordinate of the center of gravity compared to the real beam. As a result of that, the bending stiffness and the eccentricity of the prestressing force to the centroidal axis of the beam (i.e. the bending moment due to prestressing force) are decreased.

The adopted value of the tensile strength of the concrete clearly affects the maximum load capacity. A reduction of 32.8% in the tensile strength results in a reduction of 20.2% in the peak load.

For the sake of completeness, Figure 31 shows the crack width plots after the load drop for each analysis. The crack patterns show reasonably agreement, except for the analyses “fixed, damaged based G” and “110% prestress”.

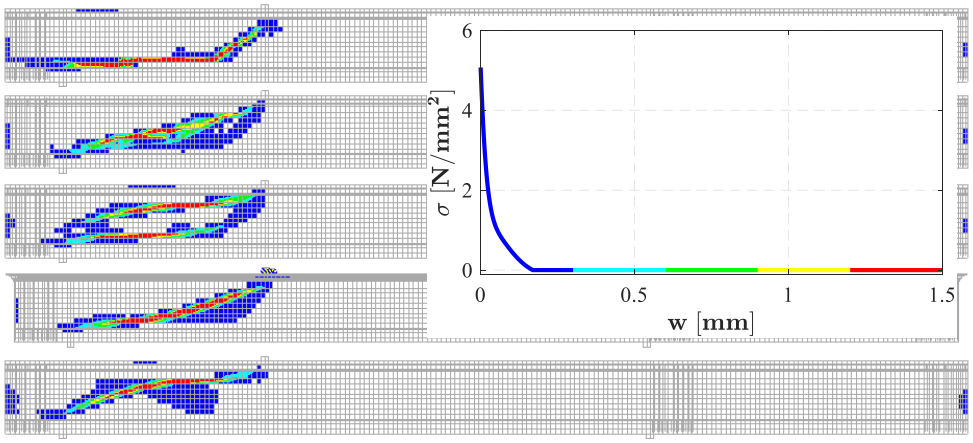

Figure 31: Case PB5. Crack width plots after the load drop for the analyses “fixed, damaged based G”, “fixed, aggr. size based G”, “110% prestress”, “shell element model”, and “0.672 $f_{t;mean}$”.

2.7 Concluding remarks

The failure mechanism and the sequence of events are well simulated by the numerical analyses. Table 11 compares the numerically and experimentally obtained loads for different events. Mean values of the material properties have been used in the numerical analysis. The load at the occurrence of the first diagonal crack is considered as the ultimate load capacity. To rely on a possible higher ultimate load capacity, utilizing the predicted post-peak regime, is not prudent for this specimen without shear reinforcement that failed in a brittle way.

Considering a mean concrete tensile strength according to (CEB/fib, 2012), the numerical analysis overestimates the load level at the first diagonal crack by 18%. The numerical analysis overestimates the maximum observed load level by 4%. The significant influence of the concrete tensile strength on the first peak load level is evident from the failure mechanism and is quantified by the variation study.

The application of the safety formats for nonlinear finite element analysis of concrete structures shows a relatively high design resistance of 556 kN (i.e. 88% of F_{exp}) for the GRF method, compared to the PF and E-COV method. The safety formats for nonlinear finite element analysis lead to significant higher design resistances than the ones based on symbolic expressions.

Table 11: Case PB5. Comparison between numerical results and experimental results (mean values).

	f_{ctm} (MPa)	NLFEA (kN)	Experiment (kN)
Load first crack	5.07 3.41	745 595	633 (considered as ultimate capacity)
After first peak load	5.07	547	509 (considered as not reliable)
Maximum load	5.07	809	778 (considered as not reliable)

The sensitivity analyses show that the use of shells elements leads to a lower ultimate load capacity compared to reference analysis with a plane stress element model, provided that care is taken for the cross-sectional discretization. This is an important observation from the practical point of view when considering the modelling of bridge structures.

3 Case PB6: Choulli, Mari, Cladera, girder with stirrups (2005)

This chapter describes the experimental setup and results, analytical analysis, finite element modelling, numerical analyses and the application of safety formats for nonlinear finite element analysis for the prestressed concrete beam that is denoted with *case PB6*. Case PB6 is a pre-tensioned I-shaped beam with stirrups. It concerns specimen HCP1TW in the experiment of Choulli (2005). Compared to case PB5 (see the previous chapter), case PB6 has the following differences: (*i*) it has a lower value for f_{cm}; (*ii*) it has longitudinal reinforcing bars and stirrups in the web; (*iii*) the distance between the right support and the east end of the beam is shorter; and (*iv*) it has a longer period between casting and testing of the beam.

3.1 Experimental setup and results

This section provides the details of the experimental setup in terms of geometry of the beam, material properties and boundary conditions. Furthermore, the result of the test is described.

3.1.1 Geometry

Figure 32 shows the geometry, the reinforcement layout and the location of the prestressing strands of the beam. A more detailed view on the reinforcements and strands is shown in Figure 33. The beam has an I-shaped cross-section, a length of 10.0 m and a total depth of 0.75 m. The longitudinal reinforcement in the web of the beam consists of two times 3 Ø10 mm with 160 mm spacing at the west half of the beam and two times 5 Ø10 mm with 80 mm spacing at the east half of the beam.

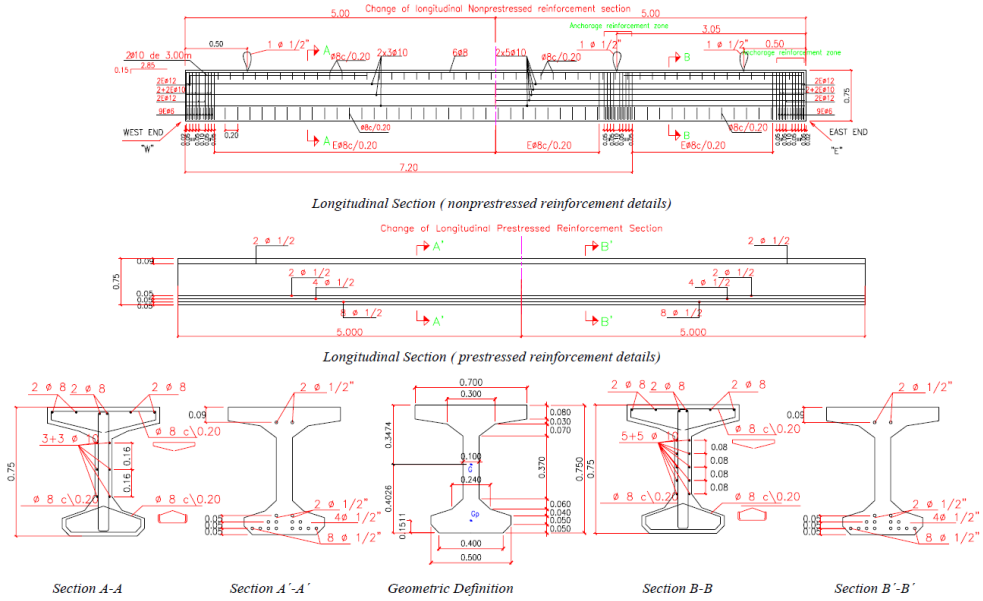

Figure 32: Case PB6. Geometry, reinforcement layout and location of prestressing strands (dimensions in m). The pictures are taken from (Choulli, 2005).

Figure 33: Case PB6. Reinforcement cage and prestressing strands. The picture is taken from (Choulli, 2005).

The transversal reinforcement in the web along the beam is Ø8 mm stirrups with 200 mm spacing. Furthermore, the top flange contains six Ø8 mm reinforcing bars over the entire length of the beam and two Ø10 mm rebars of 3.0 m length at both ends of the beam. Stirrups of Ø8 mm with 200 mm spacing are placed in the top and bottom flanges. The anchorage zone of the prestressing strands contains stirrups of Ø10 mm and Ø12 mm in the web (from bottom flange to top flange) and bottom flange, over an approximately 0.45 m distance from each end. This set of stirrups is also placed at 3.0 m of the east end.

The prestressing force is transferred by sixteen straight bonded strands 0.5” in a long line process, with an area A_p of 99 mm^2 per strand. The total area of prestressing strands in the beam equals 1584 mm^2. The initial stress in the prestressing steel without losses σ_{p0} equals 1397 N/mm^2. The averaged initial stress in the concrete σ_{cp} without prestressing losses equals 11.37 N/mm^2. The averaged initial stress in the concrete σ_{cp} at the day of testing (incl. losses due to elastic shortening of the concrete, creep, shrinkage and relaxation) equals 9.56 N/mm^2. The prestressing force was applied six days after casting. Testing was performed 94 days after casting.

3.1.2 Material properties

Table 12 summarizes the provided concrete, reinforcement and strand properties. The mean concrete cylinder compressive strength f_{cm} of 81.17 N/mm^2 is obtained from the results of standard 150 mm x 300 mm cylinder tests (at the day of testing). The mean concrete cylinder compressive strength at six days after casting equals 65 N/mm^2.

3.1.3 Boundary conditions and loading

Figure 34 shows the test setup of case PB6. The simply supported beam was subjected to a three-point bending test. The beam had a fixed support near the applied load (west side) and a sliding support on the other side (east side). The test consisted of two stages. In the first stage, the east side of the beam was tested. In the second stage, the west side of the beam was tested. The current analysis concerns the second stage of testing. During this stage of testing, a displacement

Table 12: Case PB6. Properties of concrete, reinforcement and prestressing strands.

Concrete properties	
f_{cm} (N/mm^2)	d_{max} (mm)
81.17	12

Reinforcement and strand properties							
	Steel	Corru-gation	Ø (mm)	E_s (N/mm^2)	f_{ym} (N/mm^2)	f_{tm} (N/mm^2)	ε_u (%)
Stirrups	B500S	0.57	8.0	NA	525.38	660.63	26.9*
Long. bars Ø8	B500SD	0.58	8.0	NA	556.50	664.00	25.0*
Long. bars Ø10	B500SD	0.79	10.0	NA	581.00	691.00	24.0*
Strands	Y1860 S7 13.0	-	12.7	192940	1776	1941.4	5.17

* The ultimate strain is determined from test specimens with length of 100 mm.

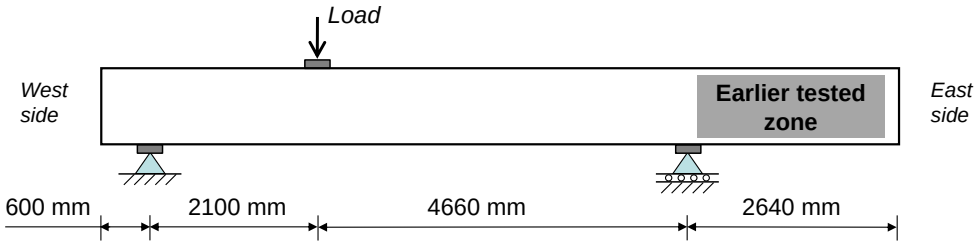

Figure 34: Case PB6. Loading and boundary conditions (dimensions in mm).

Figure 35: Case PB6. Overview of the test setup during testing the west side of the beam.

controlled load was placed at 2.1 m distance from the left support. The load was applied by a hydraulic jack, using a closed loop hydraulic MTS 1100 KN equipment. The loading rate varied from 0.3 mm/min to 1 mm/min. The dimension of the load plate was 75 mm. The beam was monotonically loaded until failure. Figure 35 shows the test setup during testing of the west side of the beam.

3.1.4 Experimental results

Figure 36 shows the obtained load-deflection response. The first major cracks were diagonal shear cracks that appeared at a load level of 606 KN with an angle of 30 degrees to the horizontal axis (see Figure 37), accompanied with a small load drop. Subsequently, the applied load increased again due to important contributions from the strands, the longitudinal reinforcement and especially the transversal reinforcement. Strain gauges on the web reinforcement E3PT and WIPLM (see Figure 38) recorded important strains at the diagonal shear cracking load, and next they registered strains that exceed the strain value corresponding to the yield strength. Fracture of the shear reinforcement was not observed. None of the prestress tendons or longitudinal reinforcement did reach their yield strength at any time during the test. Drops in the load followed the development of diagonal cracks (hardly visible at this scale in Figure 36). These cracks appeared at right and left, and more or less parallel to, of the first and main inclined crack. The formation of the cracks reduced the stiffness of the girder. The load level at which flexural cracking occurred was larger than what theoretically was expected. They occurred prior to the formation of the first diagonal shear cracks at centre span. Before recording the test data, a load of about 30 kN was applied to stabilize the test system. This load is added to the reported values of the external load. The maximum observed load level is 1069 kN at a deflection of 27.7 mm.

Quoting Choulli (2005), the following failure processes took place for the girders with stirrups. “All beam specimens failed in shear. The final collapse of the beams ends took place after the yielding of the stirrups. Once the stirrups yielded, the shear compression fields could rotate to a minor angle, increasing the stress in the struts. Finally, shear failure resulted from a diagonal tension and crushing of the concrete in the web”. Specific for girder PB6 the following description of the failure process was added: “The final collapse of the beam end resulted from a diagonal tension failure in the web with the yielding of shear reinforcement according to recorded test data by strain gauges”. Pictures of the observed cracks are provided in Figure 39 to Figure 41.

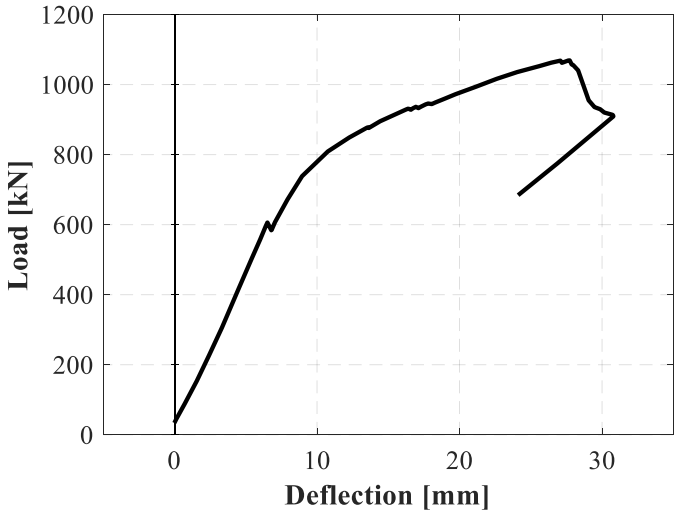

Figure 36: Case PB6. The experimentally obtained load – deflection curve.

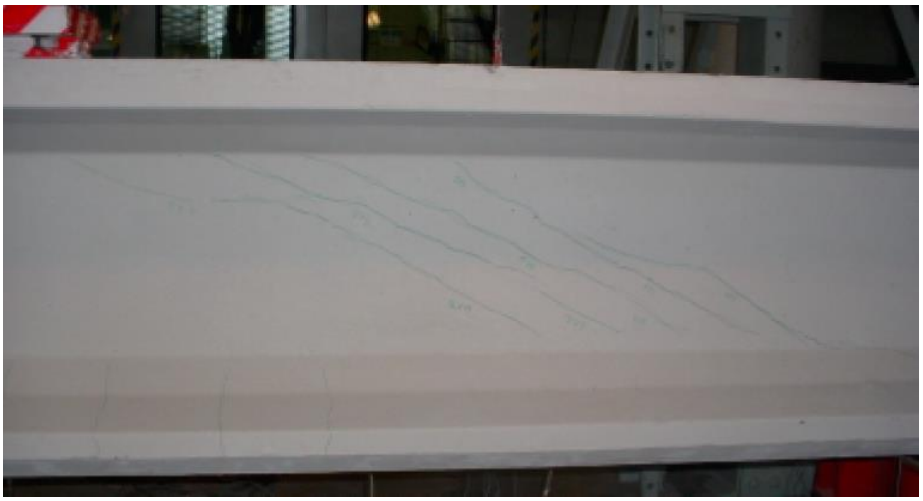

Figure 37: Case PB6. Development of the first diagonal shear cracks in the girder. The picture is taken from (Choulli, 2005).

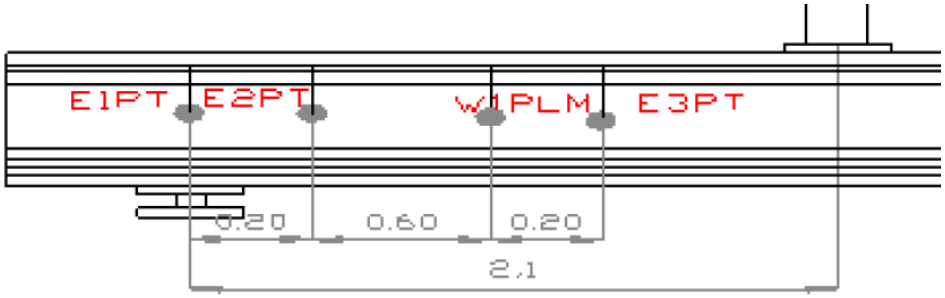

Figure 38: Case PB6. Locations of the strain gauges on the stirrups. The picture is taken from (Choulli, 2005).

Figure 39: Case PB6. Details of the girder at failure. The picture is taken from (Choulli, 2005).

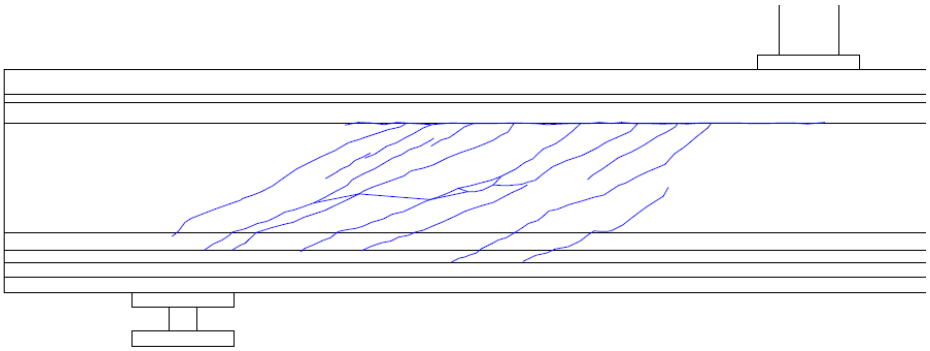

Figure 40: Case PB6. Crack pattern at failure. The picture is taken from (Choulli, 2005).

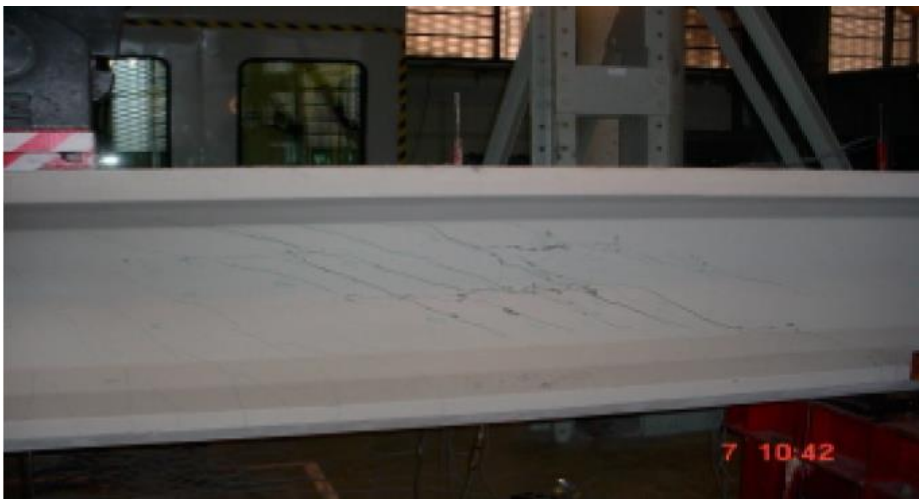

Figure 41: Case PB6. Longitudinal crack at the mid-web depth. The picture is taken from (Choulli, 2005).

3.2 Analytical analysis

3.2.1 Cross-sectional properties

Figure 42 shows the cross-section of the girder. The corresponding cross-sectional properties are:

- the area of the cross-section A: 194500 mm^2,
- the second moment of area I: = 1.50·10^{10} mm^4,
- the first moment of area (axis top flange-web) S_{tf}: 2.39·10^7 mm^3,
- the first moment of area (centroidal axis) S_c: 2.53·10^7 mm^3,
- the first moment of area (axis bottom-flange web) S_{bf}: 2.33·10^7 mm^3.

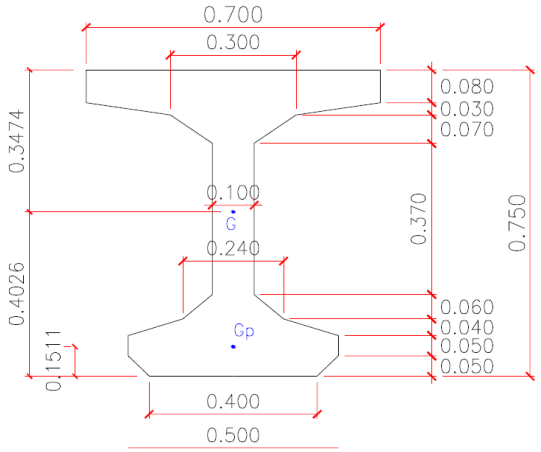

Figure 42: Case PB6. Cross-section. The picture is taken from (Choulli, 2005).

3.2.2 *Cross-sectional forces due to the loads*

In the following, the moments and shear forces due to dead weight, the prestressing force and the point load at midspan are calculated.

Dead weight

Figure 43 shows the static scheme of the girder subjected to the dead weight. Assuming a density for the reinforced concrete ρ_c of 2500 kg/m^3, the moments and shear forces between the supports due to this load are calculated as follows:

$q_{dw} = A \cdot \rho_c = 0.1945 \cdot 25 = 4.86$ kN/m
$R_{1,dw} = (10/2 - 2.64)/ 6.76 \cdot 10 \cdot q_{dw} = 17$ kN (vertical reaction force of left support)
$V_{E,dw} = -0.6 \cdot q_{dw} + R_{1,dw} - 4.86 \cdot x = 14.1 - 4.86 \cdot x$ $[0 < x < 6.76]$
$M_{E,dw} = 17 \cdot x - ½ \cdot 4.86 \cdot (x + 0.6)^2$ $[0 < x < 6.76]$

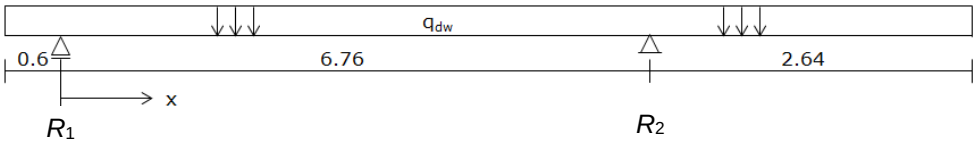

Figure 43: Case PB6. Dead weight load.

Prestressing force

The moments and shear forces due to the prestressing force are calculated as follows:

σ_{cp} = 9.56 N/mm^2 (after losses)
$N_{E;all} = A_c \cdot \sigma_{cp} = 1859$ kN
$N_{E,td} = 1859 / 16 = 116$ KN
$d_{p,top}$ = 90 mm (see Figure 32)
$d_{p,bottom} = (2 \cdot 600 + 4 \cdot 650 + 8 \cdot 700) / 14 = 671$ mm (from top side)
$V_p = 0$
$M_p = 14 \cdot 116 \cdot (0.347 - 0.671) + \ldots$
$2 \cdot 116 \cdot (0.347 - 0.090) = -467$ kNm

Note that the prestressing force is fully introduced in the cross-section above the left support, since the transmission length of the tendons equals 589 mm (see 3.3.5).

External point load
Figure 44 shows the static scheme of the girder subjected to the point load. The corresponding moments and shear forces are:

$V_{E,F}$ = 4.66 / 6.76 · F [0 < x < 2.1]
$M_{E,F}$ = 4.66 / 6.76 · F · x [0 ≤ x ≤ 2.1]

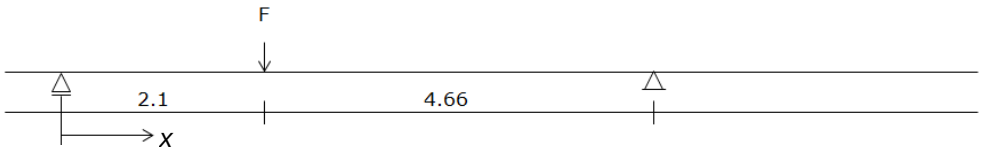

Figure 44: Case PB6. External point load.

3.2.3 Bending moment resistance

The analytical approaches predicts shear tension failure prior to flexural cracking (which is shown in the next subsection). Hence, the bending moment resistance will not be governing.

3.2.4 Shear force resistance

The Model Code 2010 (CEB/fib, 2012) offers two levels of approximations for the calculation of the shear resistance of hollow core slabs and similar structural members without shear reinforcement. According to Model Code 2010, shear failure for these members occurs when the principal tension stress demand in the web exceeds the tensile strength of the concrete.

In the following, the shear resistance of the girder is determined by using both level of approximations. The level II approximation is equal to the Eurocode approach (CEN, 2011).

Shear resistance Eurocode/ Model Code level II, based on mean values
First, the shear resistance is calculated using the design provision for members with shear reinforcement. It is assumed that z = 0.9 · $d_{p,top}$ = 0.9 · 671 = 604 mm. The lowest allowable angle θ between the concrete compression strut and the beam axis perpendicular to the shear force is assumed, which is 21.8˚. Hence, the shear resistance equals:

$$V_{R,s} = \frac{A_{sw}}{s} \cdot z \cdot f_{yw} \cdot \cot\theta$$
$$= \frac{100.5}{200} \cdot 604 \cdot 525 \cdot 2.5 = 398 \cdot 10^3\ N$$

The value of $V_{R,s}$ is limited to $V_{R,max}$ that is determined based upon α_{cw} = (1 + 9.56 / 81.17) = 1.11 and v_1 = 0.6 (1 – 81.17/250) = 0.41. Even with the low angle of θ = 21.8˚, this limiting value for the compressive strut is not governing:

$$V_{R,max} = \alpha_{cw} \cdot b_w \cdot z \cdot v_1 \cdot f_{cm} / (\cot\theta + \tan\theta)$$
$$= 1.11 \cdot 100 \cdot 604 \cdot 0.41 \cdot 81.17/2.9 = 769 \cdot 10^3\ N$$

With $V_{E,dw}$ = 12 kN at x =0.44, the maximum point load F that can be resisted by the shear reinforcement is equal to (398-12) · 6.76 /4.66 = 560 kN.

Next, the shear resistance for diagonal tension cracking is calculated. If this value is higher than the resistance of a member with shear reinforcement, this will be the governing failure mechanism according to the Eurocode and the girder will be considered as a member without shear reinforcement.
In prestressed single span members without shear reinforcement the regions that are not cracked in bending the shear resistance should be limited to the tensile strength of concrete, according to the Eurocode. The Eurocode prescribes that the calculation of the shear resistance is not required for cross-sections that are closer to the support than the point which is the intersection of the elastic centroidal axis and a line inclined from the inner edge of the support at an angle of 45˚. For this specimen with a support plate length of 75 mm, this distance is equal to 75/2 + 402 = 440mm (see Figure 45).
The maximum allowable point load F in Figure 44 is calculated in an iterative way by checking $\sigma_1 \leq f_{ctm}$ for different locations along the length and the height of the beam in the area indicated by the grey zone in Figure 45. For each of these locations, the maximum principal stress σ_1 is calculated with:

$$\sigma_1 = \sqrt{\tau^2 + \left(\frac{\sigma_{cp}}{2}\right)^2} + \frac{\sigma_{cp}}{2}$$

in which

$$\tau = \frac{V_{Rc,calc}\, S}{b_w\, I}$$

and

$$\sigma_{cp} = \frac{N_E}{A} + \frac{M_E z}{I}$$

The tensile strength of the concrete f_{ctm} is equal to 2.12 ln (1 + 87.17/ 10) = 4.69 N/mm^2.

The critical stress state, $\sigma_1 = f_{ctm}$, was found at x = 2.1 m (under the point load) and at the height of the bottom flange – web connection, for a point load of F_m = 592 kN. Table 13 shows the principal stress state in the grey zone in Figure 45 at this critical load.

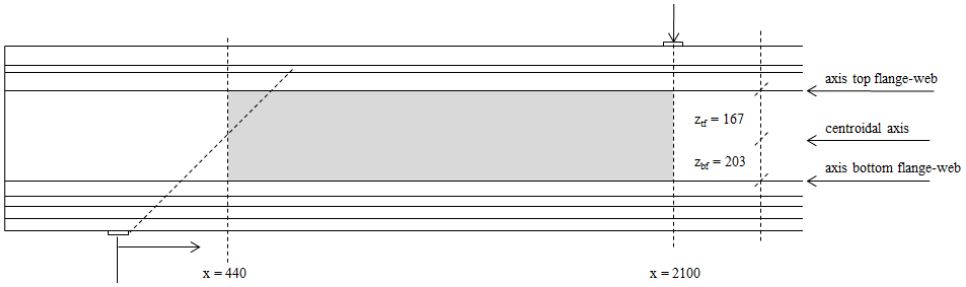

Figure 45: Case PB6. Considered locations (grey zone) for maximum principle tensile stresses.

Table 13: Case PB6. Principle tensile stresses over the height of the beam at different *x* values for *F*m = 592 kN.

		Horizontal position *x* [m]							
		0.44	**0.60**	**0.85**	**1.10**	**1.35**	**1.60**	**1.85**	**2.10**
Vertical position	*top flange-web*	4.23	4.01	3.70	3.43	3.18	2.96	2.76	2.59
	centroidal	3.78	3.77	3.75	3.73	3.71	3.70	3.68	3.66
	bottom flange-web	2.65	2.78	3.00	3.25	3.54	3.87	4.25	4.69

To illustrate the calculation procedure, we consider the critical location at x = 2.1 m and z = 203 mm (bottom flange – web connection) for the point load F_m = 592 kN. The cross-sectional forces due to dead weight at his location are V_{dw} = 3.9 kN and M_{dw} = 18 kNm, the cross-sectional forces due to the prestressing force are V_p = 0 kN and M_p = -467 kNm, and the cross-sectional forces due to the point load are V_F = 408 kN and M_F = 857 kNm. The maximum principal stress σ_1 is then:

$$\sigma_{cp} = \frac{N_E}{A} + \frac{M_E z}{I} = -\frac{1859 \cdot 10^3}{194500} + \frac{(18 + 857 - 467) \cdot 10^6 \cdot 203}{1.50 \cdot 10^{10}} = -4.04 \text{ N/mm}^2$$

$$\tau = \frac{V_{Rc,calc}\, S}{b_w\, I} = \frac{(3.9 + 408) \cdot 10^3 \cdot 2.33 \cdot 10^7}{100 \cdot 1.50 \cdot 10^{10}} = 6.40 \text{ N/mm}^2$$

$$\sigma_1 = \sqrt{\tau^2 + \left(\frac{\sigma_{cp}}{2}\right)^2} + \frac{\sigma_{cp}}{2} = \sqrt{6.40^2 + \left(\frac{-4.04}{2}\right)^2} + \frac{-4.04}{2} = 4.69 \text{ N/mm}^2.$$

The maximum tensile stress at the bottom of the girder at x = 2.1 m for the point load F_m = 592 kN is

$$\sigma_{cp} = \frac{N_E}{A} + \frac{M_E z}{I} = -\frac{1859 \cdot 10^3}{194500} + \frac{(18 + 857 - 467) \cdot 10^6 \cdot 403}{1.50 \cdot 10^{10}} = 1.40 \text{ N/mm}^2$$

Since this stress value is lower than the (flexural) tensile strength of concrete, no flexural cracking prior to shear tension failure is expected. An inverse calculation with σ_{cp} = 4.69 N/mm^2 and F as the free parameter in the equation above, shows that flexural cracking occurs at $F_{m;flex.cr}$ = 677 kN.

Comparing the shear resistance belonging to members with shear reinforcement and the shear resistance for diagonal tension cracking, the maximum value is obtained in case of the latter. Hence, the shear resistance according to the Eurocode, using the mean value of the concrete tensile strength, is determined as F_m = 592 kN. Note that this value is smaller than $F_{m;flex.cr}$, which means that according to these calculations the bottom flange is still uncracked when the occurrence of a diagonal tensile crack is predicted. Note further that the obtained shear resistance value is seen as a lower bound, since the contribution of the stirrups is neglected.

Shear resistance Eurocode/ Model Code level II, based on design values
When the design values are used in the calculation, the shear resistance according to the design provision for members with shear reinforcement is equal to $V_{R,s}$ = 300 kN. With $V_{E,dw}$ = 12 kN at x =0.44, the maximum point load F that can be resisted by the shear reinforcement is equal to (300-12) · 6.76 /4.66 = 418 kN.

When in the calculation of the shear resistance for diagonal tension cracking the principal tensile stress is limited to the design value of the tensile strength f_{ctd} = 0.7 f_{ctm} / 1.5 = 2.19 N/mm², the critical stress state is found at F_d = 359 kN. This critical stress state occurs at x = 0.44 m (the cross-section at the left side of the grey zone) and at the height of the top flange – web connection.

To check this critical stress state, we again calculate σ_1. So, x = 0.44 m and z = -167 mm (top flange – web connection) and the point load F_d = 359 kN. The cross-sectional forces due to dead weight at his location are V_{dw} = 12 kN and M_{dw} = 4.9 kNm, the cross-sectional forces due to the prestressing force are V_p = 0 kN and M_p = -467 kNm, and the cross-sectional forces due to this point load are V_F = 247 kN and M_F = 109 kNm. The maximum principal stress σ_1 is then:

$$\sigma_{cp} = \frac{N_E}{A} + \frac{M_E z}{I} = -\frac{1859 \cdot 10^3}{194500} + \frac{(4.9 + 109 - 467) \cdot 10^6 \cdot -167}{1.50 \cdot 10^{10}} = -5.63 \text{ N/mm}^2$$

$$\tau = \frac{V_{Rc,calc}\, S}{b_w\, I} = \frac{(12 + 247) \cdot 10^3 \cdot 2.39 \cdot 10^7}{100 \cdot 1.50 \cdot 10^{10}} = 4.13 \text{ N/mm}^2$$

$$\sigma_1 = \sqrt{\tau^2 + \left(\frac{\sigma_{cp}}{2}\right)^2} + \frac{\sigma_{cp}}{2} = \sqrt{4.13^2 + \left(\frac{-5.63}{2}\right)^2} + \frac{-5.63}{2} = 2.18 \text{ N/mm}^{2.}$$

Shear resistance Model Code level I, based on mean values
The simpler level I approximation only considers the concrete compressive stress at the centroidal axis due to prestressing. Presumably to account for the simplification, the resistance has to be reduced to 80% of the calculated value. Using the mean value of the concrete tensile strength f_{ctm}, the shear resistance is:

$$V_{Rm,ct} = 0.8\, \frac{I_c\, b_w}{S_c} \sqrt{{f_{ctm}}^2 + \sigma_{cp}\, f_{ctm}}$$

$$V_{Rm,ct} = 0.8\, \frac{1.5 \cdot 10^{10} \cdot 100}{2.53 \cdot 10^7} \sqrt{4.69^2 + 9.56 \cdot 4.69} = 388 \cdot 10^3\ N$$

With $V_{E,dw}$ = 12 kN at x = 0.44 m, the maximum allowable point load F_m in Figure 10 becomes equal to (388 - 12) · 6.76 / 4.66 = 545 kN.

Shear resistance Model Code level I, based on design values
When the principal tensile stress is limited to the design value of the tensile strength f_{ctd} = 0.7 · f_{ctm} / 1.5 = 2.19 N/mm², the design shear resistance $V_{Rd,ct}$ is 241 kN and F_d is 332 kN.

3.3 Finite element model

This section presents all the details of the finite element model for case PB6.

3.3.1 Units

The force unit is in newtons (N) and the length unit in millimeters (mm).

3.3.2 Geometry

Case PB6 is modelled in plane stress conditions. Five different parts in the finite element model can be distinguished: (*i*) the I-shaped beam; (*ii*) the support and loading plates; (*iii*) the interface between the beam and the support and loading plates; (*iv*) the reinforcement; and (*v*) the pre-tensioned strands. The modelling choices for each part are discussed in the following. Note that the damage in the zone at the east side of the beam, tested in the first stage of the experiment, is not considered in the model. Since this damage is located at the right hand side of the right support, it is assumed that neglecting the damage has a minor effect on the structural response.

I-shaped beam: The dimensions of the I-shaped beam are based on Figure 32. To account for the varying out-of-plane thicknesses, the beam geometry is discretized over the height by eight layers, see Figure 46. The calculated thicknesses of the layers are such that the total cross-sectional area of the modelled beam matches with the real cross-sectional area.

Support and loading plates: All plates are modelled with a length of 75 mm and a height of one element (i.e. 50 mm). The out-of-plane thickness of the support plates are set to the thickness of the bottom layer t_1 and the out-of-plane thickness of the loading plate is set to the thickness of the top layer t_8.

Interface: The interfaces between the beam and the support and loading plates are modelled as zero thickness interfaces.

Reinforcement: The reinforcement layout is based on Figure 32. Since some detailed information regarding the positions of the reinforcing bars and stirrups in the beam is missing, the following estimates are made:

- the concrete cover is set to 20 mm (based on $1.5Ø_{strand}$);
- the stirrups in the anchorage zones are distributed over a length of 45 cm;

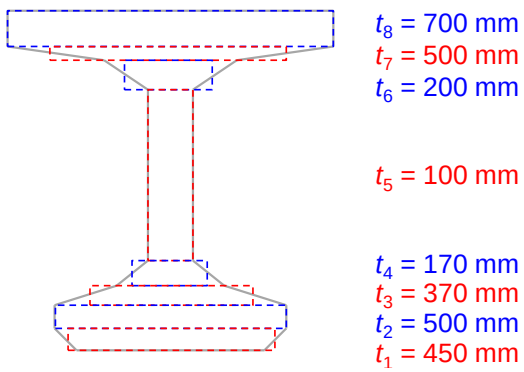

Figure 46: Case PB6. Cross-sectional discretization.

The stirrups in the top and bottom flanges along the beam (except in the anchorage zones) are neglected in the model[4].

Pre-tensioned strands: The sixteen strands are located in four different layers, see Figure 32. To avoid stress concentrations, spurious cracking and subsequent numerical instabilities, each layer of strands is modelled separately.

3.3.3 Material models and parameters

The finite element model has six different materials: (*i*) concrete; (*ii*) structural steel; (*iii*) interface; (*iv*) reinforcing bars; (*v*) stirrups and (*vi*) strands. Table 14 summarizes all the adopted material models and properties, based on Table 12 and the RTD guidelines (Rijkswaterstaat, 2017a).

The concrete material behaviour is modelled with a total strain based orthogonal rotating smeared crack model and a band width estimator according to (Govindjee, 1995). The adopted material properties are as follows: Young's modulus E_c of 43.2 GPa, Poisson's ratio ν of 0.15, density of 2500 kg/m^3, tensile strength f_{ctm} of 4.69 MPa, tensile fracture energy G_f of 0.161 N/mm and compressive strength f_{cm} of 81.17 MPa. The parameters E_c, f_{ctm} and G_f are derived from the formulas of the *fib* Model Code 2010 (CEB/fib, 2012), based on the given f_{cm} from Table 12. The compressive fracture energy G_c is assumed to be equal to 250 G_f, following reference (Nakamura, 2001). The adopted stress-strain tension softening curve is according to (Hordijk, 1991) and for concrete under compression a parabolic softening behaviour is assumed, see Figure 47. Furthermore, lateral effects of cracking (Vecchio, 1993) and confinement (Selby, 1993) on the compressive strength and a variable Poisson's ratio dependent on the crack width are included.

The material behaviour of the steel plates is modelled with a linear-elastic stress-strain relation, using the elastic properties E_s of 210 GPa and ν of 0.3. Furthermore, the density of the steel is set to 7850 kg/m^3.

The interface between the steel plates and concrete have elastic stiffness properties of $k_n = 4.32 \cdot 10^4$ N/mm^3 and $k_t = 4.32 \cdot 10^1$ N/mm^3, which are derived from the Young's modulus of the concrete. A bilinear behaviour is assumed in the interface normal direction and a linear-elastic behaviour in the interface tangential direction. The normal stiffness in tension and compression are set to $4.32 \cdot 10^1$ N/mm^3 and $4.32 \cdot 10^4$ N/mm^3 respectively, simulating a no-tension interface (see Figure 48).

[4] Since the stirrups in the bottom flange consist of two parts (see Figure 32) and their height is limited, it is questionable if they are effective from a mechanical point of view. When included in the model, the stirrups most likely do have an (small) effect on the crack development and subsequently they may affect the failure behaviour.

Table 14: Case PB6. Summary of the adopted material models and properties in the FE model.

Material/-model	*Variable/parameter*	*Value*
Concrete	Density	2500 kg/m^3
total strain based smeared rotating crack model	Young's modulus*	43.21 GPa
	Poisson's ratio ν	0.15
	Variable Poisson's ratio	Yes
	Compression curve	Parabolic
	Compressive strength	81.17 MPa
	Compressive fracture energy	40.27 N/mm
	Reduction due to lateral cracking	Yes
	Minimum reduction factor f_{cm}	0.4
	Influence of lateral confinement	Yes
	Tensile strength*	4.69 MPa
	Type of tension softening	Hordijk
	Tensile fracture energy*	0.161 N/mm
	Band width estimator	Govindjee
	Maximum aggregate size	12 mm
Stirrups	Young's modulus	200 GPa
hardening plasticity	Yield strength at ε_y = 0.25%	525.38 MPa
	Ultimate strength at ε_u = 27%	660.63 MPa
Longitudinal bars Ø8	Young's modulus	200 GPa
hardening plasticity	Yield strength at ε_y = 0.27%	556.5 MPa
	Ultimate strength at ε_u = 25%	664.0 MPa
Longitudinal bars Ø10	Young's modulus	200 GPa
hardening plasticity	Yield strength at ε_y = 0.28%	581.0 MPa
	Ultimate strength at ε_u = 24%	691 MPa
Strands	Young's modulus	192.94 GPa
hardening plasticity	Yield strength at ε_y = 0.92%	1776 MPa
	Ultimate strength at ε_u = 5.17%	1941.4 MPa
Bond	Perfect bond	
Interface steel plates	Normal stiffness	4.32·10^4 N/mm^3
Nonlinear-elasticity	Shear stiffness	4.32·10^1 N/mm^3
	No-tension interface (Δ - σ_n curve)	Yes
Structural steel	Density	7850 kg/m^3
linear-elastic	Elastic modulus	210 GPa
	Poisson's ratio	0.3

* Derived from relation given in *fib* Model Code 2010 (CEB/fib, 2012).

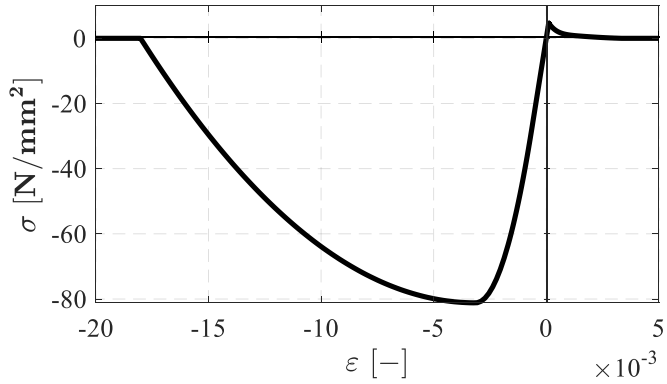

Figure 47: Case PB6. Adopted stress-strain curve for concrete (based on a crack band width of 50 mm).

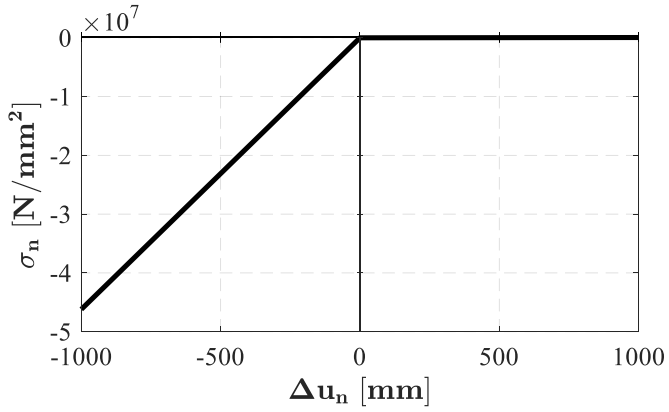

Figure 48: Case PB6. Adopted traction-displacement curve in the interface normal direction.

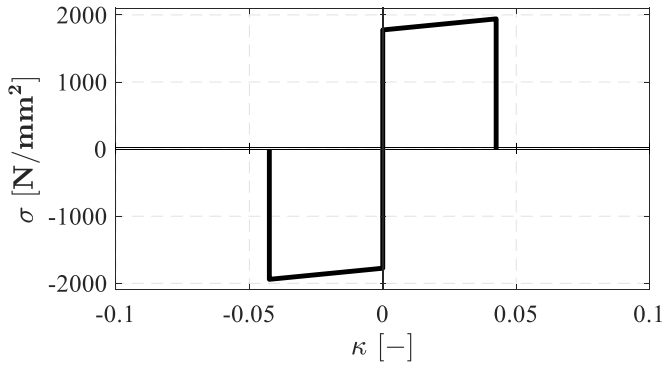

Figure 49: Case PB6. Adopted stress - equivalent plastic strain curve for the strands.

The reinforcing bars, stirrups and strands adopt von Mises plasticity and hardening behaviour. Figure 49 shows the stress – equivalent plastic strain curve for the strands. Similar curves are applied to the reinforcing bars and stirrups, though with different values. The elastic modulus E_s, the yield strength f_{ym}, the ultimate strength f_{tm} and the ultimate (total) strain[5] ε_u for the different reinforcements are obtained from Table 12. The elastic modulus of the reinforcing bars and stirrups is set to 200 GPa. The interaction between the reinforcements and concrete is modelled with perfect bond.

3.3.4 Element types and finite element mesh

Figure 50 shows the 2D finite element model that is used to simulate the test. The finite element model adopts three different element types: (*i*) plane stress elements; (*ii*) interface elements; and (*iii*) embedded reinforcements.

The concrete is represented by a structured mesh, consisting of quadrilateral plane stress elements based on quadratic interpolation and using a 3 x 3 (full) Gauss integration scheme. The averaged elements sizes are set to 50 mm by 50 mm. The out-of-plane thicknesses of these elements are based on Figure 12. The steel plates, that introduce the load and support forces, are modelled by the same elements.

[5] The ultimate strain values from Table 12, based on test specimens with length of 100 mm, are used in the model. Since the element size is approximately 50 mm (see section 3.3.4), the numerically obtained strain values may be larger than the specified ultimate strain values to cause rupture of the bar.

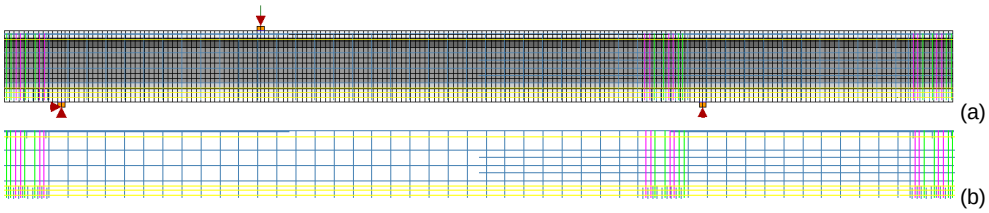

Figure 50: Case PB6. Mesh and boundary conditions (a) and embedded reinforcement sets (b).

Zero-thickness quadratic interface elements with a 3-point Newton-Cotes integration scheme are used between the steel plates and the concrete beam.

The reinforcing bars, stirrups and strands are modelled by embedded reinforcement elements with 2-point Gauss integration, assuming perfect bond between the steel and concrete. The reinforcements only have axial stiffness.

3.3.5 *Boundary conditions and loading*

Horizontal and vertical constraints are applied at the bottom mid-nodes of the support plates. According to Figure 35, the left support is constrained in *x* and *y* direction and the right support in only the *y* direction. Furthermore, a vertical constraint is attached to the top mid-node of the loading plate in order to apply the unit displacement.

Three loads are considered in the simulation of the test: prestressing, dead weight and a unit displacement of 1 mm at the loading plate. The loads are applied in three separate load cases.

The prestressing load is divided over four layers of strands, which are simultaneously applied. The forces P_i per layer of strands is calculated with:

$$P_i = \sigma_{pcs} \cdot A_{p;i} \tag{6}$$

where σ_{pcs} is the stress in the prestressed strands at time of testing and $A_{p;I}$ the area of strands in layer *i*, *i* = 1…4. The stress σ_{pcs} is calculated from the averaged stress in the concrete after prestressing losses σ_{cp} = 9.56 N/mm^2, see subsection 3.1.1, using:

$$\sigma_{pcs} = \frac{\sigma_{cp} \cdot A_c}{A_p} = \frac{9.56 \cdot 194500}{1584} = 1173.9 \ \text{N/mm}^2 \tag{7}$$

Due to elastic shortening a lower stress level in the strands will occur. Therefore, the strands are “overstressed” in the model in order to get the intended stress level in the strands. The required input value for σ_{pcs} is calculated from results of a linear-elastic calculation, such that σ_{cp} at the neutral line is approximately 9.56 N/mm^2.

The prestressing forces are gradually introduced (i.e. from zero to P_i) over a transmission length l_{pt}, which is calculated from the equations in section 8.10.2.2 of (CEN, 2011):

$$l_{pt} = \alpha_1 \alpha_2 \phi \frac{\sigma_{p0}}{f_{bpt}} \tag{8}$$

where:

$\alpha_1 = 1.25$ (for sudden release – as a conservative approach)

$\alpha_2 = 0.19$ (for three- and seven-wire strands)

$\phi = 12.7$ mm

$\sigma_{p0} = 1397$ N/mm^2

$f_{ctm} = 4.27$ N/mm^2 (based on f_{cm} = 65 N/mm^2, see subsection 3.1.2)

$$f_{ctm}(t) = \beta_{cc}(t) \cdot f_{ctm} = \exp\left(0.25 \cdot \left(1 - \left(28/6\right)^{0.5}\right)\right) \cdot 4.27 = 3.20 \text{ N/mm}^2$$

$$f_{bpt} = \eta_{p1} \cdot \eta_1 \cdot \alpha_{ct} \cdot 0.7 \cdot \frac{f_{ctm}(t)}{\gamma_c} = 3.2 \cdot 1.0 \cdot 1.0 \cdot 0.7 \cdot \frac{3.20}{1.0} = 7.16 \text{ N/mm}^2$$

(for the simulation of the test, the partial factor is set to 1.0)

As mentioned in subsection 3.1.1, the prestressing was applied six days after casting. Hence, the transmission length belonging to t = 6 is equal to 589 mm.

3.3.6 Load increments and convergence criteria

The analysis is performed in two phases. In the first phase, the loads “prestressing” and “dead weight“ are subsequently applied, both in one step. The second phase of the analysis is performed in displacement control with 25 steps of 0.20 mm, 60 steps of 0.01 mm, 50 steps of 0.20 mm and 150 steps of 0.025 mm. The regular Newton-Raphson method is used as solution procedure, with maximal 50 iterations per load step. An explicit line search technique is adopted in order to decrease the number of iterations per increment. A force tolerance of 1.0% and an energy tolerance of 0.1% are used as convergence criteria. The analysis is set to continue, even if the convergence criteria are not satisfied.

3.4 Nonlinear finite element analysis

This section presents the results of the analysis of case PB6. Attention is given to the load – deflection response, the convergence behaviour, the deformed meshes, the crack widths in concrete, the strains in steel, and Gauss point statistics.

3.4.1 Load – deflection

Figure 51 presents the load – deflection response of the beam during phase 2 of the analysis (black line), where the deflections are measured at the loading point. Seven steps are marked with red dots, indicating different events in the failure process. These points are closer investigated in the following paragraphs. Non-converged steps are indicated with blue circles. The numerically obtained load bearing capacity of the beam is 962 kN, which is visible at the fifth point.

The load – deflection response starts with negative deflections, indicating the upward bending due to the prestress (phase 1). In the second phase of the analysis, the displacement at the loading plate is applied that causes a downward (positive) deflection of the beam. Until a load of 670 kN (point 1, load step 58) the beam behaves almost linearly. After this point, the load drops to 602 kN. This load drop is accompanied with the formation of diagonal cracks in the web between the left support and the loading plate and the yielding of two stirrups that are intersected by these cracks (point 2, load step 60). None of the load steps 59 to 62 during this load drop reaches convergence. Subsequently, the system regains its equilibrium

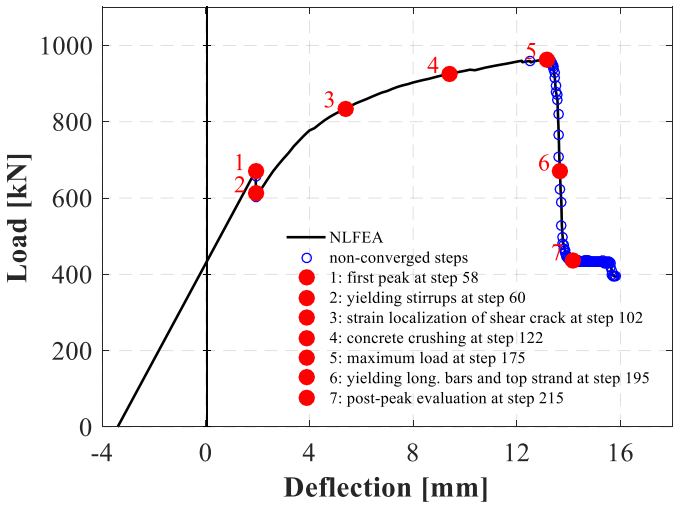

Figure 51: Case PB6. Load – deflection curve during phase 2 of the analysis.

state and the analysis continued till load step 180 with only one non-converged step. During this stage of the analysis, the following is observed:

- the number of stirrups that starts to yield increases from two to nine;
- the steepness of the slope of the load – deflection response decreases just before point 3 (at a load of 835 kN, load step 102). This change in the global stiffness of the beam corresponds with the moment that (*i*) the strains in the web further localize into a distinct diagonal crack; and (*ii*) the bottom flange gets flexural cracks;
- the concrete at the top of the web, close to the loading plate, starts to crush at a load of 925 kN (point 4, load step 122);
- the beam reaches its maximum capacity of 962 kN (point 5, load step 175).

Note that the presence of the stirrups in the beam and the hardening behaviour of the steel in the stirrups are important reasons why the beam is able to redistribute stresses and carry more load after point 2. Soon after the maximum load is reached, the beam fails. The results at the points 6 (at a load of 669 kN, load step 195) and 7 (at a load of 435 kN, load step 215) indicate that this failure is accompanied with crushing of the concrete in the web and the top flange shearing off. However, these results should be treated with caution, since after load step 180 most of the remaining load steps do not reach convergence anymore and so they belong to an unreliable equilibrium path.

3.4.2 Convergence behaviour

Figure 52 shows the evolution of the relative out of balance force and relative energy variation during the analysis. The red dots refer to the points in the load – deflection curve, see Figure 51. The black lines in the two graphs indicate the force norm and energy norm respectively.

Until point 1, phase 2 of the analysis converges on the basis of the force norm. The energy norm is not considered in this stage, since the load steps converge without iterations. In the following five load steps both the force norm criterion and energy norm criterion are not satisfied. Next, till load step 180 the convergence is reached on the basis of the energy norm. Beyond this step, almost all steps are non-converged, except some steps at the end of the analysis.

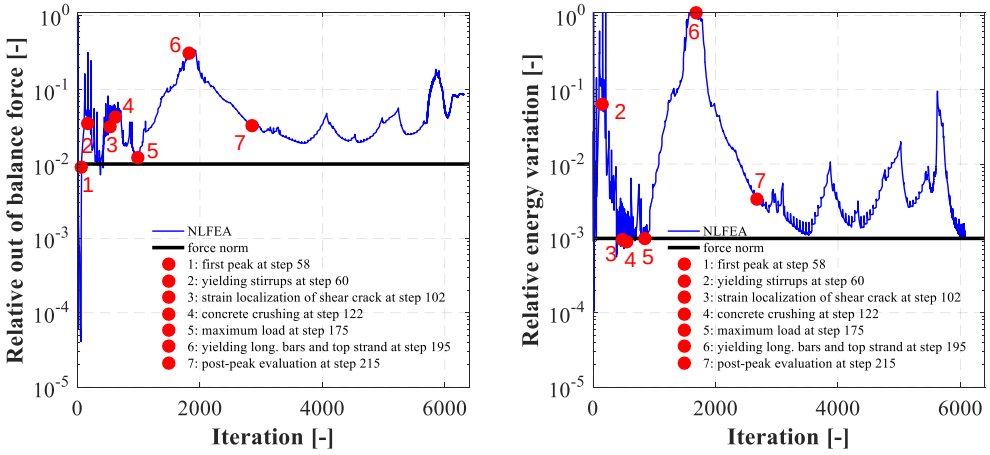

Figure 52: Case PB6. Evolutions of the relative out of balance force and relative energy variation.

3.4.3 *Deformed meshes*

Figure 53 presents the meshes with normalized deformations at the load steps 58, 60, 102, 122, 175, 195 and 215. The plots show that the main deformations happen in the web of the beam between the left support and the loading plate. Local element distortions become gradually more pronounced, especially at the top of the web near the loading plate. The plots of the last two considered load steps reveal elements for which the element stiffness is entirely vanished. Though these load steps belong to an unreliable equilibrium path, they suggest that failure mode can be characterized by crushing of the concrete in the web and that the top flange shearing off.

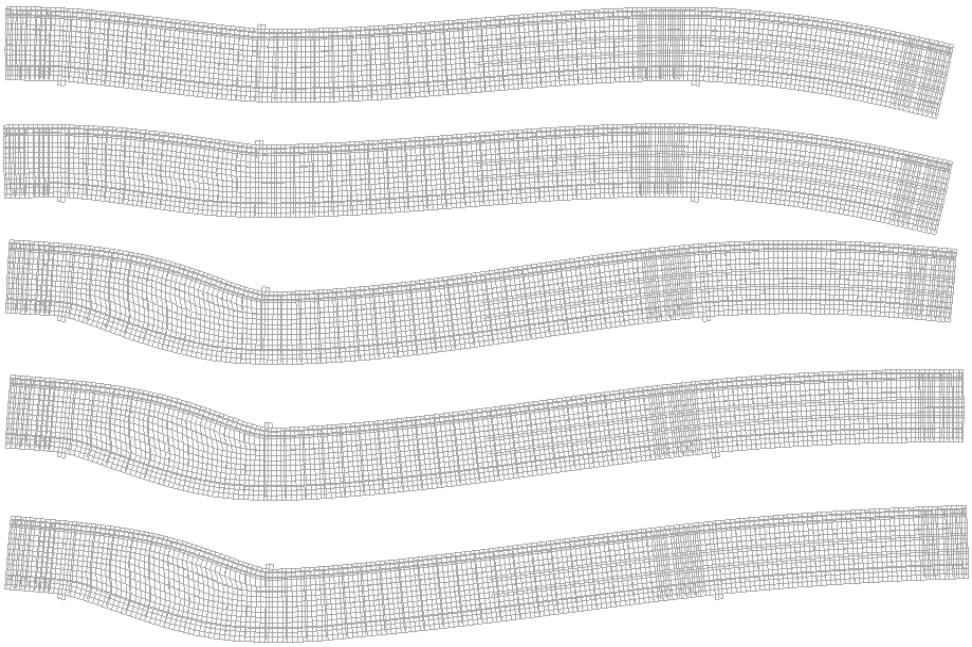

Continued at the next page

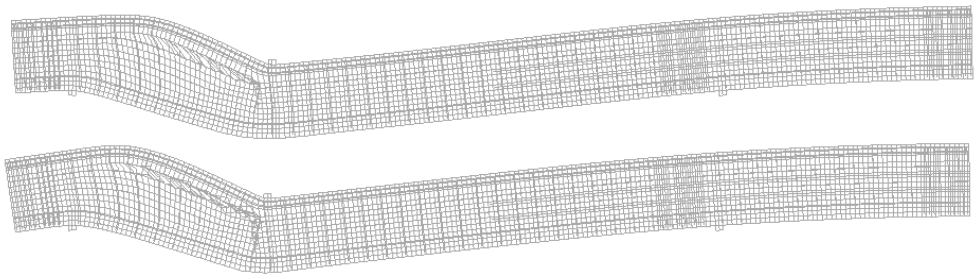

Figure 53: Case PB6. Deformed meshes at the load steps 58, 60, 102, 122, 175, 195 and 215, see Figure 51.

3.4.4 *Crack widths and principal strains in concrete*

Figure 54 presents the crack widths plots at the load steps 58, 60, 102, 122, 175, 195 and 215. Figure 55 and Figure 56 present the plots with the maximum principal strains (ε_1) and minimal principal strains (ε_2) at these load steps respectively. The plots reveal the evolution of the fracture process in different stages. Before point 3 (load step 102), only the web is cracked, which leads to an active contribution of some stirrups to the resistance of the beam. At point 3, flexural cracks appear in the bottom flange under the loading plate and a distinct diagonal crack in the web becomes visible. In the subsequent points, the flexural cracks and the cracks in the shear zone further develops. Large crack widths are especially found at the top of the web. At point 4 (load step 122), the concrete in the web near the loading plate starts to crush. This crushing zone increases when the deflections increases, first by horizontally propagating along the top flange and later (at the load steps 195 and 215, after failure) also by vertically propagating in the web of the beam. It is observed that the top flange of the beam did not crush, though the compressive stresses here are higher than at the top of the web. Checks on the principal stresses reveal that there exists a biaxial compression state under the loading plate. In such a stress state the compressive strength increases according to (Selby, 1993), see subsection 3.3.3, and hence the crushing is postponed.
Note that the results of the last two load steps belong to an unreliable equilibrium path.

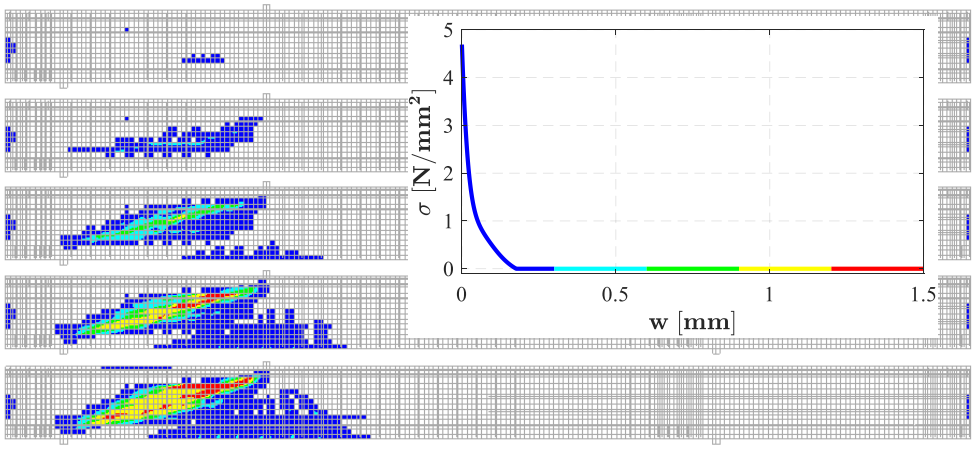

Continued at the next page

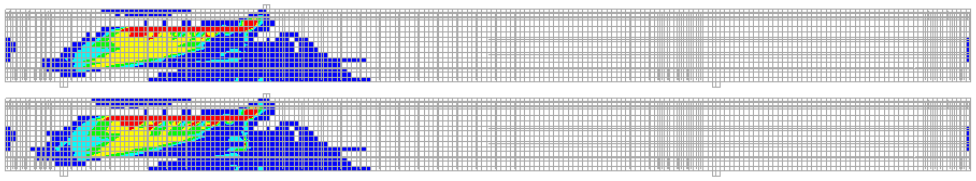

Figure 54: Case PB6. Crack width plots at the load steps 58, 60, 102, 122, 175, 195 and 215, see Figure 51.

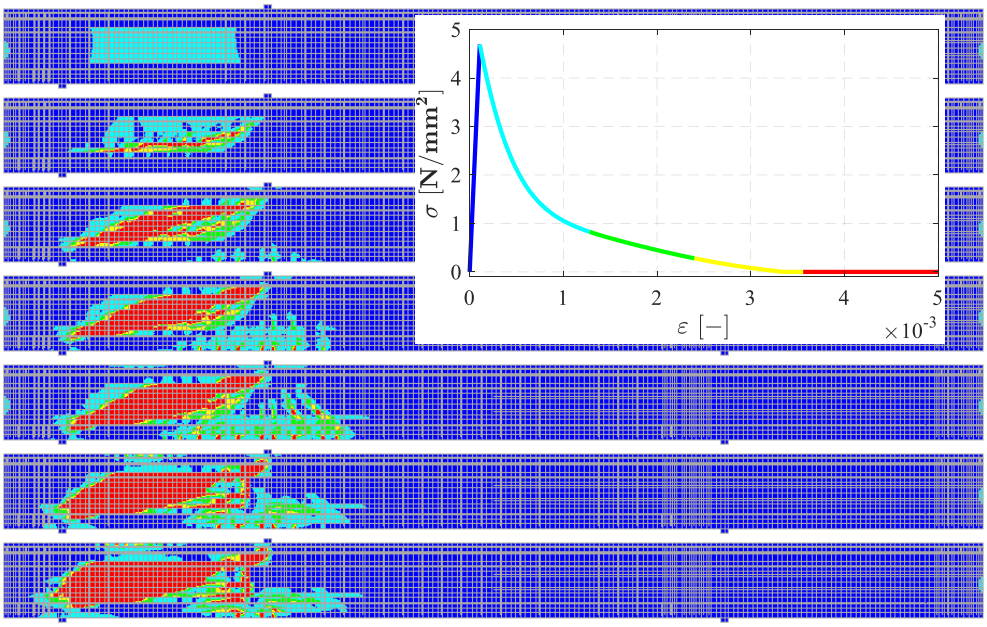

Figure 55: Case PB6. Maximum principal strain plots (ε_1) at the load steps 58, 60, 102, 122, 175, 195 and 215, see Figure 51.

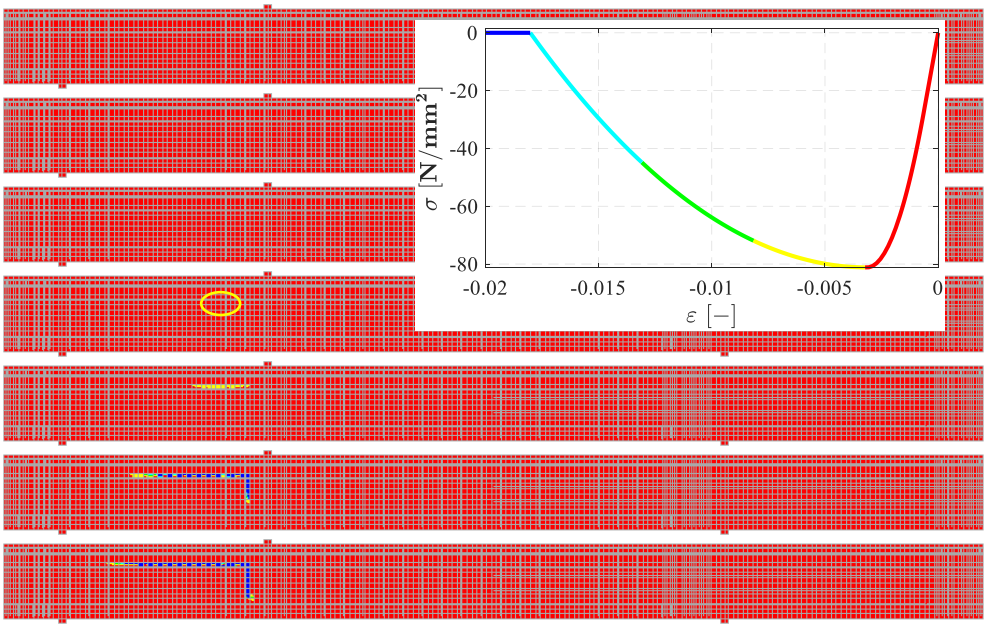

Figure 56: Case PB6. Minimum principal strain plots (ε_2) at the load steps 58, 60, 102, 122, 175, 195 and 215, see Figure 51.

3.4.5 *Strains in steel*

Figure 57 presents the strains in the stirrups and reinforcing bars at the load steps 58, 60, 102, 122, 175, 195 and 215. The colour legend scale is related to the stress –equivalent plastic strain curve for the stirrups. The first two stirrups start to yield at point 2 (load step 60). In the ascending branch of the load – deflection response, after the small load drop, the number of yielding stirrups increases to nine at point 4 (load step 122). The reinforcing bars and the strands did not yield during the converged part of the analysis. The elastic limit in these reinforcements is locally exceeded in the post-peak regime, which belong to an unreliable equilibrium path. Note that the strain values in the stirrups, reinforcing bars and strands remain far from the ultimate strain values, during the analysis.

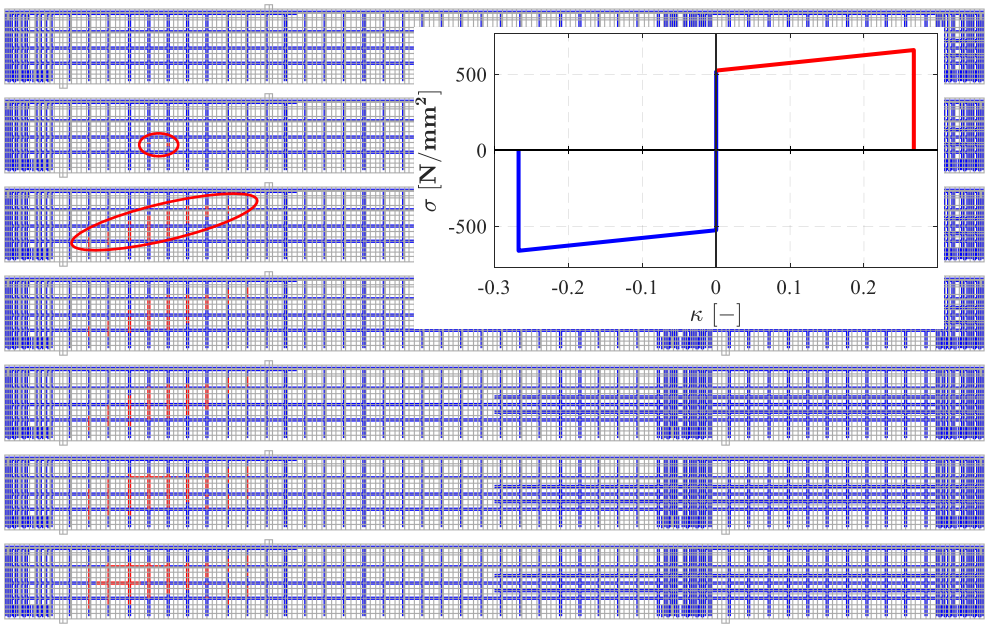

Figure 57: Case PB6. Strains in stirrups and reinforcing bars at the load steps 58, 60, 102, 122, 175, 195 and 215, see Figure 51.

3.4.6 *Gauss point statistics*

Figure 58 presents the evolutions of the number of Gauss points with earlier and present plastic behaviour (crushing or yielding) and the number of cracked Gauss points. The graphs highlight the events, as described before.

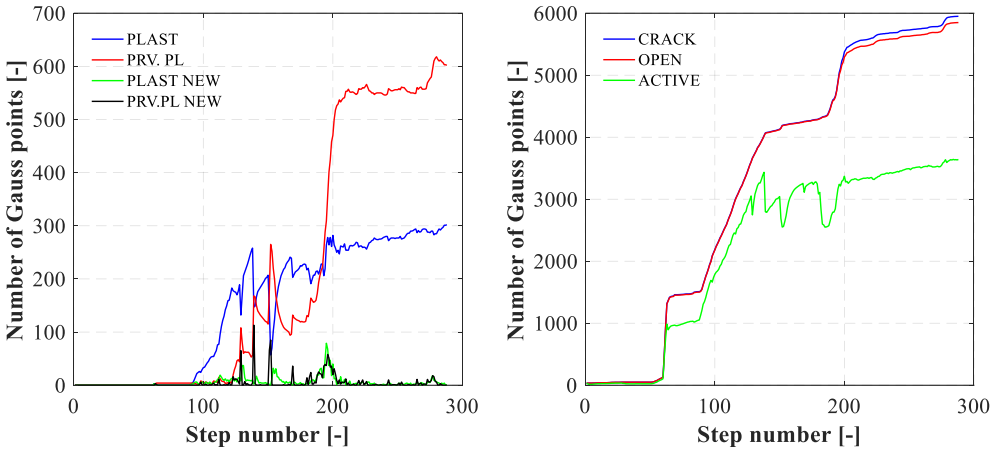

Figure 58: Case PB6. Evolutions of the number of Gauss points with (former) plastic behaviour (crushing or yielding) and the number of cracked Gauss points.

3.5 Application of safety formats for nonlinear finite element analysis

This section demonstrates the application of the three safety formats *global resistance factor method* (GRF), *estimation of the coefficient of variation of the resistance* (E-COV) and the *partial factor method* (PF), as proposed in *fib* Model Code 2010 (CEB/fib, 2012). In total, four different nonlinear finite element analyses need to be performed.

Table 15 to Table 19 summarize the input geometry and material parameters of the concrete, reinforcing bars and strands for the four analyses. The input parameters are based on the mean values, characteristic values, mean GRF values and design values, which are calculated according to Annex A of (Rijkswaterstaat, 2017a). According to this annex, only material properties are changed and the geometry properties are kept constant.

Table 15: Case PB6. Concrete properties for the nonlinear analyses of the safety formats.

	f_c (N/mm²)	f_{ct} (N/mm²)	E_c (N/mm²)	ν (-)	G_f [6] (N/mm)	G_c (N/mm)
Mean	81.17	4.69	43209	var	0.1611	40.26
Characteristic	73.17	3.28	41740	var	0.1581	39.52
Mean GRF	62.19	4.19	39539	var	0.1535	38.38
Design	48.78	2.19	36463	var	0.1470	36.74

Table 16: Case PB6. Stirrup properties for the nonlinear analyses of the safety formats.

	Ø (mm)	A_s (mm²)	f_y (N/mm²)	f_t (N/mm²)	E_s (N/mm²)	ε_{sy} (-)
Mean	8.0	50.27	525.38	660.63	200000	0.0026
Characteristic	8.0	50.27	475.86	598.36	200000	0.0024
Mean GRF	8.0	50.27	523.45	658.20	200000	0.0026
Design	8.0	50.27	413.79	520.31	200000	0.0021

[6] Note that the variations in the fracture energies G_f and G_c are surprisingly small and their values do not proportionally change with the values of the tensile strength f_t and compressive strength f_c.

Table 17: Case PB6. Properties of the longitudinal reinforcing bars Ø8 for the nonlinear analyses of the safety formats.

	Ø (mm)	A_s (mm²)	f_y (N/mm²)	f_t (N/mm²)	E_s (N/mm²)	ε_{sy} (-)
Mean	8.0	50.27	556.50	664.00	200000	0.0028
Characteristic	8.0	50.27	504.04	601.41	200000	0.0025
Mean GRF	8.0	50.27	554.45	661.55	200000	0.0028
Design	8.0	50.27	438.30	522.97	200000	0.0022

Table 18: Case PB6. Properties of the longitudinal reinforcing bars Ø10 for the nonlinear analyses of the safety formats.

	Ø (mm)	A_s (mm²)	f_y (N/mm²)	f_t (N/mm²)	E_s (N/mm²)	ε_{sy} (-)
Mean	10.0	78.54	581.00	691.00	200000	0.0029
Characteristic	10.0	78.54	526.24	625.87	200000	0.0026
Mean GRF	10.0	78.54	578.86	688.46	200000	0.0029
Design	10.0	78.54	457.60	544.23	200000	0.0023

Table 19: Case PB6. Strand properties for the nonlinear analyses of the safety formats.

	Ø (mm)	A_s (mm²)	f_y (N/mm²)	f_t (N/mm²)	E_s (N/mm²)	ε_{sy} (-)
Mean	12.7	99	1776.0	1941.4	192940	0.0092
Characteristic	12.7	99	1608.6	1758.4	192940	0.0083
Mean GRF	12.7	99	1769.5	1934.2	192940	0.0092
Design	12.7	99	1398.8	1529.1	192940	0.0072

The load increment scheme is determined per analysis and slightly differs from the one discussed in subsection 3.2.6.

Figure 59 presents the load – deflection curves of the analyses with mean values, characteristic values, mean GRF values and design values for the input parameters of the concrete, reinforcing bars and strands. Their corresponding first peak load values are 670 kN, 531 kN, 624 kN and 434 kN respectively. Their corresponding maximum load capacities are 962 kN, 905 kN, 865 kN and 727 kN respectively, which reveals a strong correlation with the concrete compressive strength. The analyses with characteristic values, mean GRF values and design values reveal a similar failure behaviour as the analysis with mean values. Using the expressions provided by Annex A of (Rijkswaterstaat, 2017a), the design resistances for the safety formats can be calculated. The design values related to the *first peak load* are compared in Figure 60 and Table 20, together with the results of the analytical calculations from subsection 3.2.4. The resistances based on mean values of the input parameters are also added. The design values related to the *maximum load* are compared in Figure 61 and Table 21, together with the results of the analytical calculations from subsection 3.2.4. Note that the analysis with label “No safety format” refers to the analysis with mean values, discussed in the previous section.

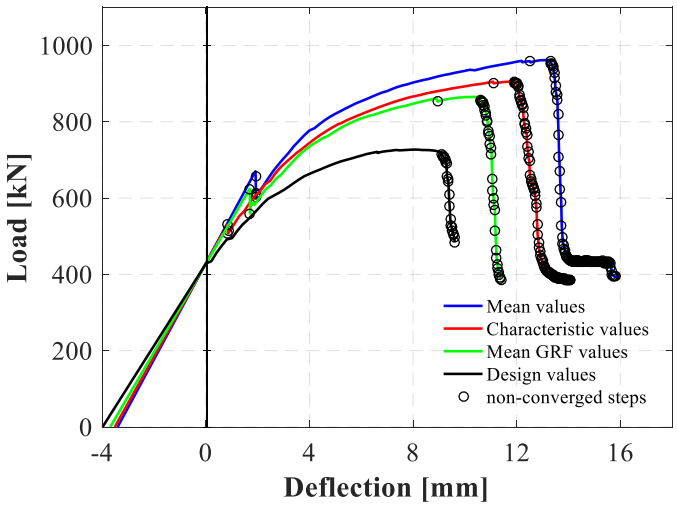

Figure 59: Case PB6. Load – deflection curves of the analyses with mean values, characteristic values, mean GRF values and design values for the input parameters of the concrete, reinforcing bars and strands.

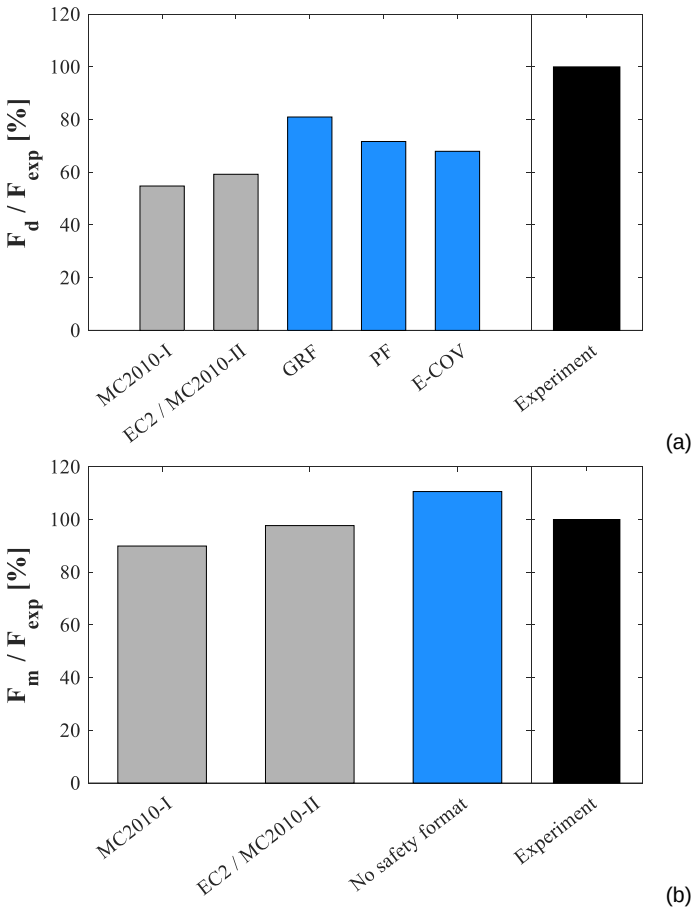

Figure 60: Case PB6. Design values of the resistance (F_d) according to the different safety formats (a) and the resistances (F_m) based on the mean values of the input parameters (b), expressed in terms of a percentage of the experimentally obtained ultimate load (F_{exp}). All values are related to the *first peak load*. The grey colour bars refer to the calculations with symbolic expressions, the blue colour bars to the nonlinear finite element analyses.

Table 20: Case PB6. Design values of the resistance according to the different safety formats and the resistances (F_m) based on the mean values of the input parameters (in kN). All values are related to the *first peak load*.

	Design values (F_d)					**Mean input (F_m)**		
F_{exp}	*MC2010 level I*	*EC2 / MC2010 level II*	*GRF*	*PF*	*E-COV*	*MC2010 level I*	*EC2 / MC2010 level II*	*No safety formats*
606	332	359	491	434	412	545	592	670

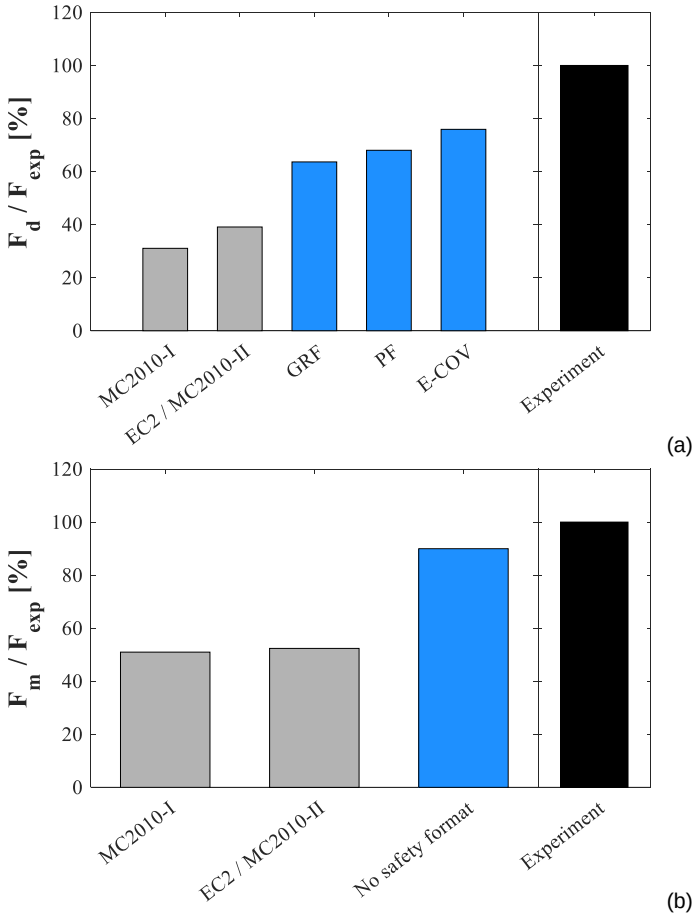

Figure 61: Case PB6. Design values of the resistance (F_d) according to the different safety formats (a) and the resistances (F_m) based on the mean values of the input parameters (b), expressed in terms of a percentage of the experimentally obtained ultimate load (F_{exp}). All values are related to the *maximum load*. The grey colour bars refer to the calculations with symbolic expressions, the blue colour bars to the nonlinear finite element analyses.

Table 21: Case PB6. Design values of the resistance according to the different safety formats and the resistances (F_m) based on the mean values of the input parameters (in kN). All values are related to the *maximum load*.

	Design values (F_d)					**Mean input (F_m)**		
F_{exp}	*MC2010 level I*	*EC2 / MC2010 level II**	*GRF*	*PF*	*E-COV*	*MC2010 level I*	*EC2 / MC2010 level II**	*No safety formats*
1069	332	418	680	727	812	545	560	962

* Corresponding to $V_{R,s}$ in subsection 3.2.4.

3.6 Sensitivity analysis

This section investigates the sensitivity of the numerical results of the previous analysis with mean values with respect to the (*i*) crack model; (*ii*) the level of prestressing force; (*iii*) the geometrical representation / element type, and (*iv*) the tensile strength of the concrete. The variations are explained in the following. For each analysis, a new load increment scheme is determined. These schemes slightly differ from the one discussed in subsection 3.2.6.

Crack model: In this analysis the rotating crack model is replaced by a fixed crack model. All the other modelling aspects are the same as described in section 3.3. The fixed crack model requires the specification of a shear retention relation. In this study, the damaged based shear retention relation and the aggregate size based shear retention relation are considered. In the former relation, the shear retention *G* depends on the normal stiffness decay (and so on the crack normal strain), via:

$$G = \frac{E_n}{2(1+\nu)} \tag{9}$$

In the latter relation, the shear retention factor β depends on the aggregate size d_{aggr}, the crack normal strain ε_n and the crack band width *h*, via:

$$\beta = 1 - \left(\frac{2}{d_{aggr}} \right) \cdot \varepsilon_n \cdot h \tag{10}$$

The damaged based shear retention relation is characterized by a relatively rapidly decreasing shear stiffness and the aggregate size based shear retention relation is characterized by a relatively slow decreasing shear stiffness.

Level of prestressing force: In this analysis the prestressing force *P* is increased by 10%. All the other modelling aspects are the same as described in section 3.3. In the context of ULS verification, the level of *P* is less importance in case of problems with bending failure. However, in case of problems with shear failure the level of *P* can be quite important, since it will determine the (bending) crack development and the principal stress distribution in the structure.

Geometrical representation / element type: In this analysis the beam is modelled by shell elements with quadratic interpolation. The model has a T-shape in cross-sectional view, meaning that the top flange is modelled by “out-of-plane” shell elements and the web and bottom flange are modelled by “in-plane” shell elements. Figure 62 shows the thickness directions and their thicknesses in the adopted cross- sectional discretization. The shell elements are modelled in the center lines of the flanges and web, except in top flange – web connection. Hence, the cross-sectional area and moment of inertia in the model differ from the real cross-sectional area and moment of inertia. All the other modelling aspects of this shell element model are the same as described in section 3.3. Figure 63 shows the mesh of the shell element model.

Note that the adopted cross-sectional discretization in the shell element model is only one of the possibilities. Other cross-sectional discretization’s may be equally valid. Though there is some overlapping material in the top flange – web connection, this model is considered as a conservative approach, because: (*i*) the

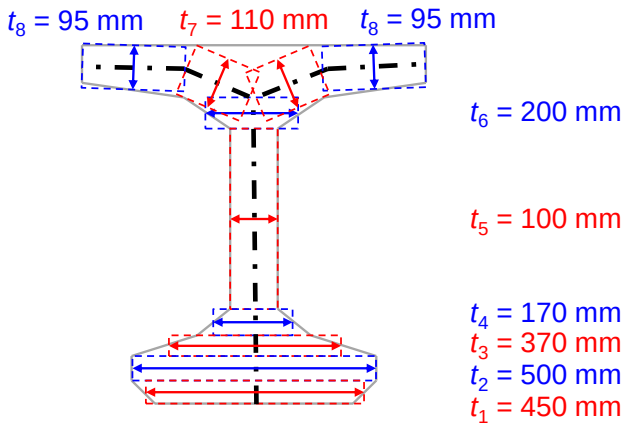

Figure 62: Case PB6. Cross-sectional discretization for the shell model.

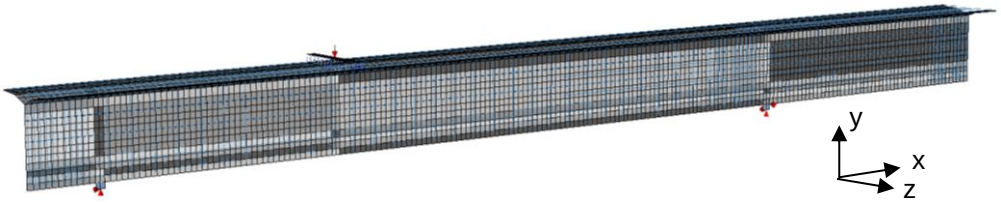

Figure 63: Case PB6. Mesh of the shell element model.

moment of inertia and *y* coordinate of the center of gravity are lower compared to the real beam; (*ii*) some material in the parts with thickness t_7 is neglected.

Tensile strength of the concrete: In this analysis the mean value of the concrete tensile strength is reduced by 32.8%, leading to $f_t = 0.672\ f_{t;m}$. All the other modelling aspects are the same as described in section 3.3.

Figure 64 presents the load – deflection responses of the sensitivity analyses. The values of the loads belonging to the first peak and the maximum observed values are summarized in Table 22. From the comparison with the results of the reference analysis in section 3.4, it can be noted that the adopted crack model does not influence the response till the first peak, but strongly affects the response after this first peak. This second part of the structural response, in turn, significantly depends on the shear retention relation in the fixed crack model. The analysis with the aggregate size based shear retention relation reveals a 250 kN higher resistance and a much more ductile behaviour, compared to the analysis with the damaged based shear retention relation. These significant differences in the failure behaviour of the beam indicate that the formulation of the shear stiffness degradation matters for this beam with a heavily cracked shear zone.

The level of prestress slightly affects the results. An increase of 10% in the prestressing force leads to an increase of 3.9% in the first peak load value and an increase of 3.3% in the load capacity.

Using shell elements instead of plane stress elements have also limited effects on the results. The shell element model results in a 3.7% lower first peak load value and a 2.5% lower load capacity. The lower first peak load value can be explained by

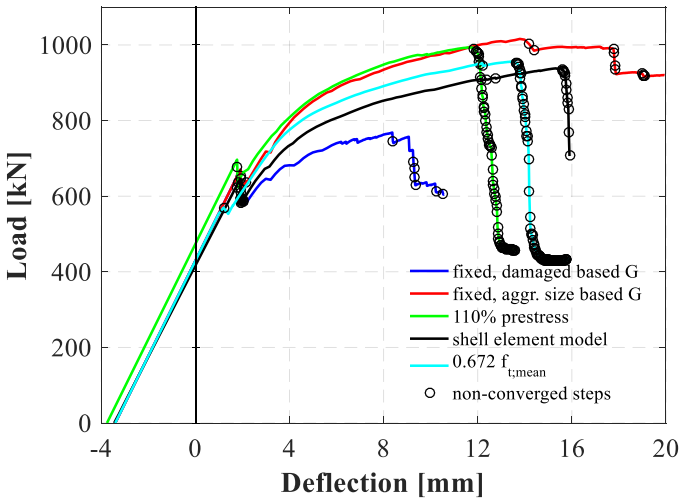

Figure 64: Case PB6. Load – deflection curves of the sensitivity analyses.

Table 22: Case PB6. First peak load values and the maximum load capacities of sensitivity analyses.

Analysis	1st peak load (kN)	Max. load capacity (kN)
Reference analysis (“No safety format”, mean values)	670.3	961.9
Fixed crack model – damaged based shear retention	670.3	768.4
Fixed crack model – aggr. size based shear retention	670.3	1016.0
10% higher prestressing force	696.7	993.4
Shell element model	645.6	938.1
Reduced tensile strength of the concrete	569.8	956.0

the adopted cross-sectional discretization, which leads to a lower moment of inertia and a lower *y* coordinate of the center of gravity compared to the real beam. As a result of that, the bending stiffness and the eccentricity of the prestressing force to the centroidal axis of the beam (i.e. the bending moment due to prestressing force) are decreased. The lower load capacity can be attributed to the fact that due to the adopted cross-sectional discretization less material is present in the compression zone of the top flange compared to the real beam.
The adopted value of the tensile strength of the concrete only affects the first peak load value. A reduction of 32.8% in the tensile strength results in a reduction of 15% of this first peak load value. The maximum load capacity is hardly affected by the tensile strength. This is not surprising, since the failure mode is dominated by the material behaviour of the reinforcement and the behaviour of the concrete under compression.

3.7 Concluding remarks

The failure mechanism and the sequence of events are well simulated by the numerical analyses. Table 23 compares the numerically and experimentally obtained loads for different events. Mean values of the material properties have been used in the numerical analysis. The maximum observed load value is considered as the ultimate load capacity.

Table 23: Case PB6. Comparison between numerical results and experimental results (mean values).

	f_{ctm} (MPa)	NLFEA (kN)	Experiment (kN)
Load first crack	4.69	670	606
	3.15	570	
After first peak load	4.69	602	584 (considered as not reliable)
Maximum load	4.69	962	1069 (considered as ultimate capacity)
	3.15	956	

Considering a mean concrete tensile strength according to (CEB/fib, 2012), the numerical analysis overestimates the load at the first diagonal crack by 11%. The numerical analysis underestimates the ultimate load capacity by 10%.

Considering a reduced concrete tensile strength of 3.15 MPa, the numerical analysis underestimates the load at the first diagonal crack by 6%. The influence of the concrete tensile strength on the ultimate load capacity is negligible.

The application of the safety formats for nonlinear finite element analysis of concrete structures shows the highest design resistance (812 kN - 76% of F_{exp}) for the E-COV method, when the maximum load is considered as the ultimate load capacity. The safety formats for nonlinear finite element analysis lead to significant higher design resistances than the ones based on symbolic expressions.

The sensitivity analyses show that the use of shells elements leads to a lower ultimate load capacity compared to reference analysis with a plane stress element model, provided that care is taken for the cross-sectional discretization. This is an important observation from the practical point of view when considering the modelling of bridge structures.

4 Case PB7: Leonhardt, Koch, Rostasy, beam IP3 (1973)

This chapter describes the experimental setup and results, analytical analysis, finite element modelling, numerical analyses and the application of safety formats for nonlinear finite element analysis for the prestressed concrete beam that is denoted with *case PB7*. Case PB7 is a post-tensioned I-shaped beam. It concerns specimen IP3 in the experiment of (Leonhardt, 1973). The beam is similar to case PB1, reported in (Rijkswaterstaat, 2017b), but with the following differences: (*i*) there are small differences in the material properties of the concrete, reinforcements and tendons; (*ii*) there are no additional stirrups in the end zones of the beam; (*iii*) the prestressing force is significantly lower; and (*iv*) no counteracting point load at midspan is applied during prestressing.

4.1 Experimental setup and results

This section provides the details of the experimental setup in terms of geometry of the beam, material properties and boundary conditions. Furthermore, the result of the test is described.

4.1.1 Geometry

Figure 65 and Figure 66 show the geometry, the reinforcement layout and the location of the post-tensioned tendons of the beam. A more detailed view on the reinforcements and tendons is shown in Figure 67. The beam has a total length of 7.0 m, a span of 6.5 m, a depth of 0.9 m and a variable thickness of the web. The beam is reinforced in the longitudinal direction with two times 6 Ø14 mm rebars in the top flange, two times 6 Ø8 mm rebars in the bottom flange and two times 2 Ø8 mm rebars in the web. The beam has stirrups Ø16 mm along the left half of the

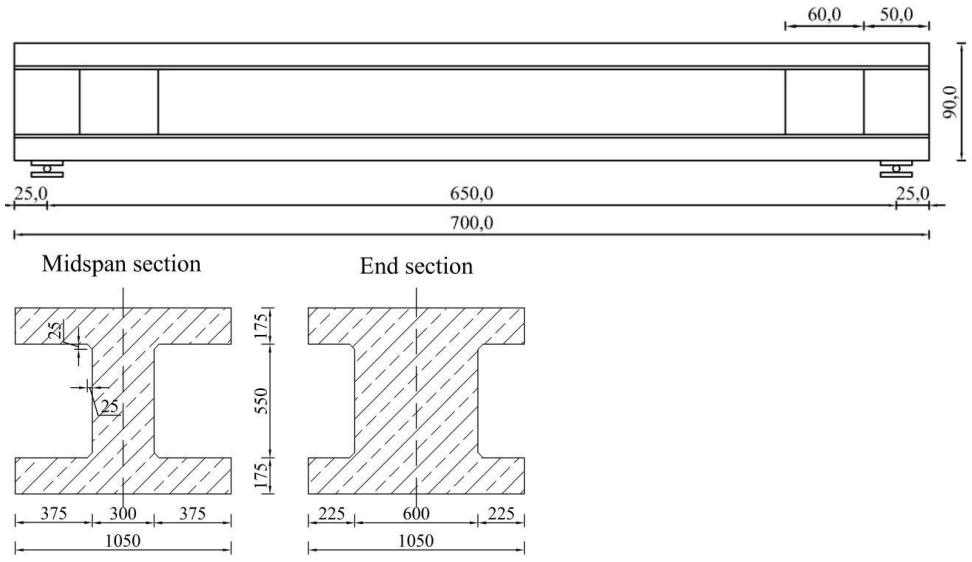

Figure 65: Case PB7. Elevation and cross-sectional details (dimensions in cm).

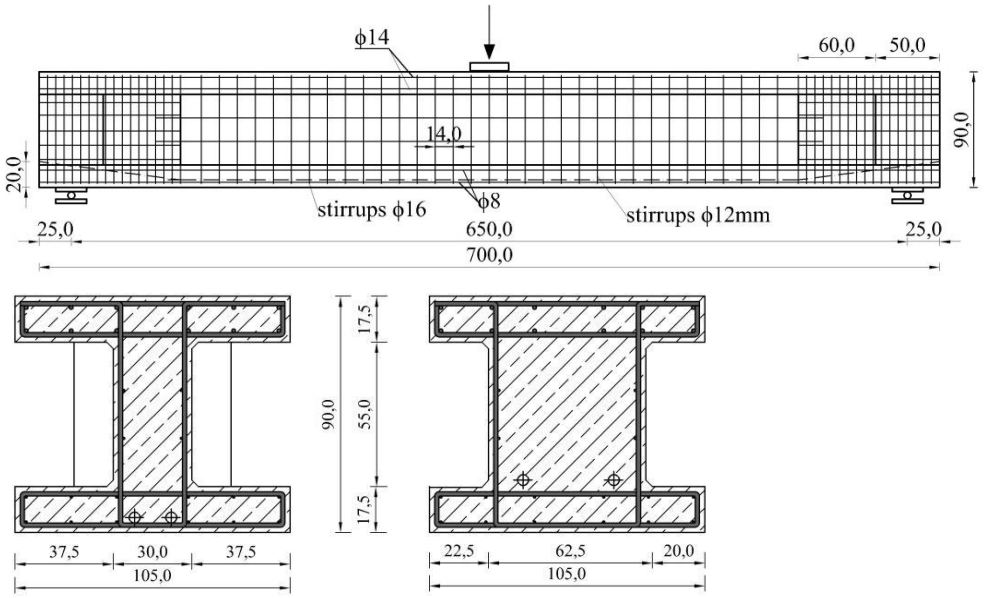

Figure 66: Case PB7. Reinforcement layout and post-tensioned tendons (dimensions in cm).[7]

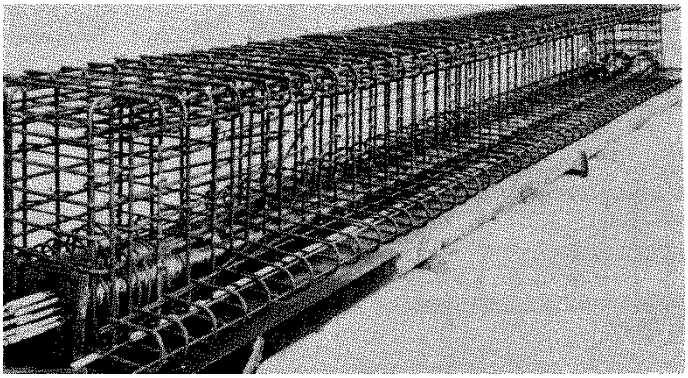

Figure 67: Case PB7. Reinforcement cage and prestressing cables.

beam and Ø12 mm along the right half of the beam, both with 140 mm spacing. Additional longitudinal reinforcement is placed in the end zones of the beam, consisting of five times 2 Ø8 mm rebars of 1100 mm length in the web.
The prestressing reinforcement consists of two post-tensioned tendons made of 12 Ø12.2 mm strands each, prestressed at both sides. The tendons have an effective depth of 825 mm (except for the end zones).

4.1.2 Material properties

Table 24 summarizes the provided concrete, reinforcement and tendon properties. The concrete compressive strength f_{cm} of 28.8 N/mm^2 is obtained from the results of tests on prisms (100 mm x 100 mm x 500 mm). Surprisingly, tests on cubes (200 mm x 200 mm x 200 mm) resulted in the same values for f_{cm}.

[7] The top figure of Figure 66 is actually showing case PB1, reported in (Rijkswaterstaat, 2017b). The reinforcement layout in case PB7 is similar, except the number of stirrups in the end zones of the beam. For case PB7 each end zone has 9 stirrups with a center-to-center distance of 130 mm.

Table 24: Case PB7. Properties of concrete, reinforcement and prestressing tendons.

Concrete properties	
f_{cm} (N/mm^2)	d_{max} (mm)
28.8	22

Reinforcement and tendon properties						
	Ø (mm)	A_s (mm)	E_s (N/mm^2)	f_{ym} (N/mm^2)	f_{tm} (N/mm^2)	ε_u (%)
Stirrups (right)	12.0	113	201105	505	582	17.5*
Stirrups (left)	16.0	201	198162	471	605	18.0*
Long. web / bottom flange	8.0	50	193257	451	556	15.0*
Long. top flange	14.0	154	203607	389	507	16.9*
Tendon	12x12.2	1403	203607	1201	1337	1.60+

* The ultimate strain is determined from test specimens with length of 100 mm.

\+ This value is obtained from the graph in the test report. The axis of the strain values ranges from 0% to 1.60%

4.1.3 *Boundary conditions and loading*

Figure 68 shows the test setup of case PB7. The simply supported beam was subjected to a three-point bending test until failure. The prestressing P_0 was applied at a load level of 98.1 kN in each cable. After prestress losses, the measured prestressing load was equal to 90.2 kN in each cable. The prestressing sequence was $1/3 \cdot P_0$ (tendon 1), $2/3 \cdot P_0$ (tendon 2), $2/3 \cdot P_0$ (tendon 1), $1/3 \cdot P_0$ (tendon 2). To connect the tendons with the concrete, the ducts were filled with grout.

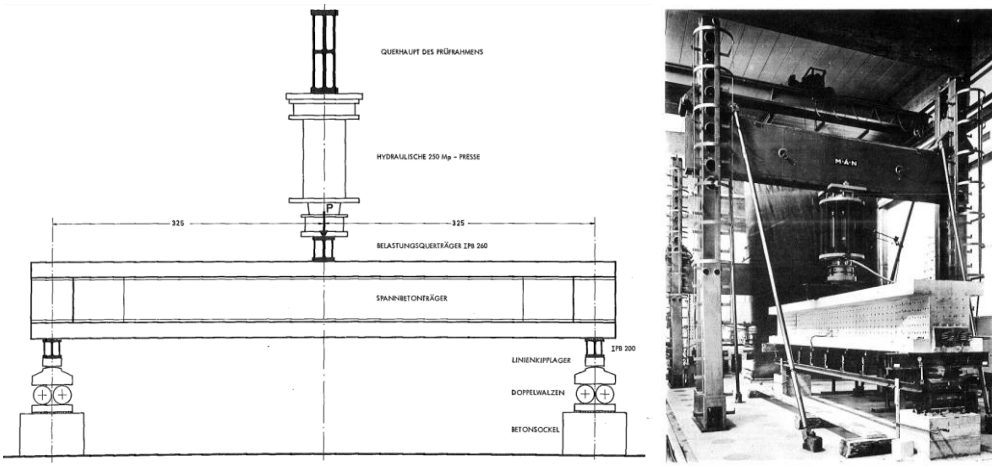

Figure 68: Case PB7. Loading and boundary conditions and experimental setup. The pictures are taken from (Leonhardt, 1973).

4.1.4 Experimental results

Figure 69 shows the load-deflection curve. The deflections were only reported until a load of 1177 kN. The dotted line in the graph concerns an extrapolation to the reported ultimate load level. The girder failed at a load of 1701 kN (173,5 Mp). The crack development and final crack pattern are shown in Figure 70 and Figure 71. The beam first showed flexural cracks with angles between 34˚ and 40˚ at a load of 177 kN (not in Figure 71). The longitudinal reinforcing bars in the bottom flange started to yield between 785 kN and 981 kN. The stirrups Ø12 in the right part of the beam started to yield around 1373 kN. At a load level of 1569 kN, about 6 stirrups yielded. The stirrups Ø16 in the left part of the beam did not yield at this stage. Figure 72 shows the stresses in the stirrups at different load levels. Beyond the load of 1569 kN no stresses in the stirrups are reported anymore. Rupture of the stirrups Ø12 was mentioned as the cause of failure by Leonhardt et al. (they denoted the failure mode as a 'shear tension failure'). Leonhardt reported a value of the bending moment at failure that is 4,7% below the calculated bending moment resistance. The stresses in the tendons did not reach the yield strength.

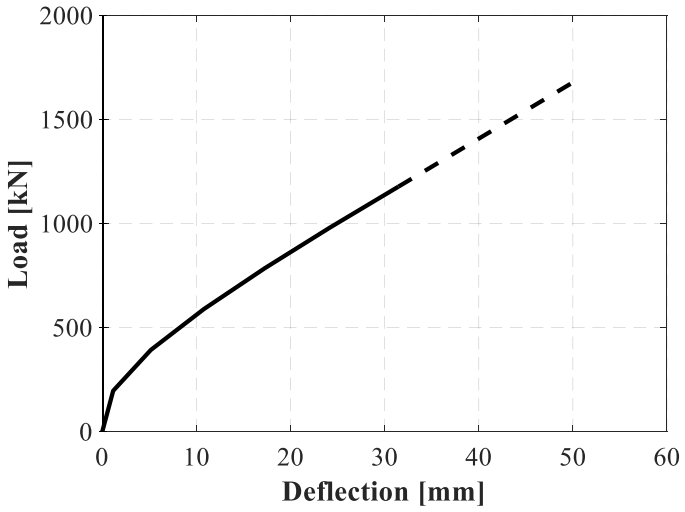

Figure 69: Case PB7. The experimentally obtained load – deflection curve.

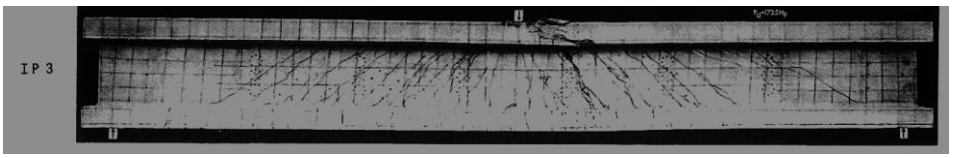

Figure 70: Case PB7. Details of the girder at failure. The picture is taken from (Leonhardt, 1973).

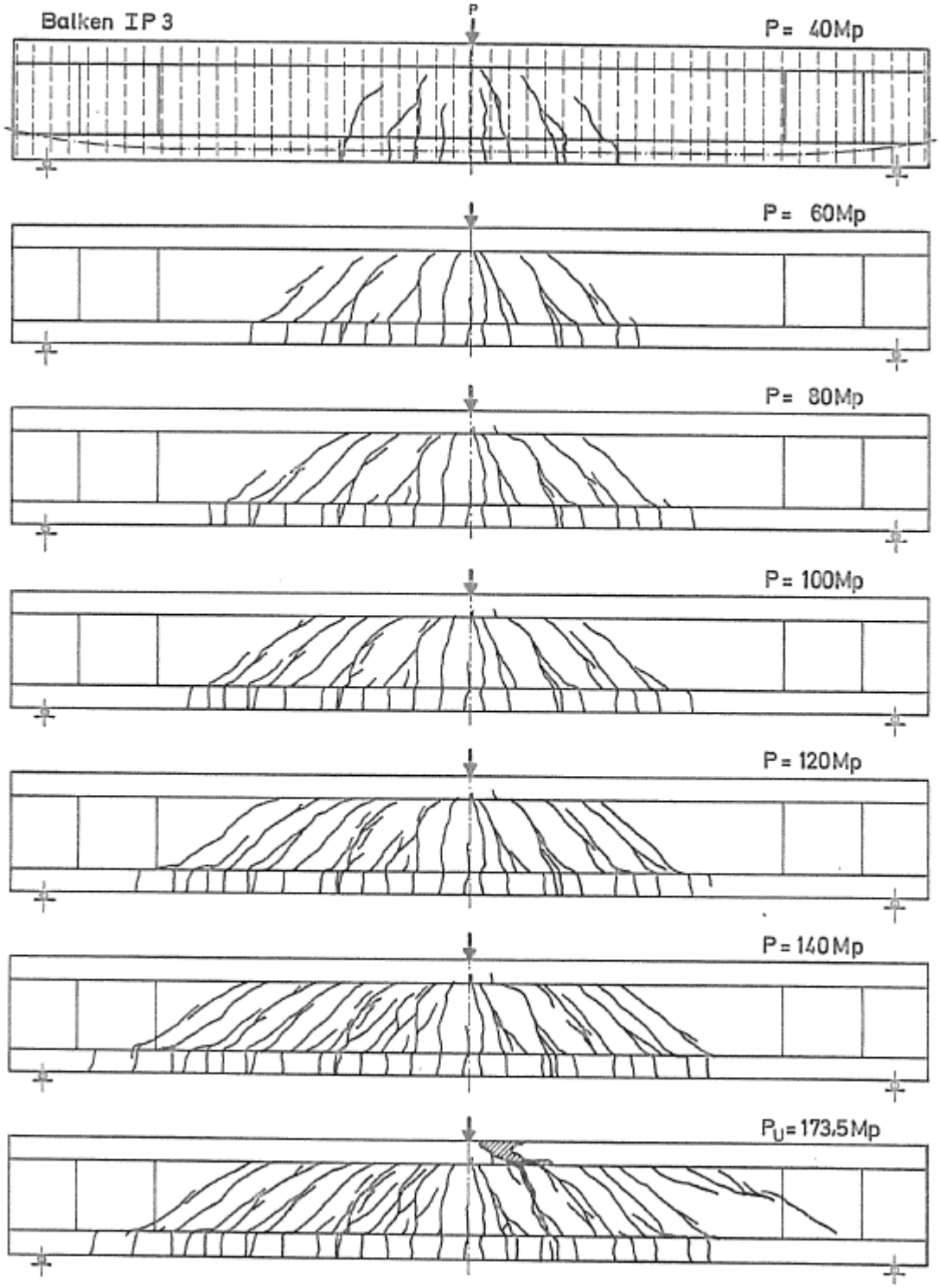

Figure 71: Case PB7. Crack development during the experiment (1Mp = 9,807 kN). The picture is taken from (Leonhardt, 1973).

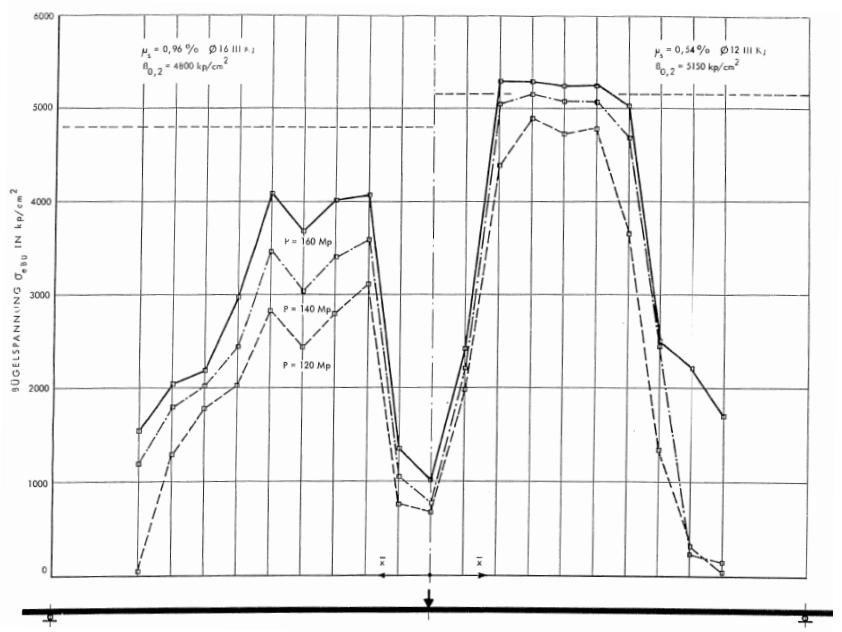

Figure 72: Case PB7. Stresses in the stirrups at the load steps 6 (1177 kN), 7 (1373 kN) and 8 (1569 kN). The picture is taken from (Leonhardt, 1973).

4.2 Analytical analysis

The critical section for shear is assumed at a distance of 0.85 m from the support. In this cross-section, the shear force from dead weight is maximal and the cross-sectional area is minimal. The critical section for the moment is under the point load, where the moment from the point load and the dead weight is maximum.

4.2.1 Cross-sectional properties

Figure 73 shows the critical cross-section of the girder. The corresponding cross-sectional properties are:

- the height of the girder h: 900 mm,
- the effective depth at the end section d_{end}: 700 mm,
- the effective depth at mid span d_{mid}: 825 mm,
- the distance to the centre of gravity from the top side z_p: 450 mm,
- the distance to the centre of gravity from the bottom z_o: 450 mm,
- the area of the end cross-section A_{end}: 697500 mm^2,
- the area of the mid span cross-section A_{mid}: 532500 mm^2.

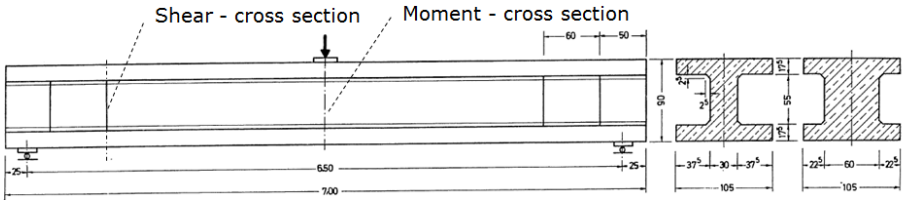

Figure 73: Case PB7. Critical cross-sections for shear and moment (dimensions in cm).

4.2.2 *Cross-sectional forces due to the loads*

In the following, the moments and shear forces due to dead weight, the prestressing force and the point load at midspan are calculated.

Dead weight

Figure 74 shows the static scheme of the girder subjected to the dead weight. Assuming a density for the reinforced concrete ρ_c of 2500 kg/m^3, the moments and shear forces at the critical cross-sections due to this load are calculated as follows:

$q_{dw,end} = A_{end} \cdot \rho_c = 0.6975 \cdot 25 = 17.4$ kN/m
$q_{dw,mid} = A_{mid} \cdot \rho_c = 0.5325 \cdot 25 = 13.3$ kN/m
$\Delta q = q_{dw,end} - q_{dw,mid} = 4.1$ kN/m
$R_{dw} = 49.8$ kN

$V_{E,dw;shear} = 2.40 \cdot 13.3 = 31.9$ kN
$M_{E,dw;shear} = 49.8 \cdot 0.85 – 13.3 \cdot 1.1^2 \cdot ½ - 0.5 \cdot 4.1 \cdot 0.85 – ½ \cdot 4.1 \cdot 0.6 \cdot 0.4 = 32.0$ kNm
$V_{E,dw;moment} = 0$ kN
$M_{E,dw;moment} = 49.8 \cdot 3.25 – 13.3 \cdot 3.5^2 \cdot ½ - 0.5 \cdot 4.1 \cdot 3.25 – ½ \cdot 4.1 \cdot 0.6 \cdot 2.80 = 70.3$ kNm

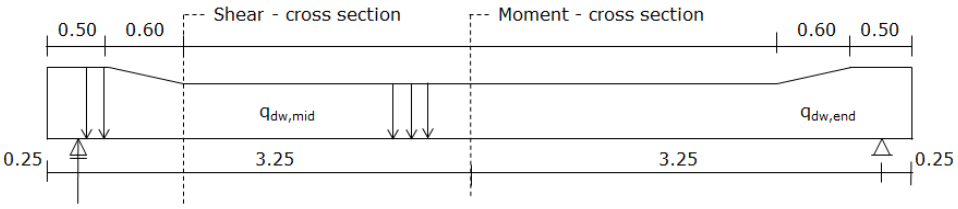

Figure 74: Case PB7. Dead weight load.

Prestressing force

Figure 75 shows the static scheme of the girder subjected to the prestressing force P. The normal force, shear force and bending moment are calculated as follows:

$e_{p,end} = d_{end} – z_p = 700 – 450 = 250$ mm
$e_{p,mid} = d_{mid} – z_p = 825 – 450 = 375$ mm
$\tan(\alpha) = (375\text{-}200) / 1100$

$N_p = P \cdot \cos(\alpha) = 2 \cdot 90.2 \cos(\alpha) = 179$ kN
$V_p = 0$ kN
$M_p = P \cdot \cos(\alpha) \cdot e_{p,end} + P \cdot \sin(\alpha) \cdot 1.10$
$= P \cdot \cos(\alpha) \cdot e_{p,mid} = 179 \cdot 0.375 = -67.1$ kN

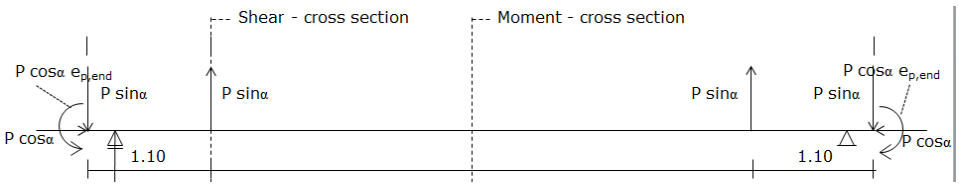

Figure 75: Case PB7. Prestress load.

External point load

Figure 76 shows the static scheme of the girder subjected to the point load. The corresponding moments and shear forces in the critical cross-sections are:

$V_{E,F;shear} = ½ \cdot F$
$M_{E,F;shear} = ½ \cdot F \cdot 0.85$
$V_{E,F;moment} = ½ \cdot F$
$M_{E,F;moment} = ½ \cdot F \cdot 3.25$

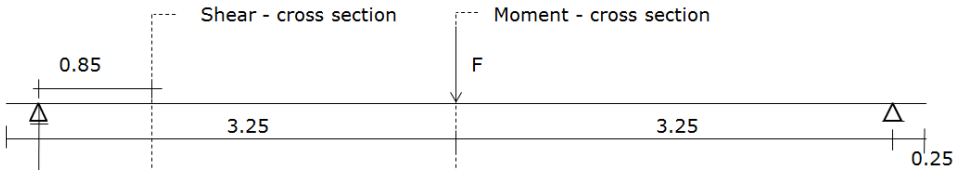

Figure 76: Case PB7. External point load.

4.2.3 *Bending moment resistance according to Eurocode*

Bending moment resistance based on mean values

The bending moment resistance and the corresponding maximum allowable point load F in Figure 76 are calculated in an iterative way, by checking equilibrium of the horizontal forces at the midspan cross-section. When *mean values* of the material parameters are used, equilibrium was found by a height of the compression zone x_u of 160 mm. The corresponding bending moment resistance $M_{R;m}$ is equal to 3009 kNm and hence the corresponding maximum allowable point load is:

$F_m = (M_{R;m} - M_{E,dw} - M_p) / (½ \cdot 3.25) = (3009 - 70.3 + 67.1) / 1.625 = 1850$ kN.

The calculation procedure is illustrated in the following, based on the determined state of equilibrium above. The following assumptions are made:

- the concrete cover is 20 mm;
- the concrete material under compression behaves according to a bi-linear σ-ε diagram with coordinates (0, 0; -1.75‰, f_{cm}; -3.5‰, f_{cm}).

Figure 77 shows the strain profile along the height of the beam. The contribution of the concrete compression zone to the normal force and bending moment resistance is:

$N_c = -0.75 \cdot b \cdot x_u \cdot f_{cm} = -0.75 \cdot 1050 \cdot 160 \cdot 28.8 = -3629 \cdot 10^3$ N.
$M_{R;c} = -N_c \cdot z_c = 3629 \cdot 10^3 \cdot (z_p - 7/18\, x_u) = 1408$ kNm.

The tendons have a working prestressing stress (after losses) of $\sigma_{pw} = F_p / A_p = 180400 / 2806 = 64.3$ N/mm^2. Using $E_p = 203607$ N/mm^2, the associated strain ε_{pw} becomes 0.32‰. The strain associated with $f_{ym} = 1201$ N/mm^2 is $f_{ym} / E_p = 5.9$‰. Since the additional strain $\Delta\varepsilon_p$ is equal to 14.6‰ (see Figure 77), the additional strain after the yielding is 14.6 + 0.32 – 5.9 = 9.0‰. With $f_{tm} = 1337$ N/mm^2 at ε_u = 16.0‰, the additional stress in the tendons after yielding becomes (1337 - 1201) · (9.0 / (16 - 5.9)) = 121 N/mm^2 . So, the total stress in the tendons is 1201 + 121 = 1322 N/mm^2, and the additional stress $\Delta\sigma_p$ is 1322 – 64.3 = 1258 N/mm^2. Hence, the contribution of the tendons to the normal force and bending moment resistance is:

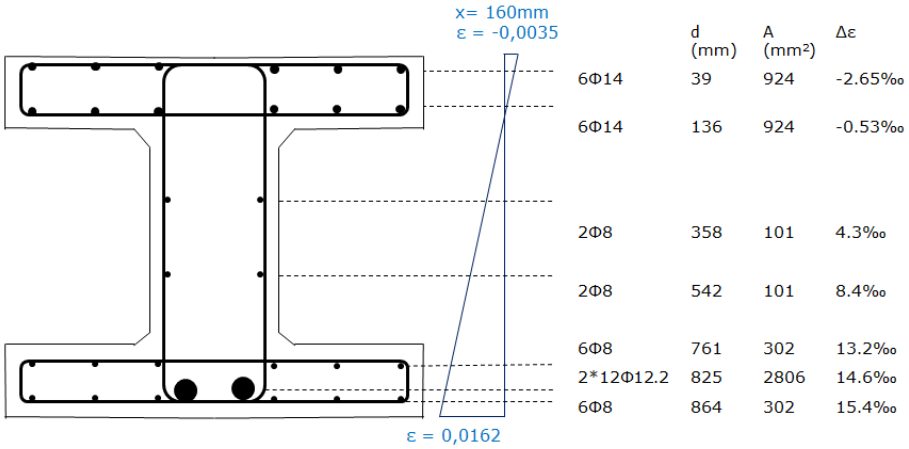

Figure 77: Case PB7. Strains along the height of the beam for a height of the compression zone of 160 mm.

$F_p = -\Delta\sigma_p \cdot A_p = 3530 \cdot 10^3$ N.
$M_{R;p} = F_p \cdot z_{tendon} = 3530 \cdot 10^3 \cdot (825 - 450) = 1324$ kNm.

The contributions of the longitudinal rebars j, in different layers over the height of the beam, to the normal force and bending moment resistance is calculated in the following way:
$F_{s;j} = \sigma_{s;j} \cdot A_{s;j}$
$M_{R;s;j} = F_{s;j} \cdot z_{s;j}$

with $\sigma_{s;j} = \varepsilon_{s;j} \cdot E_{s;j}$ for $\varepsilon_{s;j} \leq f_{ym;j} / E_{s;j}$. In case $\varepsilon_{s;j} > f_{ym;j} / E_{s;j}$, $\sigma_{s;j}$ is set to $f_{ym;j}$ neglecting the increase of the steel strength beyond yielding. The values for $\varepsilon_{s;j}$ and $z_{s;j}$ are obtained from Figure 77.

Table 25 summarizes the calculation of the bending moment resistance, showing all the separate contributions of concrete, tendons and longitudinal reinforcing bars. The total bending moment resistance $M_{R,m}$ is 3004 kNm. The total normal force at the midspan cross-section is -180 kN, which is equal to the negative value of the normal force due to prestressing N_p of 180 kN.

Bending moment resistance based on design values
Table 26 shows the design values of the material parameters in the bending moment resistance calculation. When these *design values* of the material parameters are used, equilibrium of the horizontal forces at the midspan cross-section was found by a height of the compression zone x_u of 216.5 mm. The corresponding bending moment resistance $M_{R;d}$ is equal to 2317 kNm and hence the corresponding maximum allowable point load is:

$F_d = (M_{R;d} - M_{E,dw} - M_p) / (½ \cdot 3.25) = (2317 - 70.3 + 67.1) / 1.625 = 1424$ kN.

Table 27 summarizes the calculation of the bending moment resistance based on design values, showing all the separate contributions of concrete, tendons and longitudinal reinforcing bars. The total normal force at the midspan cross-section is -180 kN, being equal to the negative value of the normal force due to prestressing N_p of 180 kN.

Table 25: Case PB7. Summary of the bending moment resistance calculation based on mean values.

	d **(mm)**	***A*** **(mm²)**	**Δε (‰)**	**Δσ (N/mm²)**	***F*** **(kN)**	**Δ*z*** **(mm)**	***M*** **(kNm)**
concrete	-	-	-	-	-3618	388	-1403.5
6 Ø14	39	923.4	-2.64	-389	-359.2	411	-147.6
6 Ø14	136	923.4	-0.52	-105	-96.7	314	-30.4
2 Ø8	358	100.6	4.36	451	45.4	92	4.2
2 Ø8	542	100.6	8.39	451	45.4	-92	-4.2
6 Ø8	761	301.8	13.2	451	136.1	-311	-42.3
tendons	825	2806	14.6	1258	3530	-375	-1323.9
6 Ø8	864	301.8	15.5	451	136.1	-414	-56.4
∑					**-180**		**-3004**

Table 26: Case PB7. Calculation of design values for the material parameters.

	Design values of the material parameters
*Concrete**	$f_{cd} = (f_{cm} - 4) / 1.5 = (28.8 - 4) / 1.5 = 16.53$ N/mm²
Longitudinal rebars Ø14	$f_{yd} = 0.9 \cdot f_{ym} / 1.15 = 0.9 \cdot 389 / 1.15 = 304$ N/mm² $f_{td} = 0.9 \cdot f_{ym} / 1.15 = 0.9 \cdot 507 / 1.15 = 397$ N/mm² $E_s = 203067$ N/mm² $\varepsilon_{ud} = 0.9 \cdot 0.9 \cdot \varepsilon_{um} = 0.9 \cdot 0.9 \cdot 16.9 = 13.7\%$
Longitudinal rebars Ø8	$f_{yd} = 0.9 \cdot f_{ym} / 1.15 = 0.9 \cdot 451 / 1.15 = 353$ N/mm² $f_{td} = 0.9 \cdot f_{ym} / 1.15 = 0.9 \cdot 556 / 1.15 = 435$ N/mm² $E_s = 193257$ N/mm² $\varepsilon_{ud} = 0.9 \cdot 0.9 \cdot \varepsilon_{um} = 0.9 \cdot 0.9 \cdot 15.0 = 12.1\%$
Tendons	$f_{p0.1d} = 0.95 \cdot f_{p0,1m} / 1.15 = 0.95 \cdot 1201 / 1.15 = 992$ N/mm² $f_{pd} = 0.95 \cdot f_{pm} / 1.15 = 0.95 \cdot 1337 / 1.15 = 1104$ N/mm² $E_p = 203607$ N/mm² $\varepsilon_{ud} = 0.9 \cdot 0.95 \cdot \varepsilon_{um} = 0.9 \cdot 0.95 \cdot 1.6 = 1.37\%$

* The "(f_{cm} – 4)" is based on DafStb-Heft 579, Reineck, Kuchma and Fitik. Note that this differs from Model Code 2010, where "(f_{cm} – 8)" is used.

Table 27: Case PB7. Summary of the bending moment resistance calculation based on design values.

	d **(mm)**	***A*** **(mm²)**	**Δε (‰)**	**Δσ (N/mm²)**	***F*** **(kN)**	**Δ*z*** **(mm)**	***M*** **(kNm)**
concrete	-	-	-	-	-2720	-370	1005
6 Ø14	39	923,4	-2.87	-304	-281	-411	115
6 Ø14	136	923,4	-1.30	-264	-244	-314	77
2 Ø8	358	101	2.3	353	36	-92	-3
2 Ø8	542	101	5.3	353	36	92	3
6 Ø8	761	302	8.8	353	107	311	33
tendons	825	2808	9.8	990	2780	375	1043
6 Ø8	864	302	10.5	353	107	414	44
∑					**-180**		**2317**

4.2.4 Shear force resistance according to Eurocode

Shear force resistance based on mean values
The shear resistance is calculated using the design provision for members with shear reinforcement:

$$V_{R,s} = \frac{A_{sw}}{s} \cdot z \cdot f_{yw} \cdot \cot\theta$$

Herein, A_{sw} is 226 mm^2 and s = 140 mm (considering the right side of the beam with 2 Ø12-140 stirrups. The intern level arm is determined by using $z = \sum(A_j \cdot z_j) / \sum A_j = 267 \cdot 10^4 / 3612 = 739$ mm, see Table 28. According to Eurocode, only the tension reinforcement is regarded in this calculation. The angle θ between the concrete compression strut and the beam axis perpendicular to the shear force is chosen in a way that $V_{R,s} = V_{R,max}$, which leads to $\theta = 24.79^{\circ}$. Hence, the shear resistance equals:

$$V_{R,s} = \frac{226}{140} \cdot 739 \cdot 505 \cdot \cot(24.79) = 1304 \cdot 10^3\ N$$

For verification, $V_{R,max}$ is also calculated: $\sigma_{cp} = N_p / A_c = 179 \cdot 10^3 / 532500 = 0.34$ N/mm^2, $\alpha_{cw} = (1 + 0.34 / 28.8) = 1.01$, $v_1 = 0.6\ (1 - 28.8 / 250) = 0.531$ and hence $V_{R,max}$ is

$$V_{R,max} = \alpha_{cw} \cdot b_w \cdot z \cdot \nu_1 \cdot f_{cm} / (\cot\theta + \tan\theta)$$
$$= 1.01 \cdot 300 \cdot 739 \cdot 0.531 \cdot 28.8/(\cot(24.79) + \tan(24.79) = 1303 \cdot 10^3\ N$$

With $V_{E,dw}$ = 31.9 kN at the shear cross-section, the maximum point load F that can be resisted by the shear reinforcement is equal to (1303 - 31.9) / 0.5 = 2542 kN. Since the load F calculated from the shear resistance is higher than the one calculated from the bending moment resistance, the latter is assumed to be governing.

Table 28: Case PB7. Calculation of the intern level arm.

	d **(mm)**	***z*** ***(mm)***	***A*** **(mm^2)**	***A·z*** **(10^4 mm^3)**
tendons	825	763	2806	214
6 Ø14	39	-23	0 (tension)	0
6 Ø14	136	74	0 (tension)	0
2 Ø8	358	296	101	3
2 Ø8	542	480	101	5
6 Ø8	761	699	302	21
6 Ø8	864	802	302	24
∑			**3612**	**267**

Shear force resistance based on design values
When using the *design values* of the material parameters, the shear resistance becomes:

$$V_{R,s} = \frac{A_{sw}}{s} \cdot z \cdot f_{yw} \cdot \cot\theta = \frac{226}{140} \cdot 722 \cdot 395 \cdot \cot(23.55) = 1056 \cdot 10^3\ N$$

The angle θ is again chosen in such a way that $V_{R,s} = V_{R,max}$. With $V_{E,dw}$ = 31.9 kN at the shear cross-section, the maximum point load *F* that can be resisted by the shear reinforcement is equal to (1056 - 31.9) / 0.5 = 2048 kN. Since the load *F* calculated from the shear resistance is higher than the one calculated from the bending moment resistance, flexural failure is also assumed to be governing in the case of using design values.

4.3 Finite element model

This section presents all the details of the finite element model for case PB7.

4.3.1 Units

The force unit is in newtons (N) and the length unit in millimeters (mm).

4.3.2 Geometry

Case PB7 is modelled in plane stress conditions. Five different parts in the finite element model can be distinguished: (*i*) the I-shaped beam; (*ii*) the support and loading plates; (*iii*) the interface between the beam and the support and loading plates; (*iv*) the reinforcements; and (*v*) the post-tensioned tendons. The modelling choices for each part are discussed in the following.

I-shaped beam: The dimensions of the I-shaped beam are based on Figure 65. To account for the varying out-of-plane thicknesses, the beam geometry is discretized over the height by three layers. The thickness variation in the web from 600 mm to 300 mm along the beam axis is applied in 12 steps at both sides of the beam.

Support and loading plates: The support plates are modelled with a length of 200 mm and a height of 60 mm. The loading plate is modelled with a length of 300 mm and a height of 60 mm. The out-of-plane thickness of the support and loading plates are set to the thickness of the flanges.

Interface: The interfaces between the beam and the support and loading plates are modelled as zero thickness interfaces.

Reinforcement: The reinforcement layout is based on subsection 4.1.1 and Figure 66. For the exact positions of the reinforcing bars and stirrups in the beam a concrete cover of 20 mm is assumed. The stirrups in the top and bottom flanges along the beam are neglected in the model[8].

[8] Since the stirrups in the top and bottom flanges have a short length (see Figure 66), it is questionable if they are effective from a mechanical point of view. When included in the model, the stirrups most likely do have an (small) effect on the crack development and subsequently they may affect the failure behaviour.

Post-tensioned tendons: The two tendons are located in one layer, see Figure 66. The effective depth between the two kinks of the cables is set to 825 mm. The ducts are not included in the model.

4.3.3 Material models and parameters

The finite element model has eight different materials: (*i*) concrete; (*ii*) structural steel; (*iii*) interface; (*iv*) reinforcing bars (2x); (*v*) stirrups (2x) and (*vi*) tendons. Table 29 summarizes all the adopted material models and properties, based on Table 24 and the RTD guidelines (Rijkswaterstaat, 2017a).

The concrete material behaviour is modelled with a total strain based orthogonal rotating smeared crack model and a band width estimator according to (Govindjee, 1995). The adopted material properties are as follows: Young's modulus E_c of 30.6 GPa, Poisson's ratio ν of 0.15, density of 2500 kg/m^3, tensile strength f_{ctm} of 2.27 MPa, tensile fracture energy G_f of 0.134 N/mm and compressive strength f_{cm} of 28.8 MPa. The parameters E_c, f_{ctm} and G_f are derived from the formulas of the *fib* Model Code 2010 (CEB/fib, 2012), based on the given f_{cm} from Table 24. The compressive fracture energy G_c is assumed to be equal to 250 G_f, following reference (Nakamura, 2001). The adopted stress-strain tension softening curve is according to (Hordijk, 1991) and for concrete under compression a parabolic softening behaviour is assumed, see Figure 78. Furthermore, lateral effects of cracking (Vecchio, 1993) and confinement (Selby, 1993) on the compressive strength and a variable Poisson's ratio dependent on the crack width are included.

The material behaviour of the steel plates is modelled with a linear-elastic stress-strain relation, using the elastic properties E_s of 210 GPa and ν of 0.3. Furthermore, the density of the steel is set to 7850 kg/m^3.
The interface between the steel plates and concrete have elastic stiffness properties of $k_n = 3.06 \cdot 10^4$ N/mm^3 and $k_t = 3.06 \cdot 10^{-2}$ N/mm^3, which are derived from the Young's modulus of the concrete[9]. A bilinear behaviour is assumed in the interface normal direction and a linear-elastic behaviour in the interface tangential direction. The normal stiffness in tension and compression are set to $3.06 \cdot 10^{-2}$ N/mm^3 and $3.06 \cdot 10^4$ N/mm^3 respectively, simulating a no-tension interface (see Figure 79).
The reinforcing bars, stirrups and tendons adopt von Mises plasticity and hardening behaviour. Figure 80 shows the stress – equivalent plastic strain curve for the tendons. Similar curves are applied to the reinforcing bars and stirrups, though with different values. The elastic modulus E_s, the yield strength f_{ym}, the ultimate strength f_{tm} and the ultimate (total) strain[10] ε_u for the different reinforcements are obtained from Table 24. The interaction between the reinforcements and concrete is modelled with perfect bond.

[9] From post-analysis checks it appears that k_t equal to $10^{-3}\,k_n$ leads to stress concentration near the loading plate, which even strongly affects the maximum load capacity for this case.
[10] The ultimate strain values from Table 24, based on test specimens with length of 100 mm, are used in the model. Since the element size is approximately 50 mm (see section 4.3.4), the numerically obtained strain values may be larger than the specified ultimate strain values to cause rupture of the bar.

Table 29: Case PB7. Summary of the adopted material models and properties in the FE model.

Material/-model	*Variable/parameter*	*Value*
Concrete	Density	2500 kg/m^3
total strain based	Young's modulus*,+	30.6 GPa
smeared rotating crack	Initial Poisson's ratio ν	0.15
model	Variable Poisson's ratio	Yes
	Compression curve	Parabolic
	Compressive strength	28.8 MPa
	Compressive fracture energy	33.42 N/mm
	Reduction due to lateral cracking	Yes
	Minimum reduction factor f_{cm}	0.4
	Influence of lateral confinement	Yes
	Tensile strength*	2.27 MPa
	Type of tension softening	Hordijk
	Tensile fracture energy*	0.134 N/mm
	Band width estimator	Govindjee
	Maximum aggregate size	22 mm
Stirrups Ø12	Young's modulus	201.11 GPa
hardening plasticity	Yield strength at ε_y = 0.25%	505 MPa
	Ultimate strength at ε_u = 17.5%	582 MPa
Stirrups Ø16	Young's modulus	198.16 GPa
hardening plasticity	Yield strength at ε_y = 0.24%	471 MPa
	Ultimate strength at ε_u = 18%	605 MPa
Longitudinal bars Ø8	Young's modulus	193.26 GPa
hardening plasticity	Yield strength at ε_y = 0.23%	451 MPa
	Ultimate strength at ε_u = 15%	556 MPa
Longitudinal bars Ø14	Young's modulus	203.61 GPa
hardening plasticity	Yield strength at ε_y = 0.19%	389 MPa
	Ultimate strength at ε_u = 16.9%	507 MPa
Tendons	Young's modulus	203.61 GPa
hardening plasticity	Yield strength at ε_y = 0.59%	1201 MPa
	Ultimate strength at ε_u = 1.6%	1337 MPa
Bond	Perfect bond	
Interface steel plates	Normal stiffness	$3.06 \cdot 10^4$ N/mm^3
Nonlinear-elasticity	Shear stiffness	$3.06 \cdot 10^{-2}$ N/mm^3
	No-tension interface (Δ - σ_n curve)	Yes
Structural steel	Density	7850 kg/m^3
linear-elastic	Elastic modulus	210 GPa
	Poisson's ratio	0.3

* Derived from relation given in *fib* Model Code 2010 (CEB/fib, 2012).

\+ The value of Young's modulus of the concrete was also derived from tests, being $266 \cdot 10^3$ kp/cm^2 = 26.1 GPa. Here, the value according to *fib* Model Code 2010 (CEB/fib, 2012) is taken.

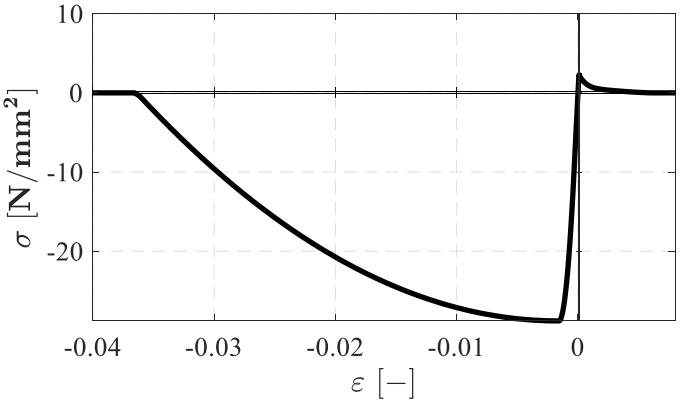

Figure 78: Case PB7. Adopted stress-strain curve for concrete (based on a crack band width of 50 mm).

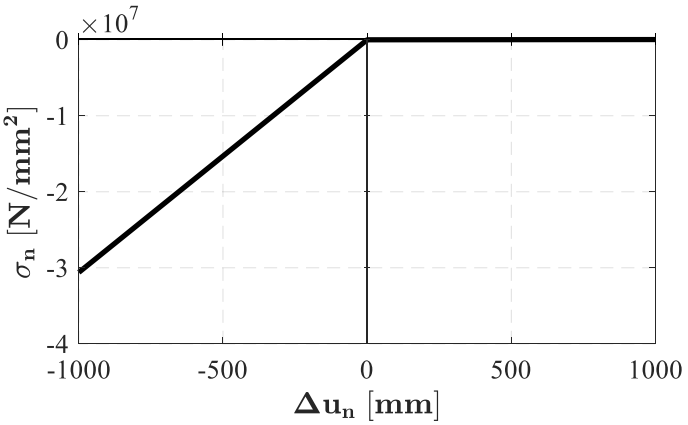

Figure 79: Case PB7. Adopted traction-displacement curve in the interface normal direction.

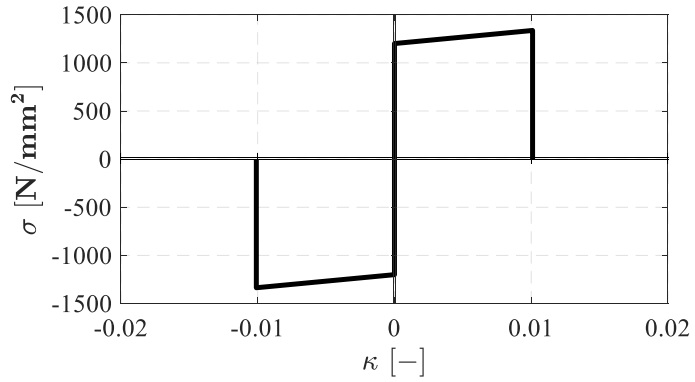

Figure 80: Case PB7. Adopted stress - equivalent plastic strain curve for the tendons.

4.3.4 Element types and finite element mesh

Figure 81 shows the 2D finite element model that is used to simulate the test. The finite element model adopts three different element types: (*i*) plane stress elements; (*ii*) interface elements; and (*iii*) embedded reinforcements.

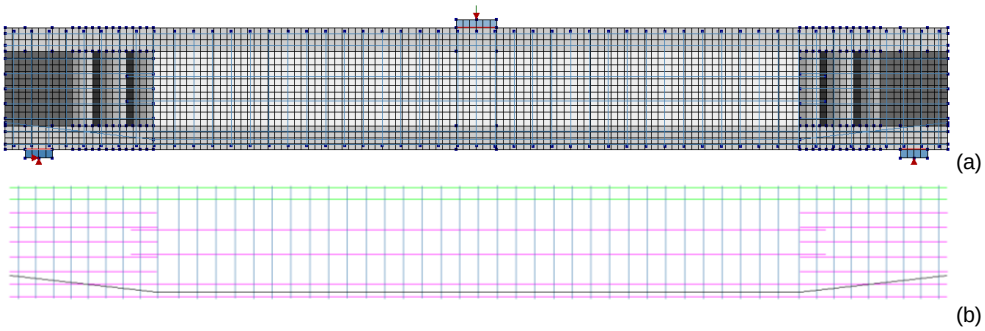

Figure 81: Case PB7. Mesh and boundary conditions (a) and embedded reinforcement sets (b).

The concrete is represented by a structured mesh, consisting of quadrilateral plane stress elements based on quadratic interpolation and using a 3 x 3 (full) Gauss integration scheme. The averaged elements sizes are set to 50 mm by 50 mm. The out-of-plane thicknesses of these elements are according to subsection 4.3.2. The steel plates, that introduce the load and support forces, are modelled by the same elements.

Zero-thickness quadratic interface elements with a 3-point Newton-Cotes integration scheme are used between the steel plates and the concrete beam. The reinforcing bars, stirrups and tendons are modelled by embedded reinforcement elements with 2-point Gauss integration, assuming perfect bond between the steel and concrete. The reinforcements only have axial stiffness.

4.3.5 *Boundary conditions and loading*

Horizontal and vertical constraints are applied at the bottom mid-nodes of the support plates. The left support is constrained in *x* and *y* direction and the right support in only the *y* direction. Furthermore, a vertical constraint is attached to the top mid-node of the loading plate in order to apply the unit displacement.

Three loads are considered in the simulation of the test: dead weight, prestressing and a unit displacement of 1 mm at the loading plate. The loads are applied in three separate load cases. The applied prestressing force at both ends of the cables is set to 90.2 kN.

4.3.6 *Load increments and convergence criteria*

The analysis is performed in two phases. In the first phase, the loads “dead weight“ and “prestressing” are subsequently applied, both in one step. The prestressing sequence, as mentioned in subsection 4.1.3, is neglected in the model. Furthermore, in this first phase there is no bond between the pre-tensioned tendons and the concrete. The second phase of the analysis is performed in displacement control with 20 steps of 0.10 mm, 140 steps of 0.25 mm and 180 steps of 0.05 mm. In this phase, the bond between the pre-tensioned tendons and the concrete is included, since the ducts are filled with grout. The regular Newton-Raphson method is used as solution procedure, with maximal 50 iterations per load step. An explicit line search technique is adopted in order to decrease the number of iterations per increment. A force tolerance of 1.0% and an energy tolerance of 0.1% are used as convergence criteria. The analysis is set to continue, even if the convergence criteria are not satisfied.

4.4 Nonlinear finite element analysis

This section presents the results of the analysis of case PB7. Attention is given to the load – deflection response, the convergence behaviour, the deformed meshes, the crack widths in concrete, the strains in steel, and Gauss point statistics.

4.4.1 Load – deflection

Figure 82 presents the load – deflection response of the beam during phase 2 of the analysis (black line), where the deflections are measured at the loading point. Six steps are marked with red dots, indicating different events in the failure process. These points are closer investigated in the following paragraphs. Non-converged steps are indicated with blue circles. The numerically obtained load bearing capacity of the beam is 1771 kN, which is visible at the fifth point.

The load – deflection response starts with small negative deflections, indicating the upward bending due to the relatively low prestress (phase 1). In the second phase of the analysis, the displacement at the loading plate is applied that causes a downward (positive) deflection of the beam. The first flexural cracks in the bottom flange of the beam are visible in load step 9, at a load of 218 kN. These cracks propagate into the web at a load of 325 kN (point 1, load step 18), which causes a change in the slope of the load – deflection response. Only two steps did not converge in this stage of the analysis. Subsequently, the analysis continued till load step 332 with only one non-converged step. During this stage of the analysis, the following is observed:

- the number and length of the flexural cracks increase more and more, until almost the entire span length is cracked;
- the longitudinal reinforcing bars in the web start to yield at a load of 422 kN (point 2, load step 28). Initially, these yielding spots are located at the intersection points of cracks with large crack widths. Later, yielding is observed along significant parts of the bars;
- the longitudinal reinforcing bars in the bottom flange start to yield at a load of 726 kN (point 3, load step 61); Initially, these yielding spots are located at the intersection points of cracks with large crack widths. Later, yielding is observed along significant parts of the bars;
- the concrete in the top flange under the loading plate starts to crush at a load of 1202 kN (point 4, load step 116). Simultaneously, two stirrups Ø12 at the right hand side of the beam start to yield. This number of stirrups increases to 14, when the maximum capacity is reached. The stirrups Ø16 at the left part of the beam did not yield in this stage of the analysis;
- the beam reaches its maximum capacity of 1771 kN (point 5, load step 332);
- the global stiffness of the beam hardly changes between the points 1 and 5.

Note that the reinforcing bars in the web yield earlier than the reinforcing bars in the bottom flange. From the numerical point of view, this can be explained by the larger crack widths that are observed in the web, resulting in higher strain values in the embedded reinforcement there. Note further that the prestressed tendons did not yield before the peak. This explains the more or less constant slope of the load – deflection response in the pre-peak regime.
Once the maximum load is reached, the beam fails. The results at point 6 (at a load of 252 kN, load step 358) indicate that this failure is accompanied with crushing of

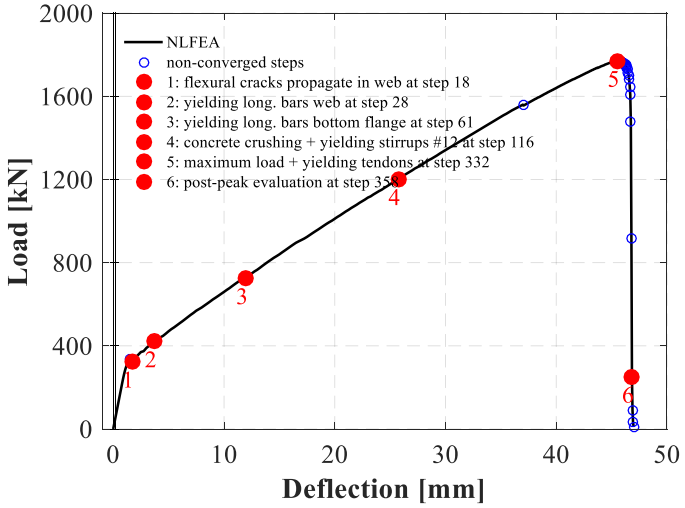

Figure 82: Case PB7. Load – deflection curve during phase 2 of the analysis.

the concrete in the top flange and the web of the beam, at the right side of the loading plate. However, these results should be treated with caution, since after load step 332 none of the load steps has reach convergence anymore and so they belong to an unreliable equilibrium path.

4.4.2 *Convergence behaviour*

Figure 83 shows the evolution of the relative out of balance force and relative energy variation during the analysis. The red dots refer to the points in the load – deflection curve, see Figure 82. The black lines in the two graphs indicate the force norm and energy norm respectively.

Throughout the analysis, the convergence is mainly reached on the basis of the energy norm. Beyond the maximum load at point 5, none of the steps satisfy the convergence criteria anymore and the force and energy norms reveal a diverging trend.

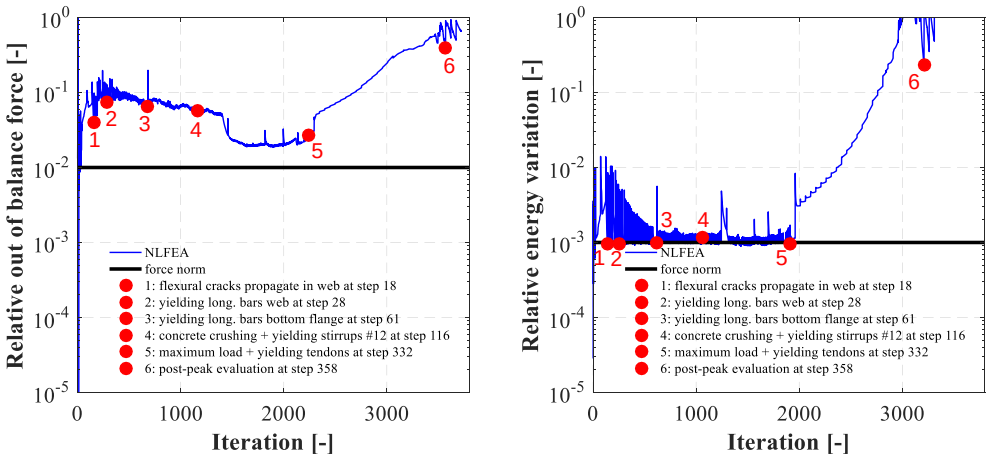

Figure 83: Case PB7. Evolutions of the relative out of balance force and relative energy variation.

4.4.3 Deformed meshes

Figure 84 presents the meshes with normalized deformations at the load steps 18, 28, 61, 116, 332 and 358. In the first five plots the beam mainly show bending deformations. The deformed mesh that belongs to load step 358 (after failure) reveal a column of elements with distorted shapes, at the left side of the loading plate. The stiffness in these elements is entirely vanished. Though this load step is not converged, it suggest that failure mode can be characterized as a compression failure.

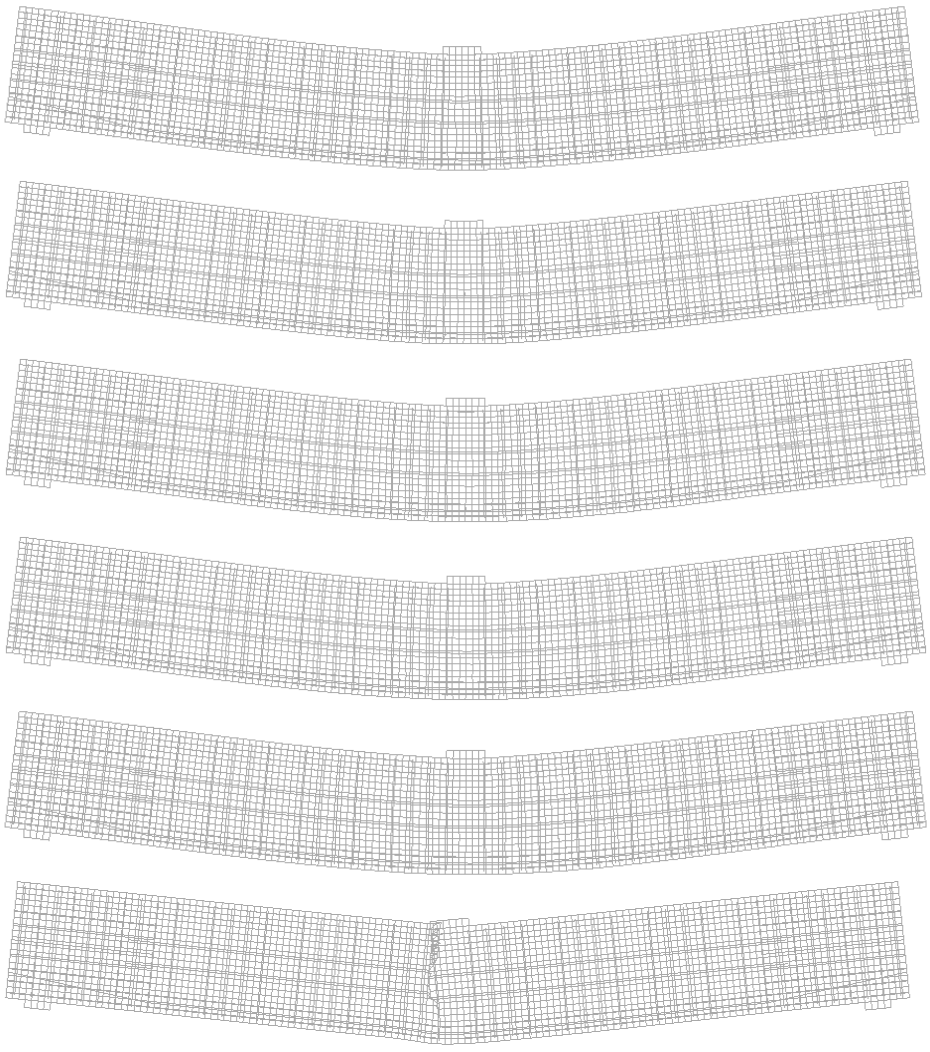

Figure 84: Case PB7. Deformed meshes at the load steps 18, 28, 61, 116, 332 and 358, see Figure 82.

4.4.4 Crack widths and principal strains in concrete

Figure 85 presents the crack widths plots at the load steps 18, 28, 61, 116, 332 and 358. Figure 86 and Figure 87 present the plots with the maximum principal strains (ε_1) and minimal principal strains (ε_2) at these load steps respectively. The plots reveal the crack development in the beam, starting from a few flexural cracks to a widespread and almost symmetric crack pattern over the entire beam.

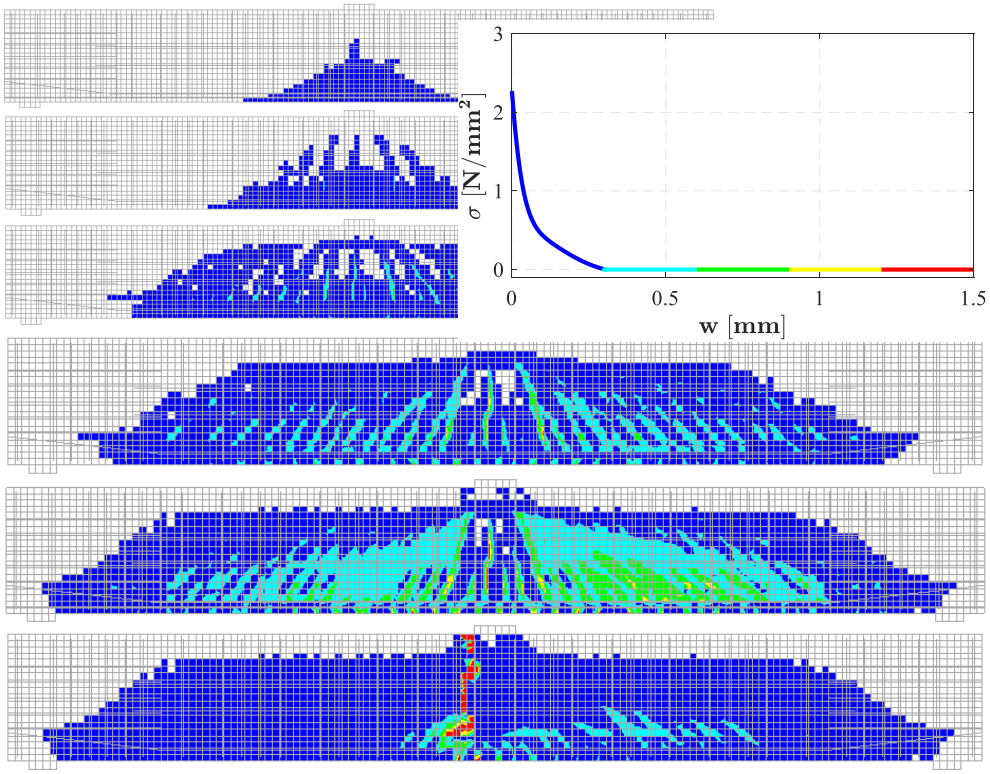

Figure 85: Case PB7. Crack width plots at the load steps 18, 28, 61, 116, 332 and 358, see Figure 82.

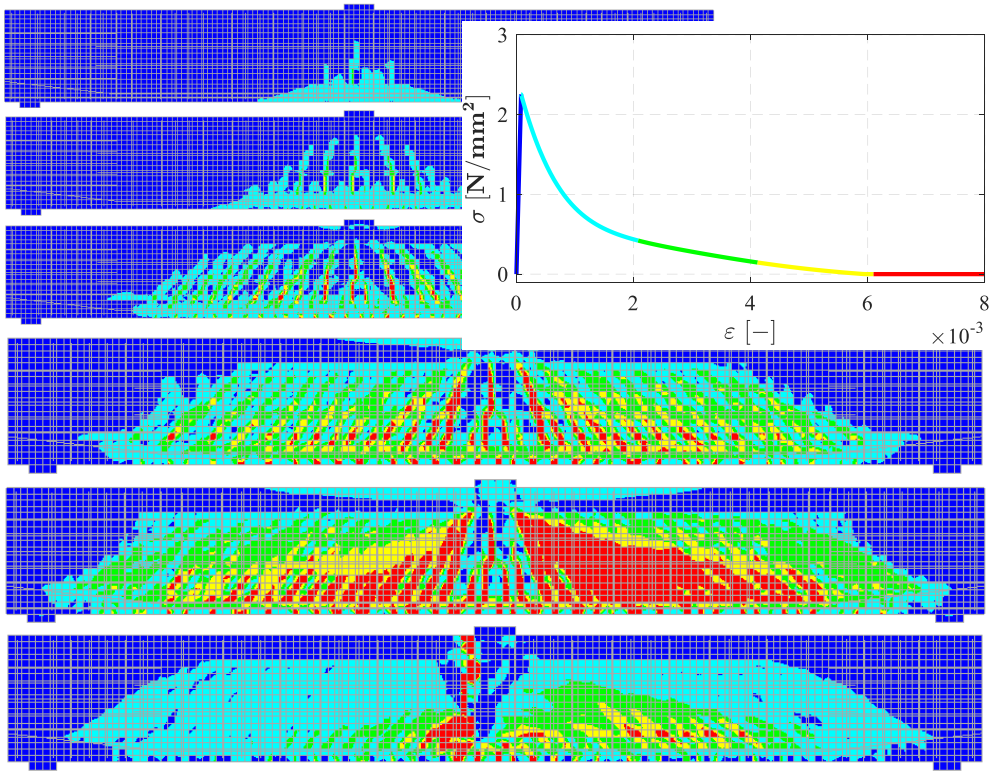

Figure 86: Case PB7. Maximum principal strain plots (ε_1) at the load steps 18, 28, 61, 116, 332 and 358, see Figure 82.

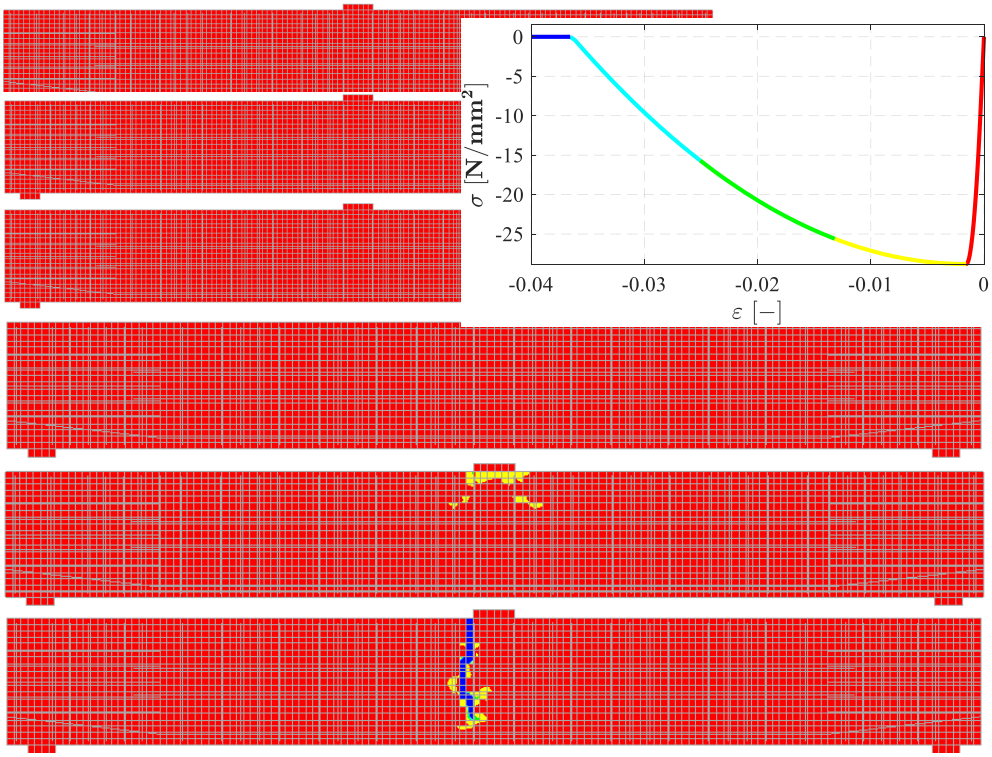

Figure 87: Case PB7. Minimum principal strain plots (ε_2) at the load steps 18, 28, 61, 116, 332 and 358, see Figure 82.

At the peak load (point 5, load step 332), the symmetry in the crack pattern is disappeared and larger crack widths are observed in the right part of the beam. This part of the beam contains stirrups with a lower cross-sectional area than in the left part of the beam. The minimal principal strain plot that belongs to this load step shows that the concrete under loading plate is crushing. Beyond the peak load (point 6, load step 358), the cracks and crushing zone is localized in a narrow band of elements over the height of the beam, at the left side of the loading plate. This result, however, is from an unreliable equilibrium path and therefore has only a qualitative value.

Note that the initial crushing of the concrete underneath the loading plate is to some extent surprising. From experimental work, it is more common to observe crushing of the concrete next to loading plate. Plots of stresses in horizontal direction at different load steps reveal no stress concentrations in the beam near the loading plate, which excludes a malfunction of the interface elements.

4.4.5 Strains in steel

Figure 88 presents the strains in the longitudinal reinforcing bars at the load steps 18, 28, 61, 116, 332 and 358. The colour legend scale is related to the stress – equivalent plastic strain curve of the bars Ø8. Figure 89 presents the strains in the stirrups at these load steps. The colour legend scale is related to the stress – equivalent plastic strain curve of the stirrups Ø12.

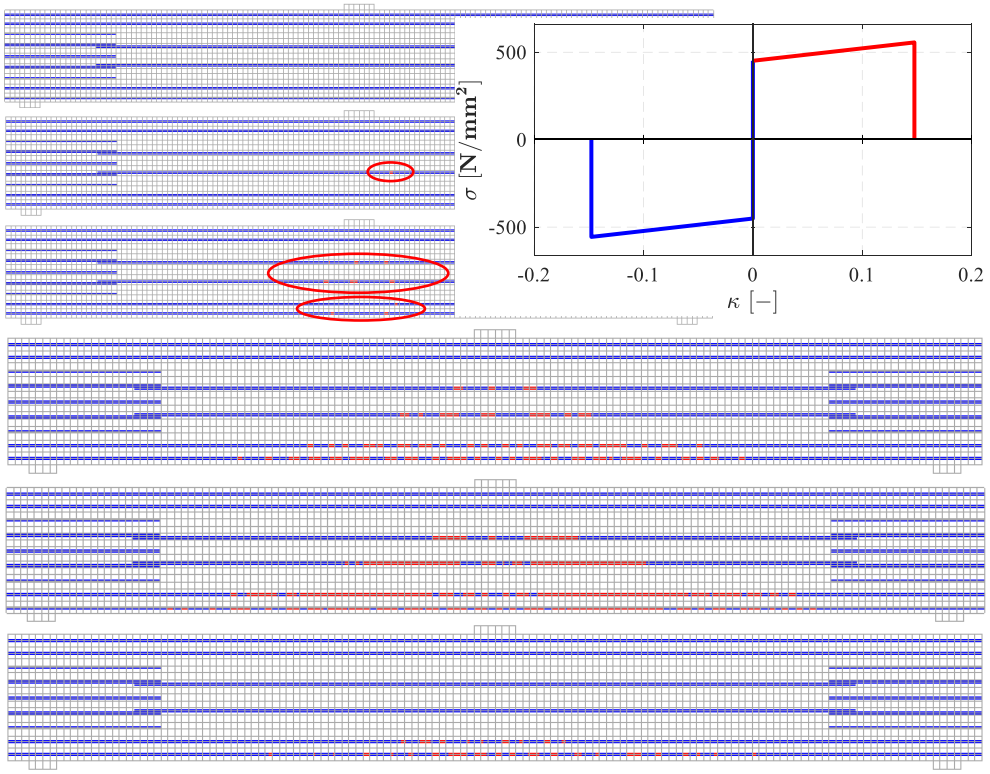

Figure 88: Case PB7. Strains in longitudinal reinforcing bars at the load steps 18, 28, 61, 116, 332 and 358, see Figure 82.

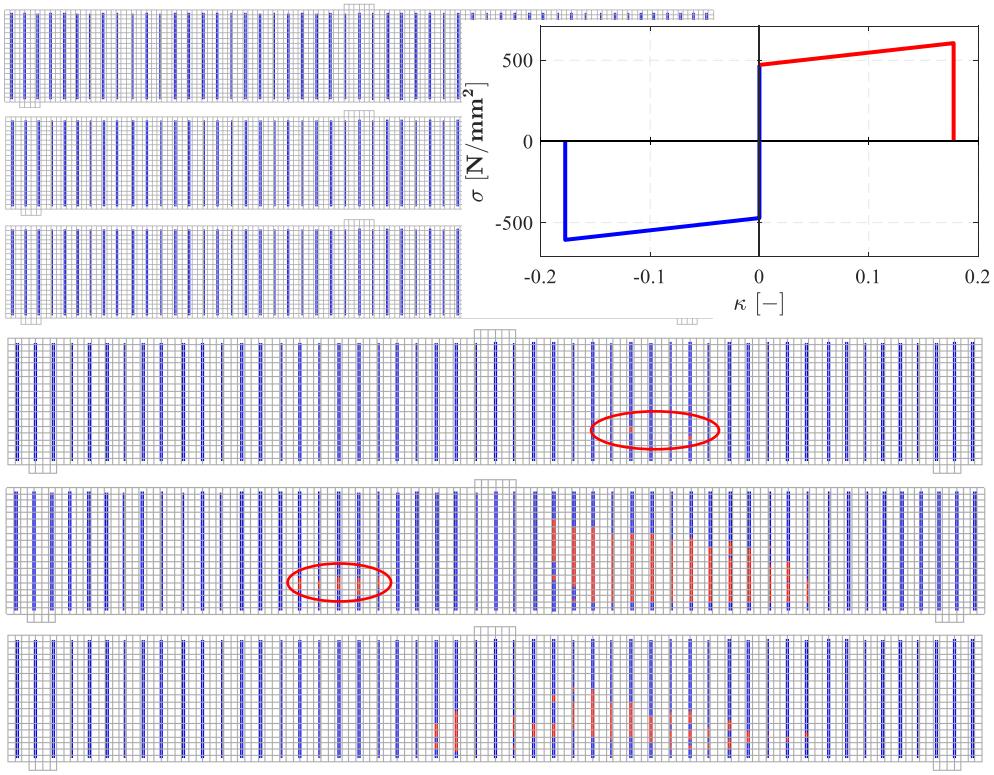

Figure 89: Case PB7. Strains in stirrups at the load steps 18, 28, 61, 116, 332 and 358, see Figure 82.

The first yielding is observed in the bottom longitudinal bars of the web (point 2, load step 28). In the subsequent load steps, the number of yielding spots increases and merge to larger zones. The longitudinal bars in the bottom flange and the stirrups Ø12 in the right part of the beam start to yield at point 3 (load step 61) and point 4 (load step 116) respectively.

The number of yielding stirrups increases from two to 14 at the peak load (point 5, load step 332). At this point, also four stirrups Ø16 in the left part of the beam yield. In none of the reinforcements, strain values close to the ultimate strain values are observed during the analysis. The tendons behave elastically until the peak. When the peak load is reached, yielding around midspan is observed during several subsequent load steps.

4.4.6 Gauss point statistics

Figure 90 presents the evolutions of the number of Gauss points with earlier and present plastic behaviour (crushing or yielding) and the number of cracked Gauss points. The graphs highlight the events, as described before.

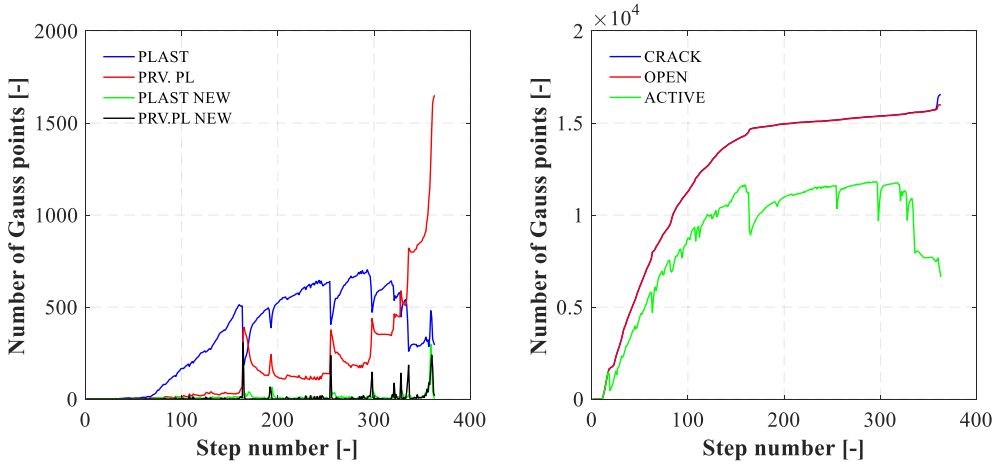

Figure 90: Case PB7. Evolutions of the number of Gauss points with (former) plastic behaviour (crushing or yielding) and the number of cracked Gauss points.

4.5 Application of safety formats for nonlinear finite element analysis

This section demonstrates the application of the three safety formats *global resistance factor method* (GRF), *estimation of the coefficient of variation of the resistance* (E-COV) and the *partial factor method* (PF), as proposed in *fib* Model Code 2010 (CEB/fib, 2012). In total, four different nonlinear finite element analyses need to be performed.

Table 30 to Table 35 summarize the input geometry and material parameters of the concrete, reinforcing bars and tendons for the four analyses. The input parameters are based on the mean values, characteristic values, mean GRF values and design values, which are calculated according to Annex A of (Rijkswaterstaat, 2017a). According to this annex, only material properties are changed and the geometry properties are kept constant.

Table 30: Case PB7. Concrete properties for the nonlinear analyses of the safety formats.

	f_c (N/mm²)	f_{ct} (N/mm²)	E_c (N/mm²)	v (-)	G_f [11] (N/mm)	G_c (N/mm)
Mean	28.80	2.27	30589	var	0.1337	33.42
Characteristic	20.80	1.59	27445	var	0.1261	31.51
Mean GRF	17.68	2.04	25998	var	0.1224	30.61
Design	13.87	1.06	23975	var	0.1172	29.30

Table 31: Case PB7. Stirrup Ø12 properties for the nonlinear analyses of the safety formats.

	Ø (mm)	A_s (mm²)	f_y (N/mm²)	f_t (N/mm²)	E_s (N/mm²)	ε_{sy} (-)
Mean	12.0	113.1	505.00	582.00	201105	0.0025
Characteristic	12.0	113.1	457.40	527.14	201105	0.0023
Mean GRF	12.0	113.1	503.14	579.86	201105	0.0025
Design	12.0	113.1	397.74	458.38	201105	0.0020

Table 32: Case PB7. Stirrup Ø16 properties for the nonlinear analyses of the safety formats.

	Ø (mm)	A_s (mm²)	f_y (N/mm²)	f_t (N/mm²)	E_s (N/mm²)	ε_{sy} (-)
Mean	16.0	201.1	471.00	605.00	198162	0.0024
Characteristic	16.0	201.1	426.60	547.97	198162	0.0022
Mean GRF	16.0	201.1	469.27	602.77	198162	0.0024
Design	16.0	201.1	370.96	476.50	198162	0.0019

Table 33: Case PB7. Properties of the longitudinal reinforcing bars Ø8 for the nonlinear analyses of the safety formats.

	Ø (mm)	A_s (mm²)	f_y (N/mm²)	f_t (N/mm²)	E_s (N/mm²)	ε_{sy} (-)
Mean	8.0	50.27	451.00	556.00	193257	0.0023
Characteristic	8.0	50.27	408.49	503.59	193257	0.0021
Mean GRF	8.0	50.27	449.34	553.95	193257	0.0023
Design	8.0	50.27	355.21	437.91	193257	0.0018

Table 34: Case PB7. Properties of the longitudinal reinforcing bars Ø14 for the nonlinear analyses of the safety formats.

	Ø (mm)	A_s (mm²)	f_y (N/mm²)	f_t (N/mm²)	E_s (N/mm²)	ε_{sy} (-)
Mean	14.0	153.9	389.00	507.00	203607	0.0019
Characteristic	14.0	153.9	352.33	459.21	203607	0.0017
Mean GRF	14.0	153.9	387.57	505.13	203607	0.0019
Design	14.0	153.9	306.38	399.31	203607	0.0015

[11] Note that the variations in the fracture energies G_f and G_c are surprisingly small and their values do not proportionally change with the values of the tensile strength f_t and compressive strength f_c.

Table 35: Case PB7. Tendon properties for the nonlinear analyses of the safety formats.

	Ø (mm)	A_s (mm²)	f_y (N/mm²)	f_t (N/mm²)	E_s (N/mm²)	ε_{sy} (-)
Mean	12.2	116.9	1201.0	1337.0	203607	0.0059
Characteristic	12.2	116.9	1087.8	1211.0	203607	0.0053
Mean GRF	12.2	116.9	1196.6	1332.1	203607	0.0059
Design	12.2	116.9	945.91	1053.0	203607	0.0046

The load increment scheme is determined per analysis and slightly differs from the one discussed in subsection 4.3.6.

Figure 91 presents the load – deflection curves of the analyses with mean values, characteristic values, mean GRF values and design values for the input parameters of the concrete, reinforcing bars and tendons. Their corresponding peak values are 1771 kN, 1416 kN, 1326 kN and 1107 kN respectively, which reveals a correlation between the predicted load capacity and the concrete compressive strength. The analyses with characteristic values, mean GRF values and design values reveal a similar failure behaviour as the analysis with mean values. Using the expressions provided by Annex A of (Rijkswaterstaat, 2017a), the design resistances for the safety formats can be calculated. These values are compared in Figure 92 and Table 36, together with the results of the analytical calculations from subsection 4.2.3. The resistances based on mean values of the input parameters are also added. Note that the analysis with label “No safety format” refers to the analysis with mean values, discussed in the previous section.

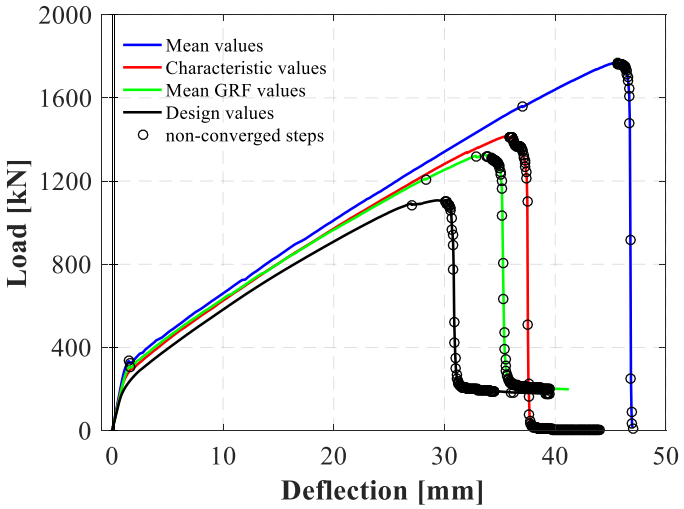

Figure 91: Case PB7. Load – deflection curves of the analyses with mean values, characteristic values, mean GRF values and design values for the input parameters of the concrete, reinforcing bars and tendons.

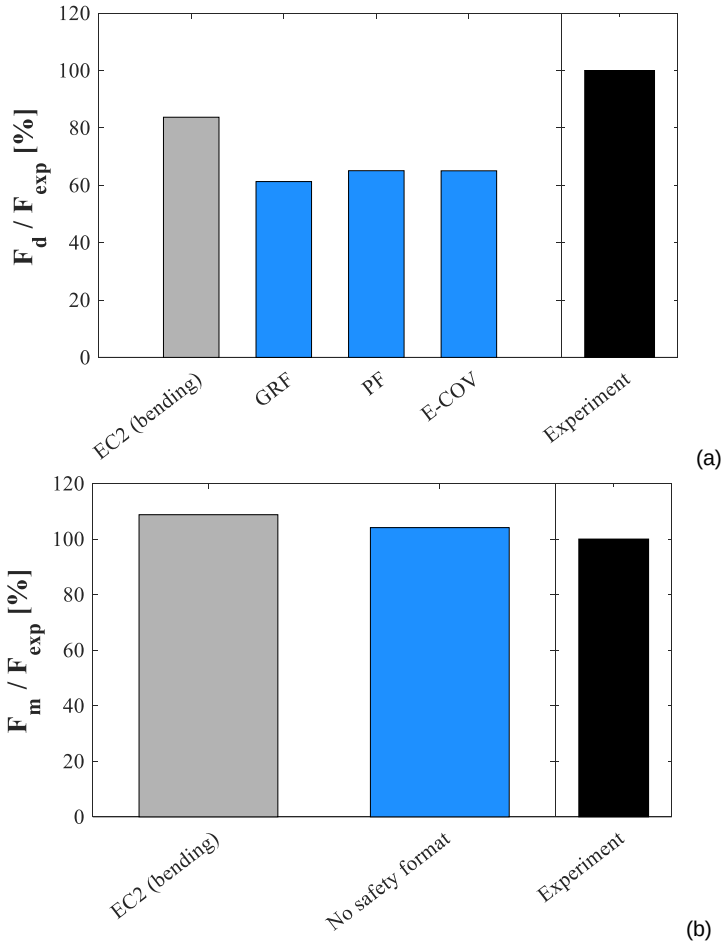

Figure 92: Case PB7. Design values of the resistance (F_d) according to the different safety formats (a) and the resistances (F_m) based on the mean values of the input parameters (b), expressed in terms of a percentage of the experimentally obtained ultimate load (F_{exp}). The grey colour bars refer to the calculations with symbolic expressions, the blue colour bars to the nonlinear finite element analyses.

Table 36: Case PB7. Design values of the resistance according to the different safety formats and the resistances (F_m) based on the mean values of the input parameters (in kN).

	Design values (F_d)				**Mean input (F_m)**	
F_{exp}	*EC2 (bending)*	*GRF*	*PF*	*E-COV*	*EC2 (bending)*	*No safety formats*
1701	1424	1043	1107	1106	1850	1771

4.6 Sensitivity analysis

This section investigates the sensitivity of the numerical results of the previous analysis with mean values with respect to the (*i*) crack model; (*ii*) the level of prestressing force; (*iii*) the geometrical representation / element type, and (*iv*) the tensile strength of the concrete. The variations are explained in the following. For each analysis, a new load increment scheme is determined. These schemes slightly differ from the one discussed in subsection 4.3.6.

Crack model: In this analysis the rotating crack model is replaced by a fixed crack model. All the other modelling aspects are the same as described in section 4.3. The fixed crack model requires the specification of a shear retention relation. In this study, the damaged based shear retention relation and the aggregate size based shear retention relation are considered. In the former relation, the shear retention *G* depends on the normal stiffness decay (and so on the crack normal strain), via:

$$G = \frac{E_n}{2(1+\nu)} \tag{11}$$

In the latter relation, the shear retention factor β depends on the aggregate size d_{aggr}, the crack normal strain ε_n and the crack band width *h*, via:

$$\beta = 1 - \left(\frac{2}{d_{aggr}} \right) \cdot \varepsilon_n \cdot h \tag{12}$$

The damaged based shear retention relation is characterized by a relatively rapidly decreasing shear stiffness and the aggregate size based shear retention relation is characterized by a relatively slow decreasing shear stiffness.

Level of prestressing force: In this analysis the prestressing force *P* is increased by 10%. All the other modelling aspects are the same as described in section 4.3. In the context of ULS verification, the level of *P* is less importance in case of problems with bending failure. However, in case of problems with shear failure the level of *P* can be quite important, since it will determine the (bending) crack development and the principal stress distribution in the structure.

Geometrical representation / element type: In this analysis the beam is modelled by shell elements with quadratic interpolation. The model has a T-shape in cross-sectional view, meaning that the top flange is modelled by “out-of-plane” shell elements and the web and bottom flange are modelled by “in-plane” shell elements. Figure 93 shows the thickness directions and their thicknesses in the adopted cross- sectional discretization. The shell elements are modelled in the center lines of the flanges and web. Hence, the cross-sectional area and moment of inertia in the model differ from the real cross-sectional area and moment of inertia.
Compared to the reference model, presented in section 4.3, the stirrups in the top flange of the beam are also included in the model. The addition of these stirrups prevent an unrealistic event, in which a large splitting crack arises in the top flange along the longitudinal axis of the beam. Further modelling aspects of this shell element model are the same as described in section 4.3. Figure 94 shows the mesh of the shell element model.
Note that the adopted cross-sectional discretization in the shell element model is only one of the possibilities. This approach is straightforward, but also non-conservative due to 5% redundant material in the top flange – web connection.

Tensile strength of the concrete: In this analysis the mean value of the concrete tensile strength is reduced by 32.8%, leading to $f_t = 0.672\, f_{t;m}$. All the other modelling aspects are the same as described in section 4.3.

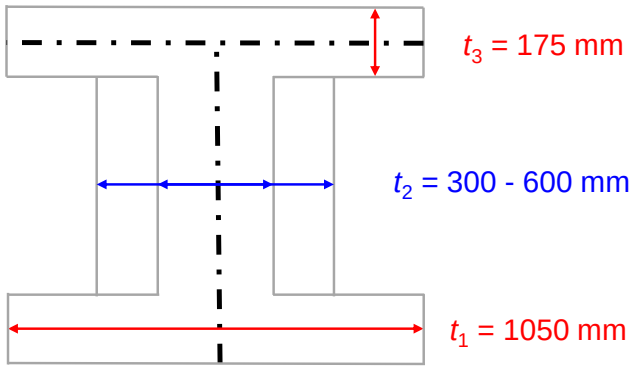

Figure 93: Case PB7. Cross-sectional discretization for the shell model.

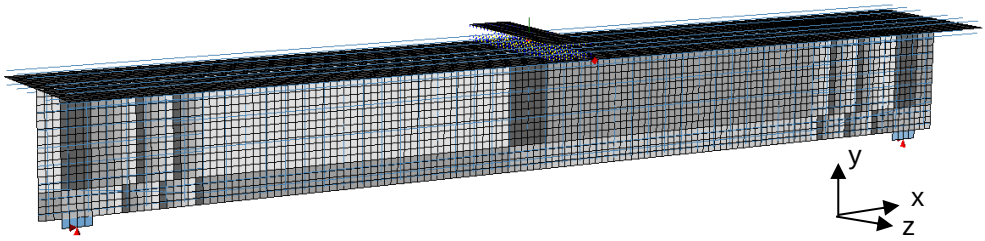

Figure 94: Case PB7. Mesh of the shell element model.

Figure 95 presents the load – deflection responses of the sensitivity analyses. The maximum observed values are summarized in Table 37. More detailed results of these analyses are provided in Annex B, which contains the contour plots with deformed meshes, crack widths, maximum principal strains (ε_1), minimal principal strains (ε_2), the strains in the stirrups, the strains in the reinforcing bars and the strains in the strands around the peak and in the post-peak regime.

From the comparison with the results of the reference analysis in section 4.4, it can be noted that the adopted crack model strongly influences the structural response. Furthermore, the adopted shear retention relation in the fixed crack model appears to be a rather governing model parameter. The analysis with the damaged based shear retention relation shows a 30% lower resistance compared to the reference analysis, whereas the analysis with the aggregate size based shear retention relation shows a 9% higher resistance and a stiffer and more ductile behaviour (with yielding of the tendons). The results indicate that the two adopted formulations of the shear stiffness degradation trigger different failure modes, i.e. a shear compression failure vs a bending failure, which is confirmed from the contour plots in Annex B.

The level of prestress do not affect the results. An increase of 10% in the prestressing force leads to a similar load capacity and failure behaviour.

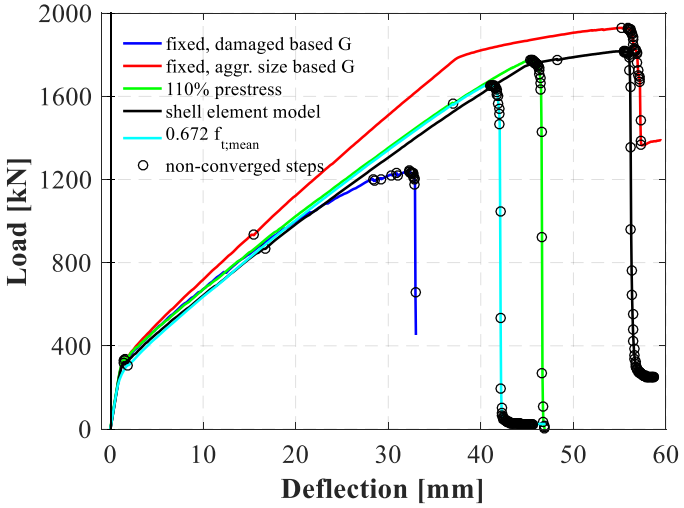

Figure 95: Case PB7. Load – deflection curves of the sensitivity analyses.

Table 37: Case PB7. Maximum load capacities of sensitivity analyses.

Analysis	**Maximum load capacity (kN)**
Reference analysis (“No safety format”, mean values)	1771
Fixed crack model – damaged based shear retention	1241
Fixed crack model – aggr. size based shear retention	1929
10% higher prestressing force	1774
Shell element model	1817
Reduced tensile strength of the concrete	1660

The use of shell elements instead of plane stress elements reveals considerable effects on the results. Firstly, the shell element model leads to a 2.6% higher load capacity. More important, however, is that the shell model predicts another structural failure. From Annex B, it can be observed that: (*i*) the failure is not preluded by crushing of the concrete in the compression zone; (*ii*) the tendons are yielding prior to failure; (*iii*) the right part of the beam is heavily cracked and the top flange seems to shear off. These observations indicate that the adopted cross-sectional discretization of the cross-section of the beam is not conservative and that in this particular case the 5% surplus material in the compression zone changes the failure mode.

The adopted value of the tensile strength of the concrete has a limited effect on the results. A reduction of 32.8% in the tensile strength results in: (*i*) a reduction of 34% of the load at which the first bending cracks appear (218 kN versus 163 kN); and (*ii*) a reduction of 6.3% of the maximum load capacity. The latter can be explained by the fact that the failure mode is dominated by the material behaviour of the reinforcement and the behaviour of the concrete under compression. The analysis with a reduced value for the tensile strength does not show yielding of the tendons.

4.7 Concluding remarks

The failure mechanism and the sequence of events are well simulated by the numerical analyses. Table 38 compares the numerically and experimentally obtained loads for different events. Mean values of the material properties have been used in the numerical analysis. The maximum observed load value is considered as the ultimate load capacity.

Considering a mean concrete tensile strength according to (CEB/fib, 2012), the numerical analysis overestimates the load level at the first flexural crack by 23%. The numerical analysis overestimates the ultimate load capacity by 4%.

The application of the safety formats for nonlinear finite element analysis of concrete structures shows the highest design resistance (1107 kN - 65% of F_{exp}) for the PF method. The EC2 approach leads to significant higher design resistances: 1424 kN (84% of F_{exp}) for the bending moment design resistance.

The sensitivity analyses show that the use of shells elements leads to a slightly higher ultimate load capacity of 2.6% compared to reference analysis with a plane stress element model, provided that care is taken for the cross-sectional discretization. This is an important observation from the practical point of view when considering the modelling of bridge structures. Furthermore, a relatively small influence of the concrete tensile strength on the ultimate load capacity is observed.

Table 38: Case PB7. Comparison between numerical results and experimental results (mean values).

	f_{ctm} (MPa)	**NLFEA (kN)**	**Experiment (kN)**
Load first bending crack	2.27	218	177
Maximum load	2.27	1771	1701 (considered as ultimate capacity)

5 Recommendations for RTD guidelines

As expressed in the preface of the RTD guidelines (Rijkswaterstaat, 2017a), the document aims to advise and educate analysts on nonlinear finite element analysis of reinforced and prestressed concrete structures. This twofold objective is reflected in the layout of the document, where the right hand-side column on each page contains clear and concise guidelines and the left hand-side column contains the explanatory part. The document covers all relevant aspects of modelling, such as the model definition, the set-up of the analysis procedure and the reporting of the model and results (chapters 2, 3 and 5, respectively). Additionally, the document provides the analysts with information on how to use/interpret the results of nonlinear finite element analysis in serviceability and ultimate limit state verifications (chapter 4).

This chapter reports findings related to the application of the RTD guidelines for the analyses of the three prestressed concrete beams, with the main focus on the modelling aspects. TNO has already shared their view on the use of nonlinear finite element analysis of concrete structures in ultimate limit state verifications via earlier communications, see (Slobbe, 2017).

Based on the current work, the following issues are recommended for consideration in case of amending the guidelines.

<u>The modelling of geometrical aspects of the structure:</u>
The modelling of the geometry is closely related to other modelling aspects, e.g. the choice of the element types. Hence, it is difficult to address this aspect of modelling specifically in the guidelines. Nevertheless, the following issues deserve more guidance:

- the cross-sectional discretization of the concrete in case shell elements are the preferred element types;
- in case the I-shaped beams are modelled with shell elements and the flanges are modelled by “out-of-plane” shell elements, the stirrups in the flanges need to be modelled to avoid the occurrence of an unrealistic large splitting crack;

Furthermore, it is recommended to request the analyst to explicitly report on the way the geometry is modelled, since here important assumptions are often made.

<u>Material modelling:</u>
Related to the modelling of the material and the input of the material properties, the following aspects of modelling need attention:

- It is recommended to adopt the rotating crack model rather than the fixed crack model;
- For the sake of completeness, the table in subsection 2.3.1 of the guidelines should also include the formulas for lightweight aggregate concrete and high strength concrete;
- To avoid confusion, the recommended value for Poisson’s ratio in the table of subsection 2.3.1 should be consistent with *fib* Model Code 2010 (CEB/fib, 2012) or it should be explicitly mentioned that the RTD guidelines deviates from *fib* Model Code 2010 in this respect;

- To avoid confusion, the minimum reduction factor of 0.4 for the concrete compressive strength due to lateral cracking in the table of subsection 2.3.1 should be consistent with the examples shown in the RTD document (Rijkswaterstaat, 2017b);
- Subsection 2.3.2 of the guidelines allows to define the material properties for the bars on the basis of experimental tests, however no reference is made to specific measuring methods. Regarding the ultimate strain values, the measuring length applied in the test is important for the assessment. Assuming that the measuring length is known, guidance is needed on how this information should be used in the determination of the ultimate strain value in relation to the element size and/or the interpretation of the analysis results in case strain values in the reinforcing bars are close to this ultimate strain value;
- Though interface elements and properties are no physical entities in a concrete structure, they may play a crucial role in the modelling of concrete structures. The incorporation of guidelines with respect to interface element types and proper estimation of their properties is therefore recommended.

Finite element discretization:
Subsection 2.5.5 of the RTD guidelines provides provisions for the maximum element size, which depends on the type of structure and number of dimensions in the model. For the cases considered in this report, it means that element sizes larger than 100 mm are allowed. However, for the cases considered, such element sizes are believed to be too large, since it is expected that they cannot properly describe:

- the cross-section of the beam;
- the stress state in the compression zone;
- the cracking and failure behaviour.

Hence, it is recommended to incorporate such reasons as mentioned before in the guidelines for the maximum element size.

The modelling of prestressing:
It is recommended to pay more attention to the modelling of the prestressing, treated in section 2.6 of the guidelines. Typical questions that should be discussed, are:

- How to deal with a large number of strands in the cross-section? Should they be modelled separately, or is it allowed to combine them in one or more bundle of strands?
- What are the important aspects when modelling a pre-tensioned system and a post-tensioned system?
- How to treat the transmission and loses of the prestressing forces in the model?

Evaluation of the numerical results:
It is worthwhile to provide more explanation and, if possible, more guidance in section 3.4 of the guidelines on how to interpret a converged equilibrium path after temporarily no convergence has been reached. This could for instance be done by further specification of the notion “plausible explanation” and/or by adding examples where structural/physical considerations give rise to either accept or to abandon the converged equilibrium path after some non-converged load steps.

Application of the safety formats:

Section 4.2 of the guidelines contains a description of the three safety formats according to *fib* Model Code 2010 (CEB/fib, 2012). With respect to input for the nonlinear finite element analyses in these formats, which are summarized in Annex A of the guidelines, the following comments are made:

- The guidelines only inform how certain material input values of the concrete and reinforcement parameters for the different analyses should be calculated, implicitly taking into account their stochastic distribution and associated uncertainties. Though not explicitly stated, all other parameters are treated as deterministic. However, it is unclear why the uncertainties are neglected for instance for the ultimate strain value ε_{su} for the reinforcements and some geometry parameters (e.g. the cross-sectional area of the rebars). More clarification is needed. Note that aforementioned parameters can be important for the outcomes of the analysis in some applications in reinforced concrete structures. Hence, their stochastic distributions and uncertainties should be considered as well.
- From the table in Annex A, it is noted that the fractile values for the different input parameters of the concrete are calculated in different ways. The following peculiarities are observed:
  - the variations in the fracture energies G_f and G_c over the calculated fractile values are very small and these values do not proportionally change with the corresponding fractile values of the tensile strength f_{ct} and compressive strength f_c;
  - the empirical correlation between the compressive strength f_c and the tensile strength f_{ct} is released: the characteristic value of f_c is larger than the mean GRF value of f_c, whereas the characteristic value of f_{ct} is smaller than the mean GRF value of f_{ct}.

  These peculiarities cannot be physically justified and lead to questionable sets of input parameters for the concrete.

Based on aforementioned observations, it is recommended to reconsider the table in Annex A. One could think of an approach that recommends calculating the fractile values of the concrete properties by using the current state-of-the-art knowledge of probabilistic models and correlations, see e.g. (JCSS, 2000).

6 References

CEB/fib. (2012). Model Code 2010 - Final draft, Volume 2. fib Bulletin No. 66. In: Ernst & Sohn.

CEN. (2011). Eurocode 2: Design of concrete structures. Part 1-1: General rules and rules for buildings. In. Brussels, Belgium.

Choulli, Y. (2005). *Shear behaviour of prestressed I-beams made with high strength self compacting concrete.* (PhD), Technical University of Catalonia, Barcelona.

Govindjee, S., Kay, G.J., Simo, J.C. (1995). Anisotropic modelling and numerical simulation of brittle damage in concrete. *International Journal for numerical Methods in Engineering, 38*, 3611–3633.

Hordijk, D. A. (1991). *Local approach to fatigue of concrete.* (PhD), Delft University of Technology, Delft.

JCSS. (2000). JCSS Probabilistic Model Code. In *Part III - Resistance Models*: Joint Committee on Structural Safety.

Leonhardt, F., Koch, R, Rostásy, S. (1973). *Schubversuche an Spannbetonträgern*. Retrieved from Berlin:

Nakamura, H., Higai, T. (2001). *Compressive fracture energy and fracture zone length of concrete.* Paper presented at the Modelling of inelastic behavior of RC structures under seismic loads.

Rijkswaterstaat. (2017a). *Guidelines for nonlinear finite element analyses of concrete structures*. (Rijkswaterstaat Technical Document RTD:1016-1:2017 (version 2.1)).

Rijkswaterstaat. (2017b). *Validation of the Guidelines for Nonlinear Finite Element Analysis of Concrete Structures - Part: Prestressed beams*. (Rijkswaterstaat Technical Document RTD:1016-3B:2017).

Selby, R. G., Vecchio, F. J. . (1993). *Three-dimensional Constitutive Relations for Reinforced Concrete*. Retrieved from Toronto:

Slobbe, A. T., Bigaj-van Vliet, A.J., Rózsás, Á., Allaix, D.L. (2017). *Plan of approach for a follow-up study: probabilistic nonlinear finite element analysis of a prestressed concrete girder*. Retrieved from

Vecchio, F. J., Collins, M. P. . (1993). Compression response of cracked reinforced concrete. *Journal of Structural Engineering, ASCE, 119*, 3590-3610.

7 Signature

Delft, 30 April 2018

Dr.Ir. A.T. Slobbe
Author

Ir. H.G. Burggraaf
Reviewer

Ir. E. Hagen
Research Manager
Structural Reliability

A Case PB5: additional results

Figure 96 and Figure 97 show the graphs with the entire numerically obtained load – deflection responses of the analyses belonging to the safety formats and the sensitivity analyses of case PB5. Table 39 provides a summary of the first peak load value and second peak load value of all these analyses.

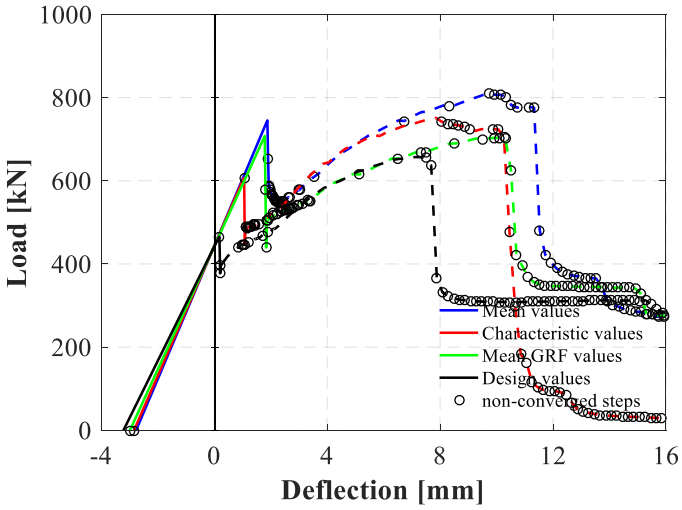

Figure 96: Case PB5. Load – deflection curves of the analyses with mean values, characteristic values, mean GRF values and design values for the input parameters of the concrete, reinforcing bars and strands.

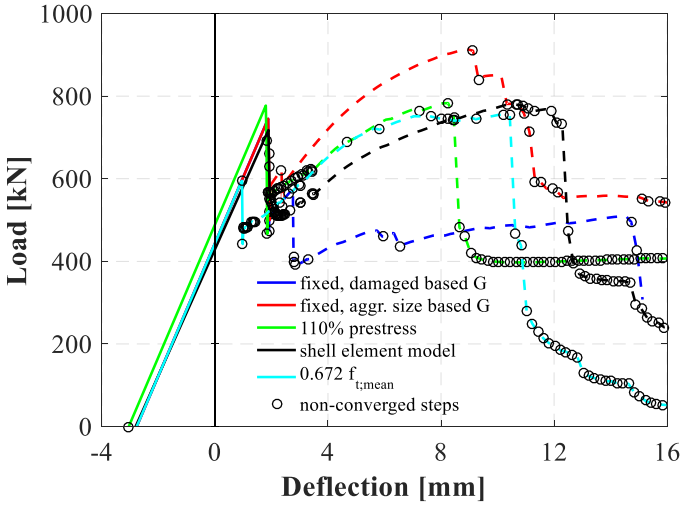

Figure 97: Case PB5. Load – deflection curves of the sensitivity analyses.

Table 39: Case PB5. Summary of peak load values of all analyses.

Analysis	**1st peak load (kN)**	**2nd peak load (kN)**
Reference analysis (“No safety format”, mean values)	745.2	809.1
Analysis with characteristic values	606.9	751.3
Analysis with mean GRF values	707.5	703.4
Analysis with design values	465.6	657.0
Fixed crack model – damaged based shear retention	745.2	510.6
Fixed crack model – aggr. size based shear retention	745.2	913.6
10% higher prestressing force	777.2	783.1
Shell element model	717.9	781.5
Reduced tensile strength of the concrete	594.8	756.7

B Case PB7: additional results

Figure 98 to Figure 104 show the contour plots with the meshes with normalized deformations, crack widths, maximum principal strains (ε_1), minimal principal strains (ε_2), the strains in the stirrups, the strains in the reinforcing bars and the strains in the strands around the peak and in the post-peak regime for all sensitivity analyses of case PB7.

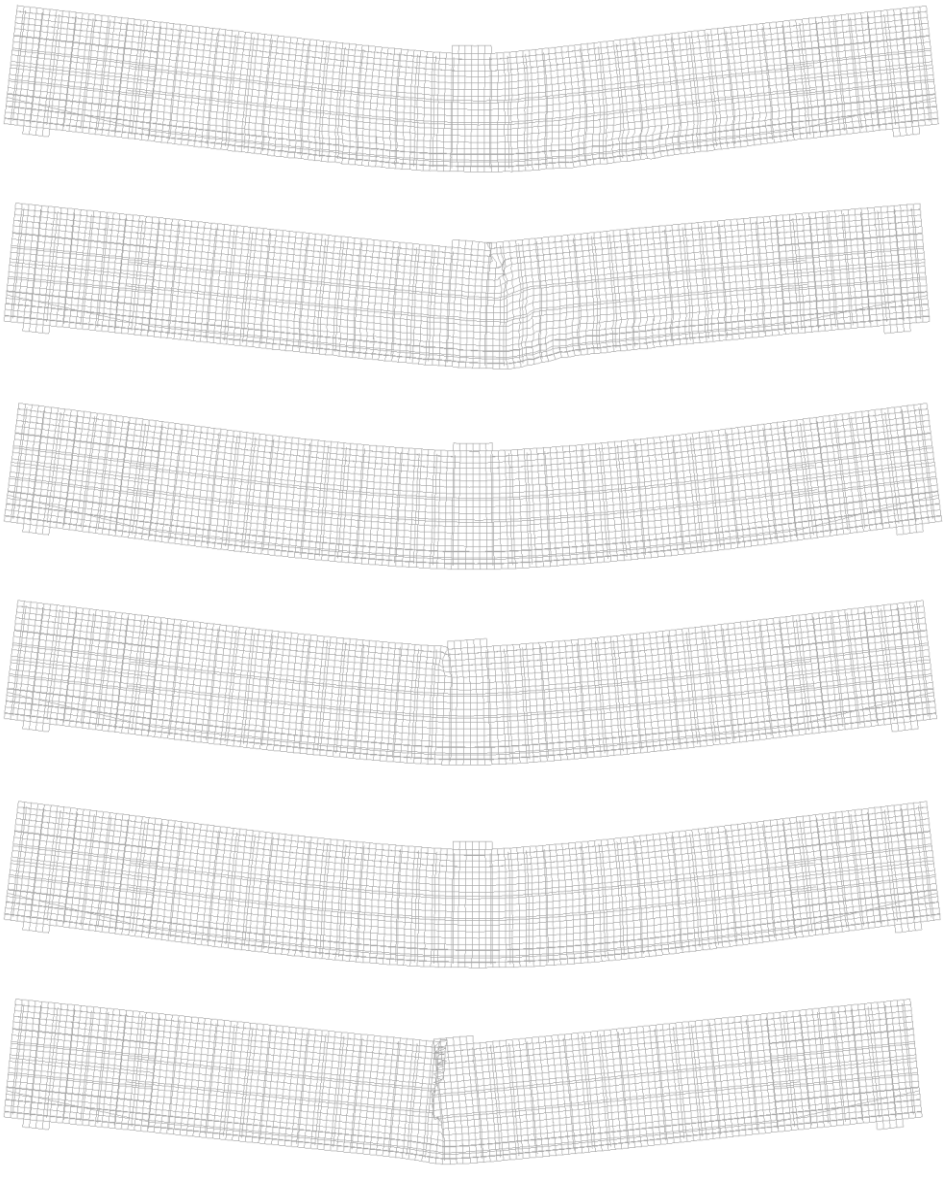

(a)

(b)

(c)

Continued at the next page

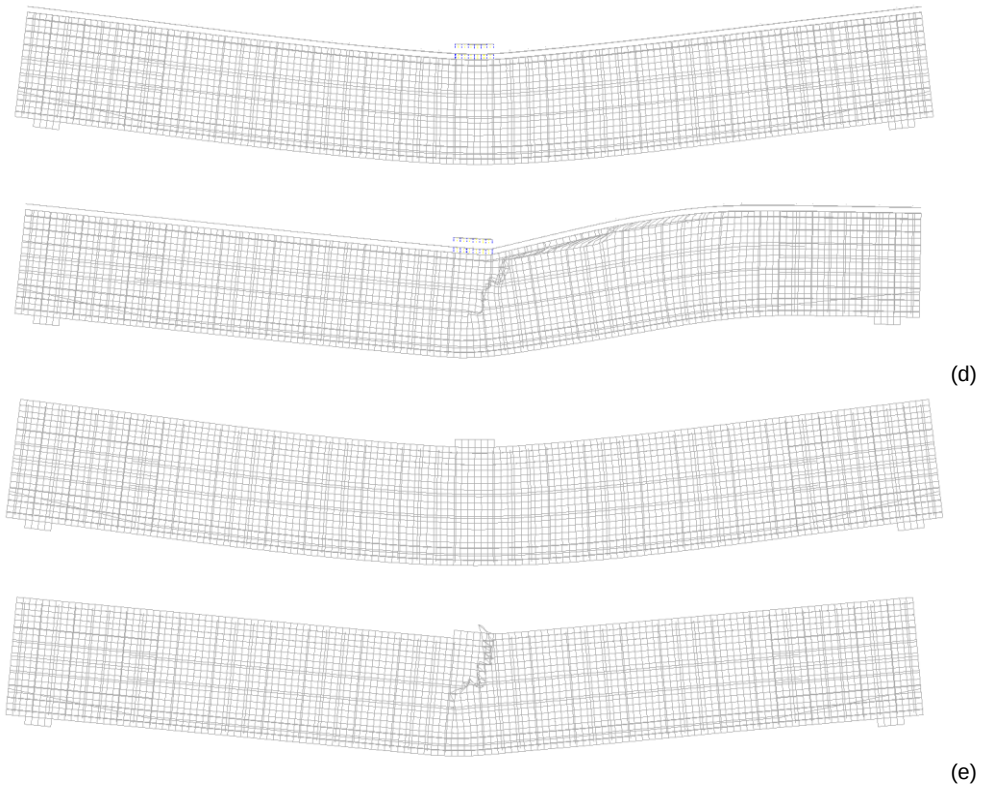

(d)

(e)

Figure 98: Case PB7. Deformed meshes around the peak and in the post-peak regime, belonging to the sensitivity analyses (a) “fixed, damaged based G”, (b) “fixed, aggregate size based G”, (c) “110% prestress”, (d) “shell element model” and (e) “0.672 $f_{t;mean}$” (see Figure 95).

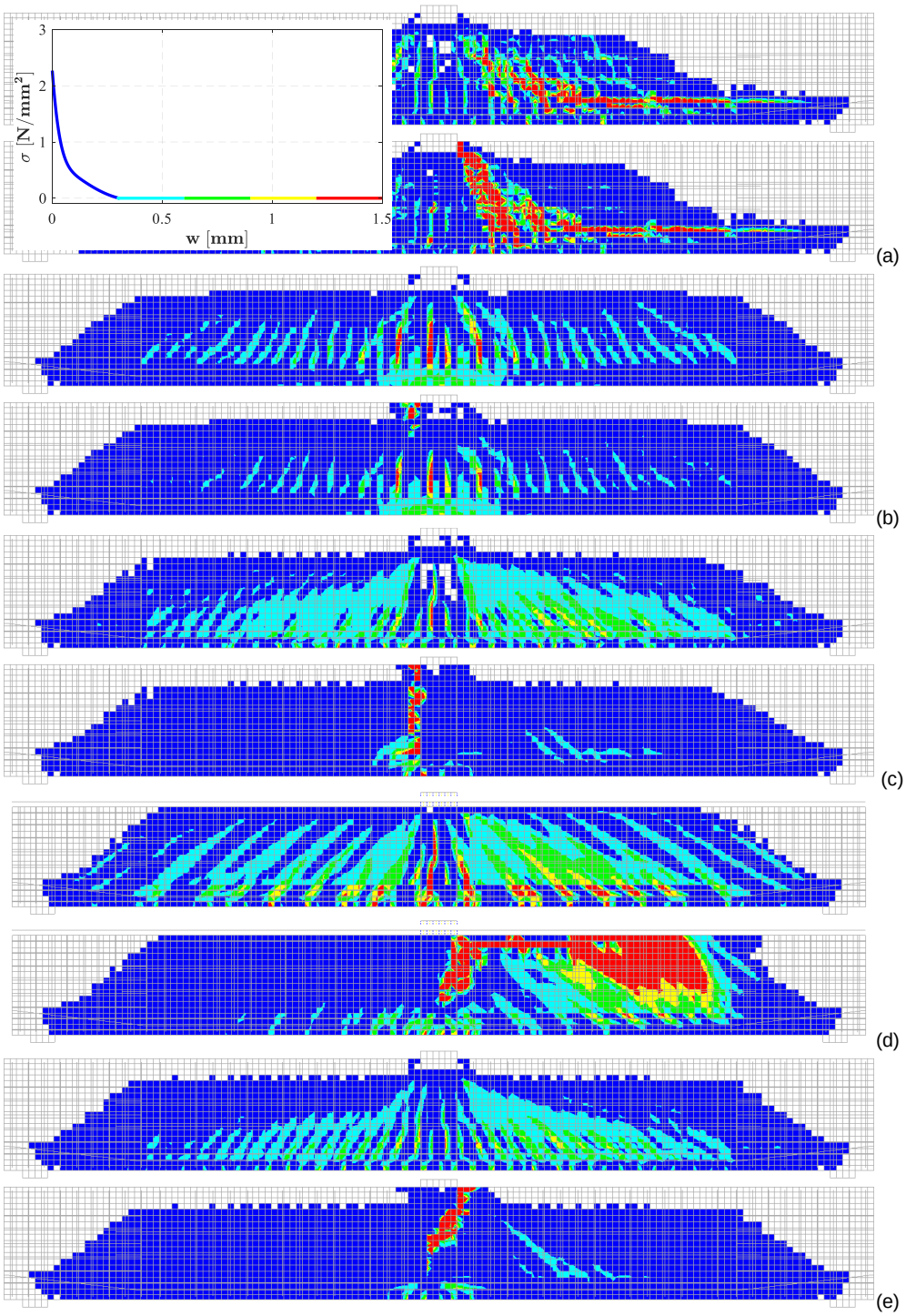

Figure 99: Case PB7. Crack width plots around the peak and in the post-peak regime, belonging to the sensitivity analyses (a) “fixed, damaged based G”, (b) “fixed, aggregate size based G”, (c) “110% prestress”, (d) “shell element model” and (e) “0.672 $f_{t;mean}$” (see Figure 95).

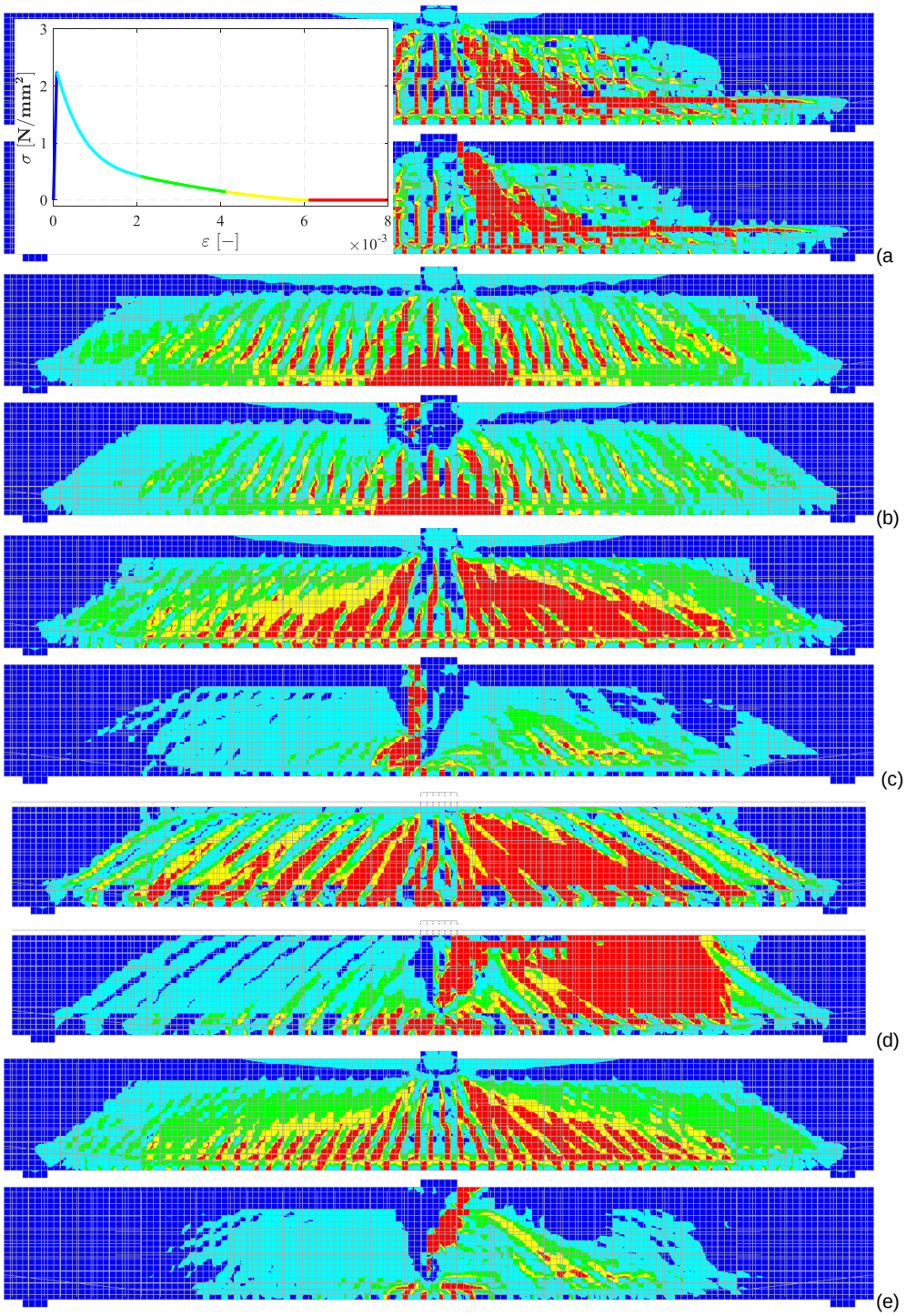

Figure 100: Case PB7. Maximum principal strain plots (ε_1) around the peak and in the post-peak regime, belonging to the sensitivity analyses (a) “fixed, damaged based G”, (b) “fixed, aggregate size based G”, (c) “110% prestress”, (d) “shell element model” and (e) “0.672 $f_{t;mean}$” (see Figure 95).

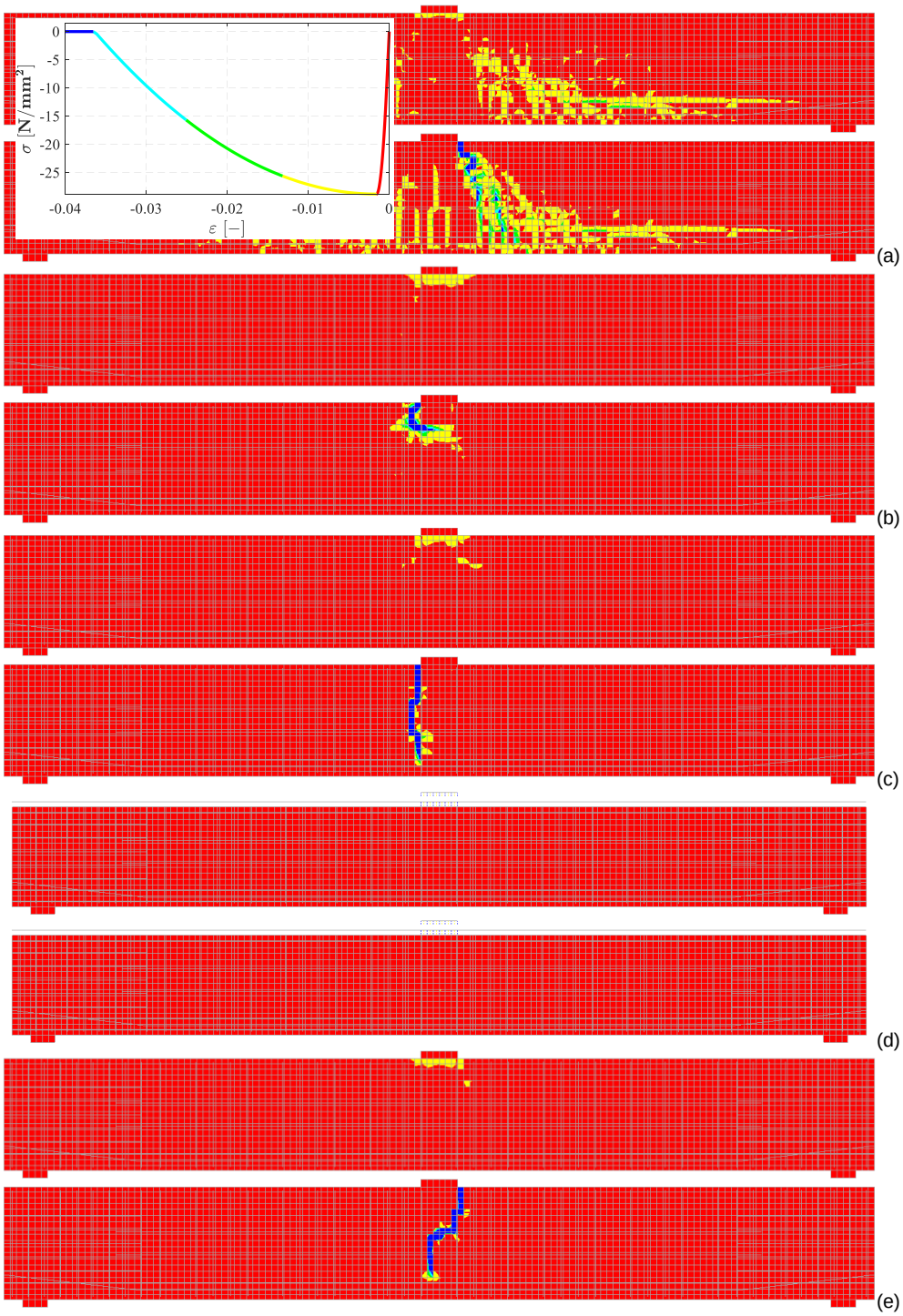

Figure 101: Case PB7. Minimum principal strain plots (ε_2) around the peak and in the post-peak regime, belonging to the sensitivity analyses (a) “fixed, damaged based G”, (b) “fixed, aggregate size based G”, (c) “110% prestress”, (d) “shell element model” and (e) “0.672 $f_{t;mean}$” (see Figure 95).

Figure 102: Case PB7. Strains in longitudinal reinforcing bars around the peak and in the post-peak regime, belonging to the sensitivity analyses (a) “fixed, damaged based G”, (b) “fixed, aggregate size based G”, (c) “110% prestress”, (d) “shell element model” and (e) “0.672 $f_{t;mean}$” (see Figure 95).

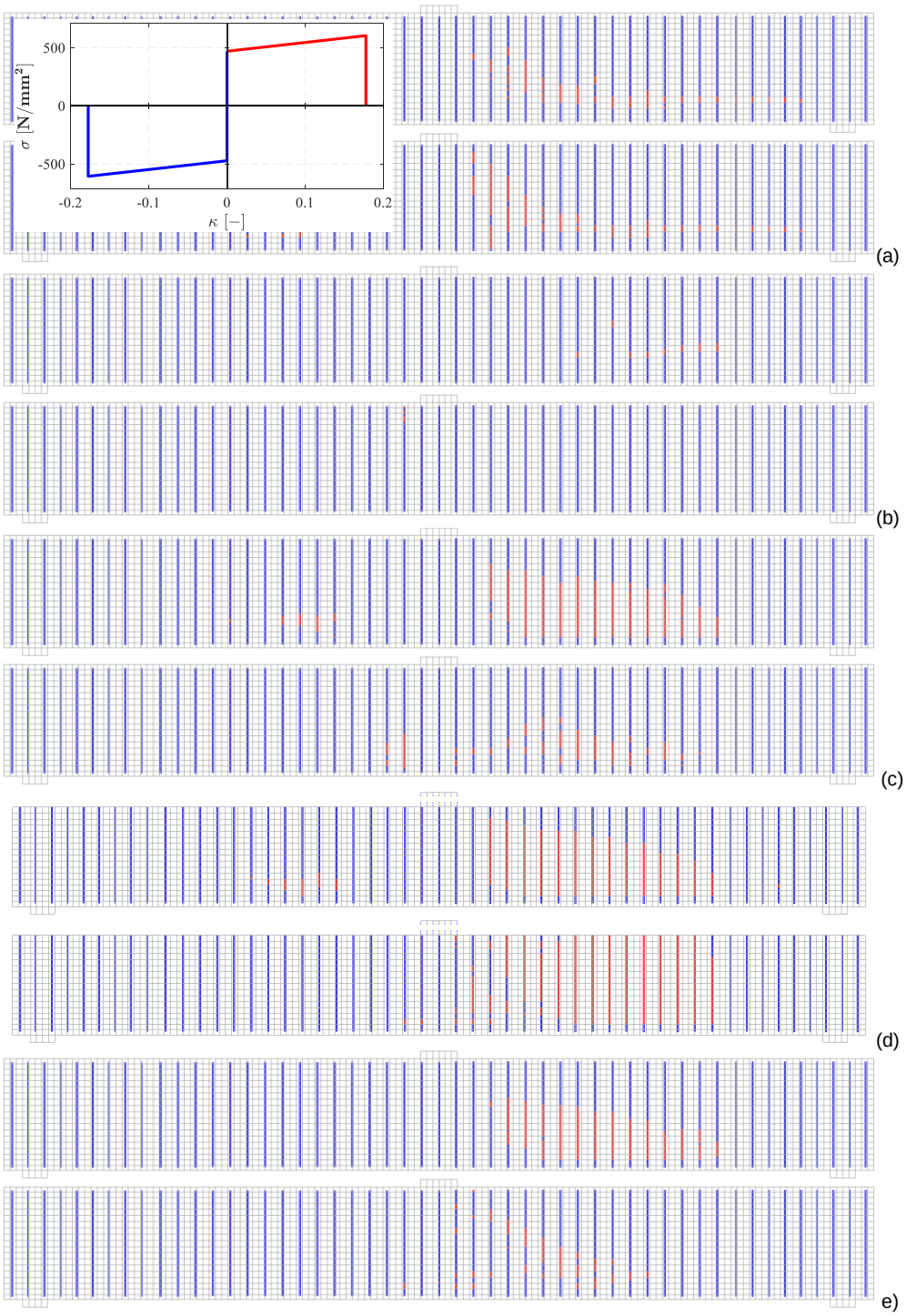

Figure 103: Case PB7. Strains in stirrups around the peak and in the post-peak regime, belonging to the sensitivity analyses (a) “fixed, damaged based G”, (b) “fixed, aggregate size based G”, (c) “110% prestress”, (d) “shell element model” and (e) “0.672 $f_{t;mean}$” (see Figure 95).

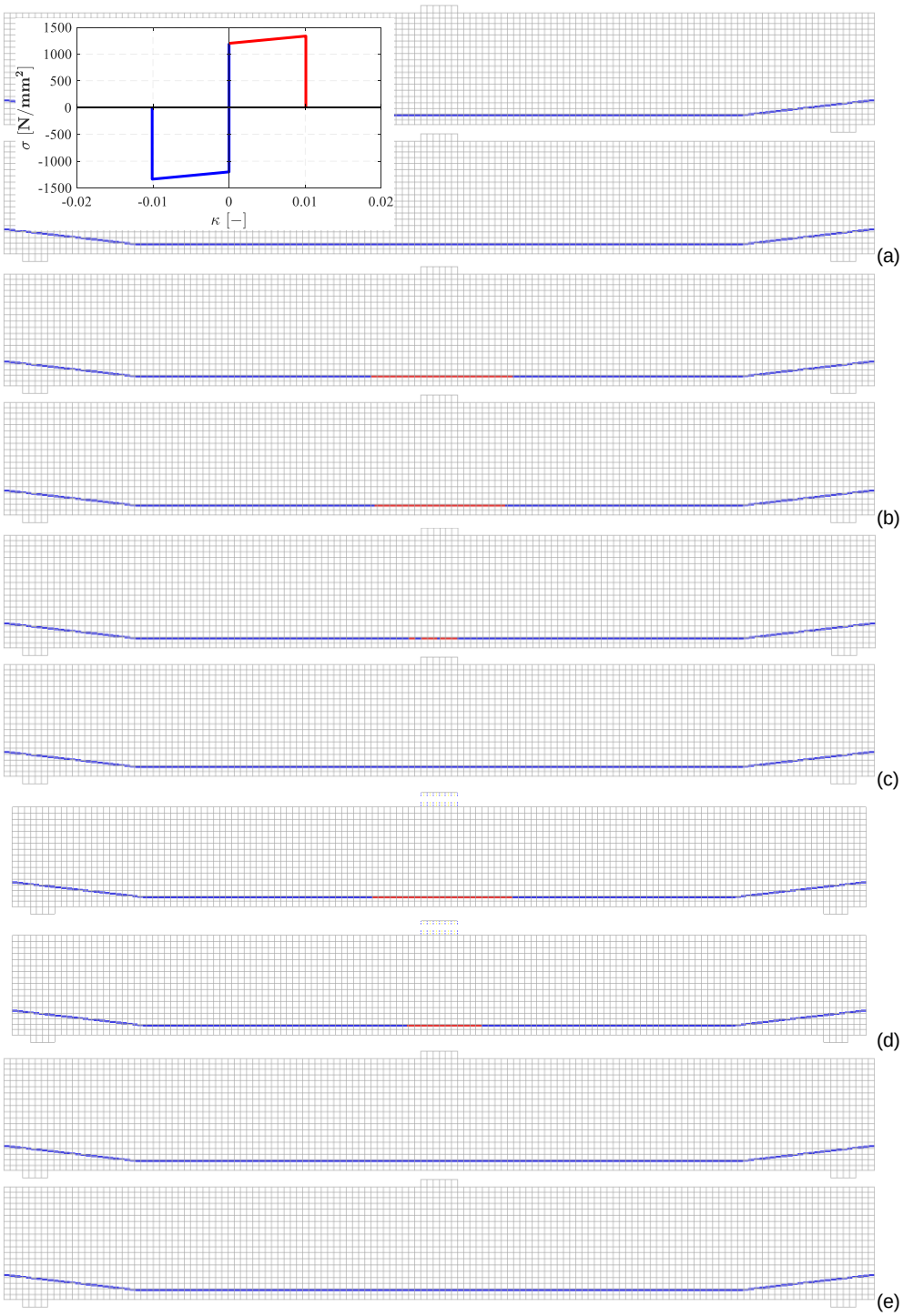

Figure 104: Case PB7. Strains in the tendons around the peak and in the post-peak regime, belonging to the sensitivity analyses (a) “fixed, damaged based G”, (b) “fixed, aggregate size based G”, (c) “110% prestress”, (d) “shell element model” and (e) “0.672 $f_{t;mean}$” (see Figure 95).